NTNU

Norwegian University of
Science and Technology

Characterization of Iron Bearing Particles in Relation to Fir-Tree Structure in Al-Mg Alloys

Idun Solli
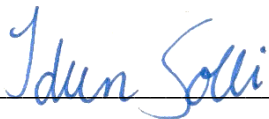
Preface

This master thesis has been carried out at the Norwegian University of Science and Technology (NTNU), Department of Materials Science and Engineering, the spring of 2018. The master project is an extension of a project work within TMT4500 Materials Technology, Specialization Project, fall of 2017. The project report was entitled as "Characterization of Fir-tree structure in Al-Mg Alloys". This master thesis has been carried out in cooperation with Hydro Aluminium.

Idun Solli

Abstract

Fir-tree structure is a well-known problem related to DC cast AA1xxx and AA5xxx alloys. During DC casting different iron bearing particles, e.g. Al_mFe, Al_3Fe and Al_6Fe, are formed. A change of the dominating iron bearing particles across the ingot cross section can result in Fir-tree structure, which in turn will cause streaking in the anodised aluminium product. This master thesis consisted of two main parts: development of reliable experimental methods to identify different types of iron bearing particles and quantitative characterization of iron bearing particles to study the mechanism for Fir-tree structure formation.

Samples cut from the cross section of a commercial DC cast AA5005 sheet ingot was studied. Different techniques and approaches for characterization of iron bearing particles were tested and compared. The morphology of the iron bearing particles was studied in both plane polished samples, deep etched samples and in powder samples. The iron bearing particles have been identified by a combination of EBSD, WDS and XRD.

The grain size of the ingot as a function of the distance from the ingot surface has been measured by anodising and light microscopy. It shows that the grain size increases with increasing distance from the surface of ingot. This indicates that the cooling rate is highest at the surface of the ingot and decreases towards the center of the ingot. A transition in dominating morphology of iron bearing particles could be observed in light microscope imaging. At the ingot surface region until a depth of 5.6 cm, where the cooling rate is highest, the dominating particle was skeletal shaped. At regions of 7.2-10.4 cm in distance to surface, it was a mix of skeletal and needle-like particles. The dominating morphology of particles at regions of 12.0-13.6 cm in distance to surface, where the cooling rate is lowest, was needle-like.

It was shown that EBSD and WDS could not be used for quantitative analysis, but could be used to determine the characteristic morphology of the different iron bearing phases. The characteristic morphology of Al_mFe was skeletal with frequently branching. Needle-like and stacked plate was the typical morphology for Al_3Fe. Al_6Fe was only identified with EBSD and WDS occasionally, showing the morphology was either skeletal-like or plate-like.

The phenol method for extracting iron bearing particles from the aluminium matrix, was for the first time developed at the Department of Materials Science and Engineering. The iron bearing particles were successfully extracted, and a quantitative analysis of the particle powder XRD results were performed by the Rietveld refinement method. The measured fraction of different phases showed that Al_mFe dominated the regions close to the ingot surface, with approximately 90 wt%. The remaining particles were Al_3Fe. At 135 mm in distance to surface, the phase distribution of particles was completely different: 89 wt% Al_3Fe, 10 wt% Al_mFe and 1 wt% Al_6Fe. Al_6Fe phase only existed as a minority phase at some locations towards the center of the ingot.

Between 65 and 79 mm in mean distance to surface, there was a rapid change in dominating particle phase from Al_mFe to Al_3Fe. This corresponds well with the measured minimum Fir-tree height of 59 mm and the morphology study. The reason for the formation of Fir-tree structure, was supposed to be the sudden change of dominating iron bearing phases. The phase selection of iron bearing particles was distribution was discussed inn correlation with local cooling rate in the ingot during solidification and chemical composition of the alloy.

Sammendrag

«Fir-tree structure» er et velkjent problem knyttet til DC-støping av AA1xxx og AA5xxx legeringer. Under DC-støping vil det dannes forskjellige jernholdige partikler, som for eksempel Al_mFe, Al_3Fe and Al_6Fe. Fir-tree structure oppstår når det dannes soner med forskjellig dominerende jernholdige partikler. Valseblokker med Fir-tree structure vil gi defekte anodiserte produkter, i form av lyse og mørke bånd etter anodisering.

Denne masteroppgaven har bestått av to deler: utvikling av pålitelig identifisering av jernholdige partikler og kvantitativ karakterisering jernholdige partikler for å studere dannelsen av Fir-tree structure. Det ble tatt ut prøver fra tverrsnittet av en valseblokk av legeringen AA5005. Ulike teknikker og tilnærminger for karakterisering av jernholdige partikler ble testet og sammenlignet. Fasene Al_mFe, Al_3Fe og Al_6Fe ble identifisert ved kombinasjon av EBSD, WDS og XRD. Morfologien til partiklene ble studert i både planpolerte prøver, dypetsede prøver og i pulverform.

Kornstørrelsen ble målt som funksjon av avstand fra valseoverflaten ved bruk av anodisering og lysmikroskop. Kornstørrelsen økte med økende avstand fra valseoverflaten. Dette viser at avkjølingshastigheten var høyest ved overflaten av valseblokken og avtok mot senter. Da morfologien til partiklene ble studert i lysmikroskop, ble det observert en overgang i dominerende morfologi for de jernholdige partiklene. Den dominerende morfologien på partiklene fra valseoverflaten til en dybde på 5.6 cm, hvor avkjølingshastigheten er høyest, var dendrittaktig. I områdene 7.2-10.4 cm fra valseoverflaten, var det en blanding av partikler med dendritt- og nåleaktig morfologi. I området 12.0-13.6 cm i avstand til valseoverflaten, hvor avkjølingshastigheten var lavest, var den dominerende morfologien til partiklene nåleaktig.

Det var tydelig at EBSD og WDS ikke kunne benyttes til kvantitative analyser, men ved hjelp av de to ulike teknikkene kunne morfologien til de ulike partiklene bli bestemt. Den karakteristiske morfologien til Al_mFe var dendrittaktig med hyppig forgreining. Al_3Fe ble bestemt til å ha flere karakteristiske morfologier: nåleaktig, plateaktig eller stablet plate. Al_6Fe ble bare identifisert ved EBSD og WDS noen få ganger. Morfologien til Al_6Fe var da enten dendrittaktig eller plateaktig.

For første gang på Instituttet for materialteknologi, ble fenolmetoden for ekstrahering av jernholdige partikler fra aluminiumsmatriks utviklet. Det lyktes å ekstrahere jernholdige partikler og kvantitative analyser ble utført ved bruk av Rietveld tilpasning av pulver XRD-målinger. Den målte fraksjonen av forskjellige faser viste at ved valseoverflaten dominerte Al_mFe med ca. 90 wt%, de resterende 10 wt% var Al_3Fe. Ved 135 mm i avstand til valseoverflaten, var faseforedelingen en helt annen: 89 wt% Al_3Fe, 10 wt% Al_mFe og 1 wt% Al_6Fe. Al_6Fe eksisterte kun som en minoritetsfase ved noen lokasjoner mot senter av valseblokken. Mellom 65 og 79 mm i avstand til valseoverflaten var det et raskt skifte i

dominerende fase fra Al_mFe til Al_3Fe. Dette samsvarer godt med den målte Fir-tree høyden på 59 mm og morfologistudien. Grunnen til dannelsen av Fir-tree structure ble foreslått til å være den raske overgangen i dominerende jernholdig fase. Fasefordelingen ble diskutert med utgangspunkt i beregninger for avkjølingshastighet og den kjemiske sammensetningen til legeringen.

Table of Content

x

1 Introduction

Aluminium is a metal with a wide range of applications. In the last years, transport industry has been growing into a major market of aluminium alloys. Exterior of buildings is another important area of application for aluminium. Within these applications, the AA5xxx series is widely used due to the alloy's high strength and good corrosion resistance in marine environments [16]. The major element in the AA5xxx series is magnesium, which increases the alloy's strength by solid solution strengthening. Within the AA5xxx series, anodised AA5005 sheet is common for architectural applications.

Anodising is a well-known surface treatment of aluminium. It does not only improve the corrosion resistance of the product, but it can really change the looks of the product. Giving both glossy and matt finish, anodising can meet different aesthetic requirements for architectural applications. To produce the desired anodised surface, does not only require thorough control of process parameters during anodising, but also strict control of the casting parameters to ensure a good base material. Streaking is a typical defect in anodised products, caused by poor base material. Streaking are light and dark bands in the rolling direction [6]. Streaking can be a result of inclusions, non-uniform grain structure or local differences in the primary constituents in the aluminium matrix, known as Fir-tree structure. The Fir-tree structure is a well-known problem related to both DC cast AA5xxx and AA1xxx alloys.

The Fir-tree structure is a result of different locations of a DC-cast ingot having different dominating iron bearing particles. One of the steps during anodising is etching. Different iron bearing particles will have different response to the chemical treatment. Upon caustic etching, the cross section of casting ingots will show a Fir-tree like pattern, hence the name of the defect [6]. Parameters such as cooling rate during DC casting and chemical composition of the alloy will influence the formation of iron bearing particles and favour formation of one instead of another. The iron bearing particles which cause the formation of Fir-tree structure, are usually very small and have very similar chemical composition. Therefore, it is difficult to identify the particles and get quantitative analyses. This is the reasons why it is still challenging to predict the formation of Fir-tree structure in the casting house, though there has been made a great effort in studying this defect.

This master thesis will deal with characterization of iron bearing particles in relation to Fir-tree structure in a DC cast AA5005 sheet ingot. Firstly, different methods for identification of iron bearing particles will be tested and compared to ensure reliable phase identification. Secondly, quantitative analysis of the iron bearing particles. The results will be compared to previous research to get indications of why the Fir-tree structure formed. In order to get an understanding of how this structure arises, basic theory regarding solidification and DC casting will be presented. It will be discussed how different factors, such as cooling rate and chemical composition, affect the formation of primary constituents during solidification. Since a great

part of the thesis is to find reliable techniques for identification of the particles, it is essential to have good knowledge about different techniques for phase identification. The principals behind EDS, WDS, EBSD and XRD, which are typical techniques for phase identification within metallurgy, will therefore also be included in the theoretical background.

2 Theoretical Background

2.1 Solidification

In metals, solidification proceeds in a temperature range rather than at one distinct temperature. Solidification can be divided into two steps: nucleation and growth. Nucleation marks the beginning of the phase transformation from liquid to solid. There are two factors nucleation depends upon [9]:

I) Free energy available for phase transformation from liquid to solid

$$Volume\ free\ energy = -\frac{4}{3}\pi r^3 \Delta G_v \qquad (1.1)$$

II) Energy required to form a liquid-solid interface

$$Interfacial\ energy = 4\pi r^2 \gamma_{SL} \qquad (1.2)$$

The total free energy for solid embryo with radius *r* is therefore:

$$\Delta G_r = -\frac{4}{3}\pi r^3 \Delta G_v + 4\pi r^2 \gamma_{SL} \qquad (1.3)$$

$$\Delta G_v = \frac{L_v \Delta T}{T_m} \qquad (1.4)$$

Where

ΔG_v: Change in free energy per unit volume

r: Radius of spherical embryo

γ_{SL}: Solid/liquid interfacial free energy

L_v: Latent heat of fusion per unit volume

T_m: Melting temperature

ΔT: Undercooling

The terms for volume free energy (red line) and interfacial energy (blue line) are illustrated in Figure 2.1, together with the expression for the total free energy, Equation (1.3) (green line). The figure shows that there exists a critical radius, *r**, associated with the solidification process. Solidification starts by a number of atoms clustering together. If this particle does not exceed the critical radius, it tends to dissolve as this will lower the free energy. These particles are called embryos [17]. On the other hand, particles that have radius larger than the critical radius will tend to grow, as this will lower the free energy. These particles are called nuclei and will grow to solid crystals by further deposition of atoms. This form of nucleation is called homogeneous nucleation and the nuclei will reduce the total free energy by continous growth.
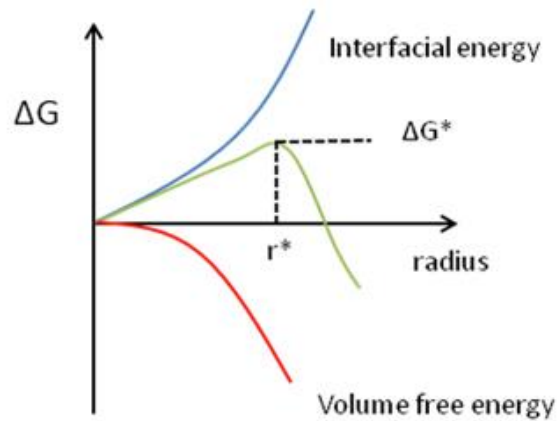
Figure 2.1: Free energy change associated with homogeneous nucleation of a sphere with radius r [7].

The driving force for solidification at *r** is the decrease in free energy going from liquid to solid [9]:

$$\frac{d}{dr}\Delta G_r < 0 \tag{1.5}$$

Where ΔG_r is given by Equation (1.3).

However, the liquid will not solidify until the undercooling is sufficient. The required undercooling is high when solid must form homogenously from the liquid, e.g. $0.25 T_m$ (≈ 165K) for liquid metal of pure aluminium [18]. Such high undercoolings are not achievable with conventional solidification processes e.g. casting. The walls of the liquid container will catalyse the nucleation, hence increase the nucleation frequency [9]. Also, there will always be inclusion particles in the liquid that can act as potential nucleation sites. This is called heterogeneous nucleation. Solid substrates in the liquid metal (e.g. mould wall or inclusions) will reduce the activation barrier for nucleation, thereby reducing the need for substantial undercoolings. The difference between homogeneous and heterogeneous nucleation is illustrated in Figure 2.2. If the nucleation in liquid metal is heterogeneous, the required undercooling will be in the order of 2 K [19].
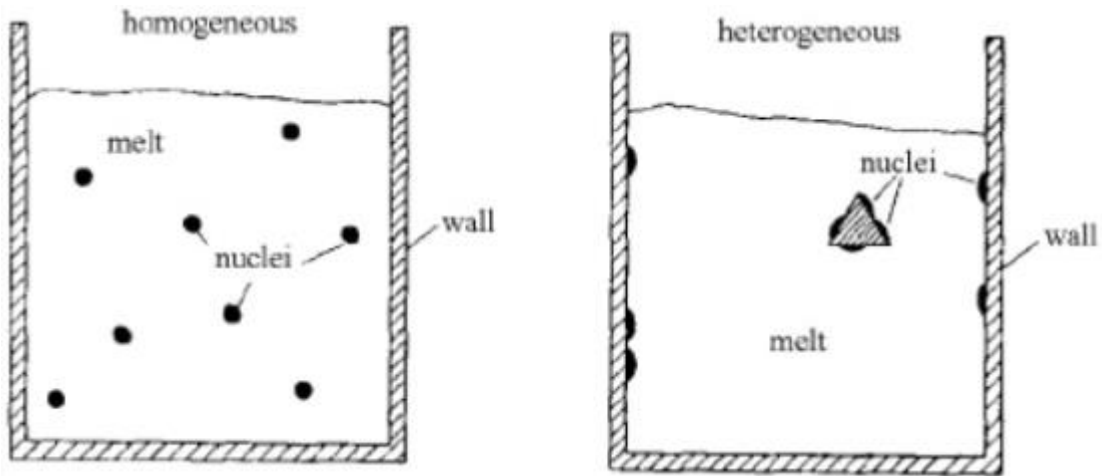
4

Figure 2.2: Schematically illustration of the difference between homogeneous and heterogeneous nucleation [7].

Equation (1.3) and (1.6) describe the excess free energy associated with the formation of clusters by homogeneous and heterogeneous nucleation, respectively [9]. It can be seen, that the term S(θ), the shape factor, is the only factor that differ in the two equations. The shape factor is dependent on the wetting angle, θ, and is a numerical value ≤ 1. If θ=10° or θ=30°, the shape factor will be 10^{-4} and 0.02, respectively. Hence, the energy barrier for heterogeneous nucleation can be much smaller than for homogeneous nucleation.

$$\Delta G_{het} = \left\{ -\frac{4}{3}\pi r^3 \Delta G_v + 4\pi r^2 \gamma_{SL} \right\} S(\theta) \qquad (1.6)$$

$$S(\theta) = \frac{(2+cos\theta)(1-cos\theta)^2}{4} \qquad (1.7)$$

Where

S(θ): Shape factor

During casting of metals, small particles can be added to increase the number of heterogenous nucleation sites (grain refiners) [19]. This will reduce the required undercooling for new solid phase to form in the liquid melt. This will have a positive effect on the strength of the material as it will decrease the size of the primary phase.

2.1.1 Solidification of Alloys

Figure 2.3 shows a hypothetical phase diagram with solidification of an alloy with composition X_0 (mole fraction of solute) that deviates from the equilibrium eutectic composition (X_E). At the liquidus temperature, T_l, the alloy will begin to solidify and the small amount of solid phase (α) will have a composition given by the solidus line [9].

$$\text{Liquid} \rightarrow \text{Liquid} + \alpha \qquad (1.8)$$

The composition of the solid and the liquid phase will follow the solidus and liquidus line, on the condition that the cooling is slow enough to allow extensive solid state diffusion and that the thermodynamic equilibrium is maintained. Determining the fraction of solid (X_{solid}) and liquid (X_{liquid}) at different temperatures, can be done by the lever rule:

$$X_{solid} = \frac{X_L - X_0}{X_L - X_S} \qquad (1.9)$$

$$X_{liquid} = 1 - X_{solid} \qquad (1.10)$$

Where

X_L and X_S: Mole fraction of solute in the liquid and solid in equilibrium at a given

temperature

The solid phase has lower concentration of solute than the liquid phase and as the solid phase grows, the solute will be rejected into the remaining liquid between the dendrites. The dendrites partition of solutes into the interdendritic liquid is called microsegregation. The interdendritic liquid will be enriched with solute and can reach the eutectic composition. When the temperature reaches T_E (eutectic temperature), the eutectic reaction will then occur, where both primary (α) and eutectic phase (β) will form from the liquid:

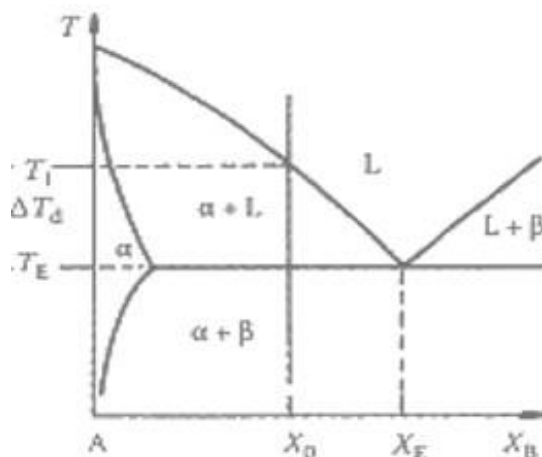$$\text{Liquid} \rightarrow \alpha + \beta \qquad (1.11)$$

Figure 2.3: Solidification of an off-eutectic alloy in a temperature gradient with alloy composition X_0 [9]

2.1.2   Direct Chill Casting of Aluminium (DC Casting)

DC casting is a semi-continuous casting process used to produce ingots and billets for further processing, such as extrusion and rolling [20]. The principle of DC casting is presented schematically in Figure 2.4. The mould is bottomless, and the first liquid metal is kept within the mould by a starter block. The mould is filled up to a desired level of liquid metal. As it can be seen from Figure 2.4, the mould is water-cooled. The water-cooled mould transfers heat from the liquid metal, giving rise to the *primary cooling*. The primary cooling causes the outer surface to solidify, which results in a shell that contains liquid metal in the center. When the liquid aluminium solidifies, it contracts, which results in an air gap between the solidified shell and the mould. The starter block is lowered with a specific rate until the desired length of the billet is reached. When the starter block is lowered, water impinges on the solidified aluminium shell and the billet is directly chilled by the water spray. This is known as *secondary cooling* and is responsible for most of the heat extraction. Between the point of contraction due to solidification and the point where the water impinges the shell, there will be a decreased cooling rate as the air gap results in a greatly reduced heat extraction through the mould [21]. This can lead to partial remelting of the shell. The extension of the air gap can increase in a greater length, if the mould is deep and the metal level is high. The risk of remelting of the shell increases, and thereby the risk of surface defects due to remelting increases. The local solidification rate in the ingot will decrease towards the center of the ingot, due to longer thermal diffusion paths [6]. Thus, DC casting gives rise to different local cooling rates across the thickness of the ingot. How the cooling rate varies as a function of distance to surface can be seen in Figure 2.5. The cooling rate is calculated by solving a 2D-Stefan problem, using material and casting parameters for the material studied in this thesis, see Table 2.1 [10].
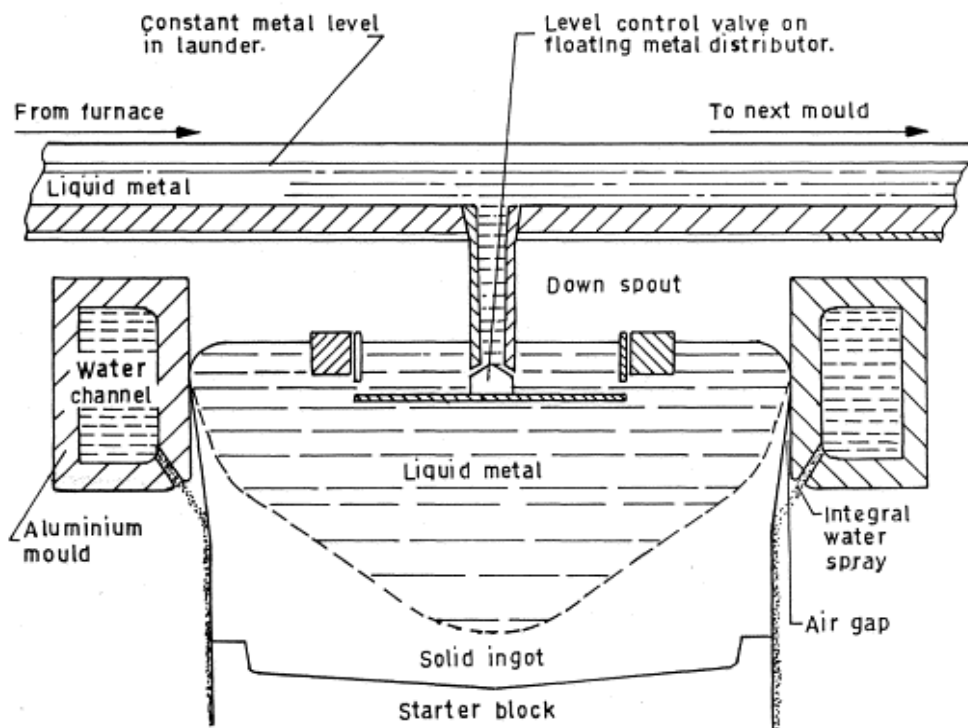

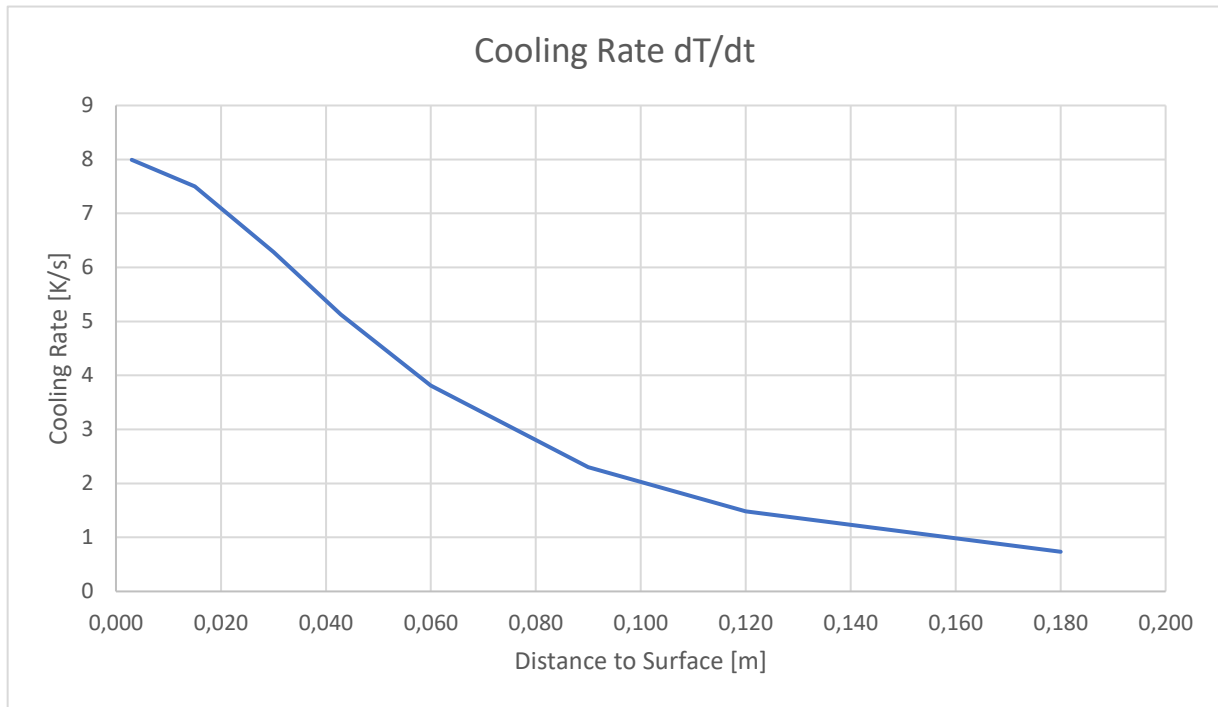*Figure 2.4: Schematical diagram of vertical DC-casting [8].*

Figure 2.5: Cooling rate as a function of distance to surface, calculated using model in Reference [10] with parameters given in Table 2.1.

Table 2.1: Parameters for solving a 2D-Stefan problem

Parameter	Value
Thermal conductivity	180
Specific heat [J/kgK]	1100
Density [kg/m^3]	2650
Latent heat melting [J/kgK]	4.00×10^5
Melting temperature [°C]	650
Surface temperature [°C]	80
Thickness [mm]	600
Casting speed [mm/min]	70

The second dendrite arm spacing (SDAS) can be measured to get indications of the local cooling rate. SDAS (λ_2) is proportional to the cube root of the solidification time (t_f), see Equation (1.12) [22]. There is also a clear correlation between the cell size and the cooling rate [21].

$$\lambda_2 = 5.5 \, (Mt_f)^{1/3} \qquad\qquad (1.12)$$

Where

M: constant related to the chemical composition of the alloy

Binary Al-Fe compounds are formed during solidification of Fe-containing commercial aluminium alloys and the cooling rate will affect which compound that is formed. Under equilibrium conditions (dT/dt < 0.015°C/s) [23], the intermetallic Al_3Fe phase is formed between the α-Al dendrite arms, see Equation (1.13). From the Al-Al_3Fe phase diagram, it can be seen that the eutectic point is at 1.85wt% Fe at the eutectic temperature 654°C, see Figure 2.6.

$$\text{Liquid}_{\text{eutectic}} \rightarrow \text{α-Al} + Al_3Fe \qquad\qquad (1.13)$$

At higher cooling rates the binary metastable Al-Fe eutectic phases Al_6Fe and Al_mFe (m=4.0-4.4) can also be formed. Figure 2.7 shows the metastable phase diagram for Al-Al_6Fe. It can be seen that the eutectic temperature has fallen from 654°C to 648°C and that the eutectic point has shifted from 1.85 wt% Fe to 3.4 wt% Fe [23]. For Al-Al_mFe, the eutectic temperature is even lower (643°C) and the eutectic point is further shifted (4.3 wt% Fe), see Figure 2.8. In Figure 2.9, the enlarged Al-rich ends of the three Al-AlFe phase diagrams are superpositioned. The formation of different eutectic phases across the thickness of the ingot can cause formation of Fir-tree structure.
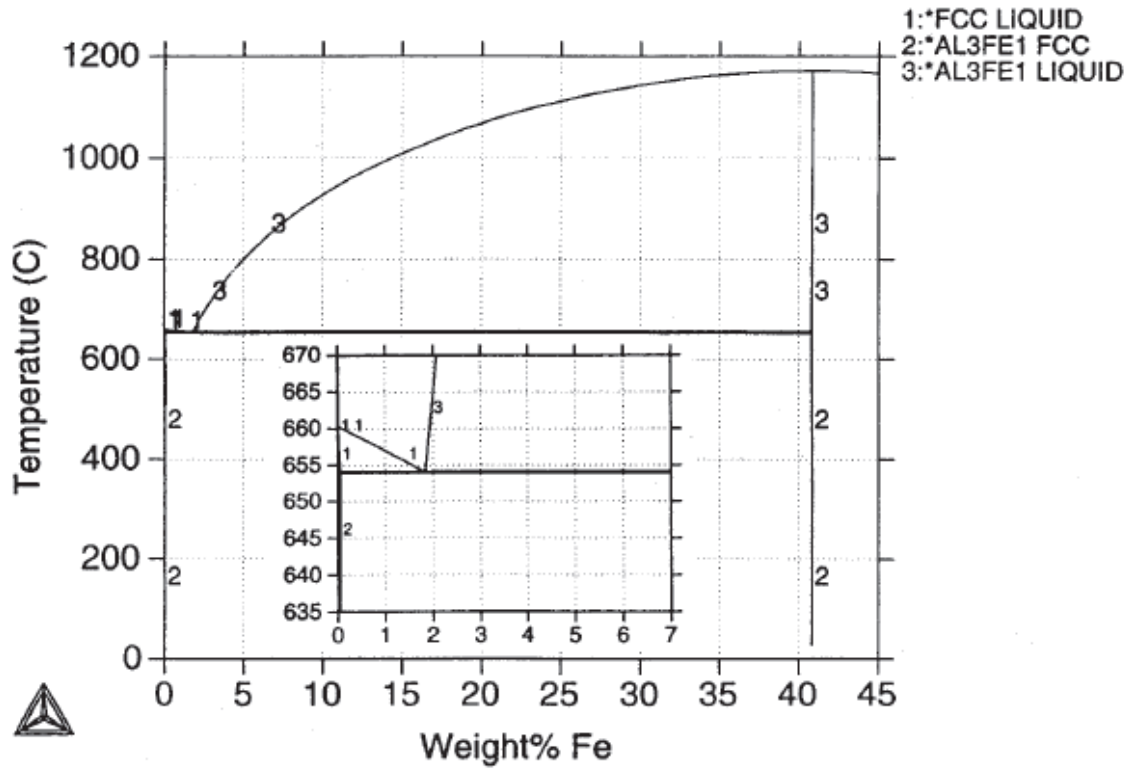
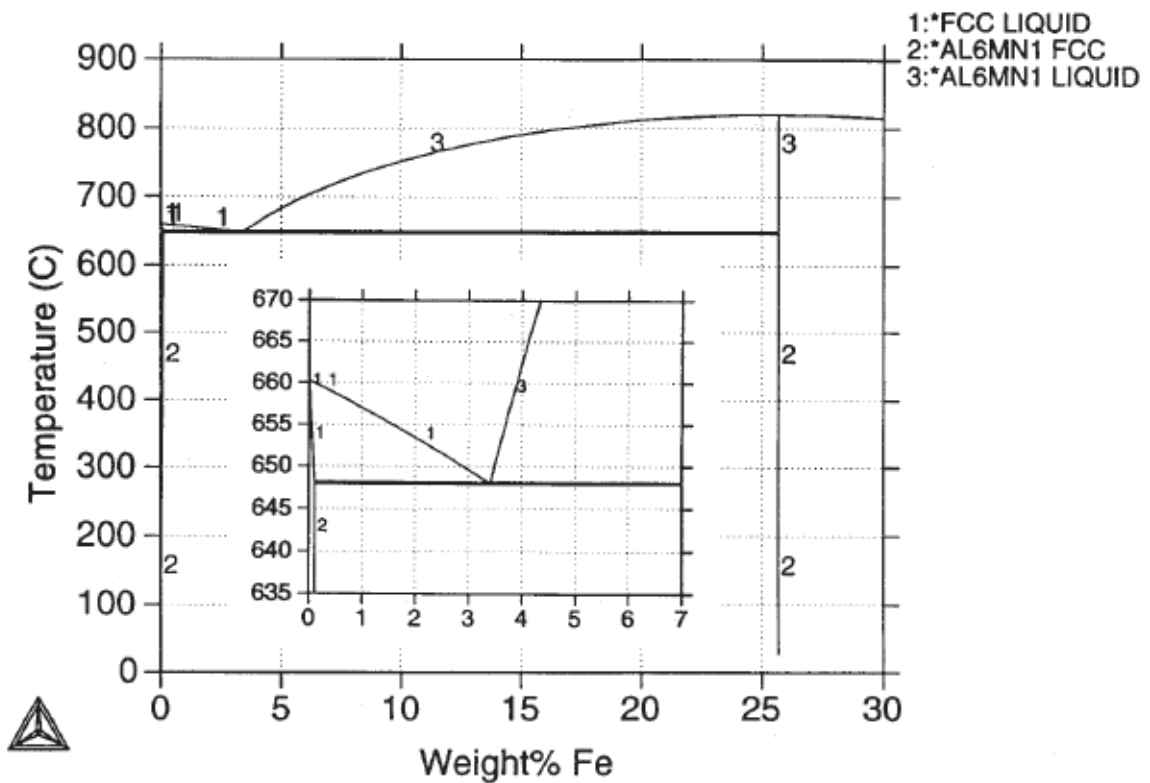*Figure 2.6: Al-Fe phase diagram computed for the Al-Al₃Fe equilibrium [12].*

Figure 2.7: Al-Fe phase diagram computed for the Al-Al₆Fe equilibrium [12].
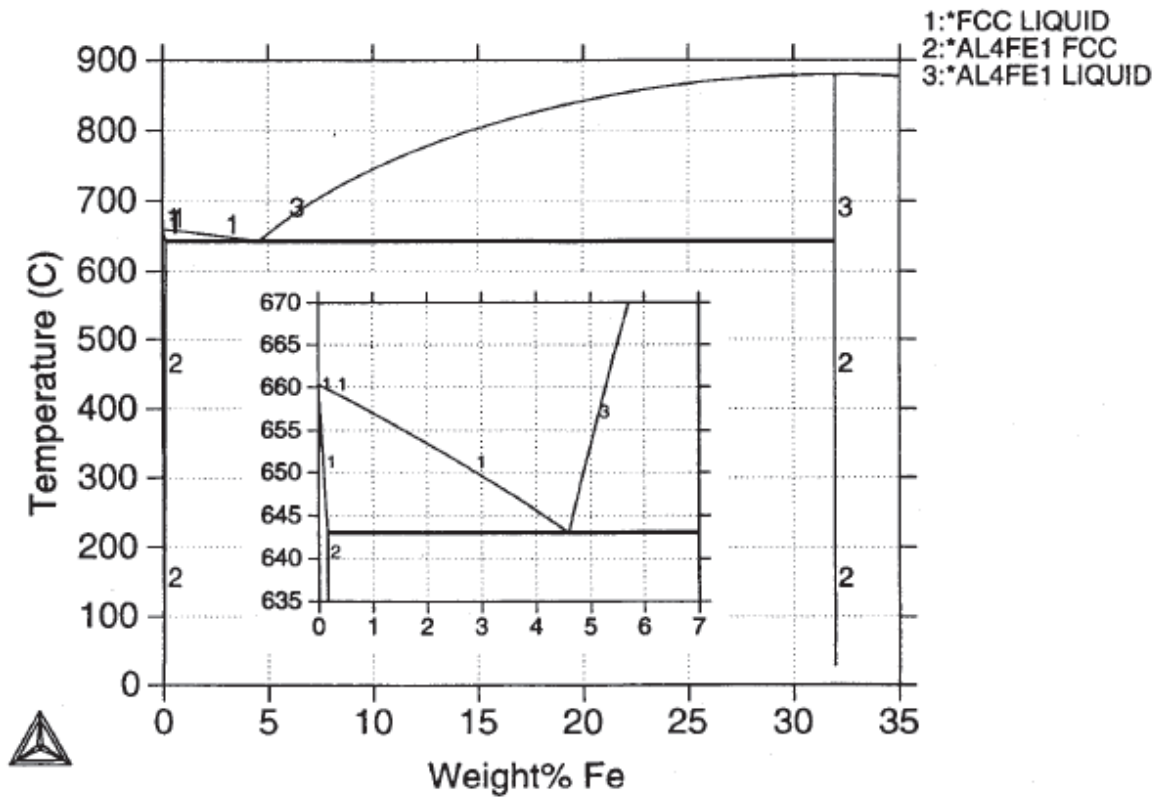
Figure 2.8: Al-Fe phase diagram computed for the Al-Al$_m$Fe equilibrium [12].
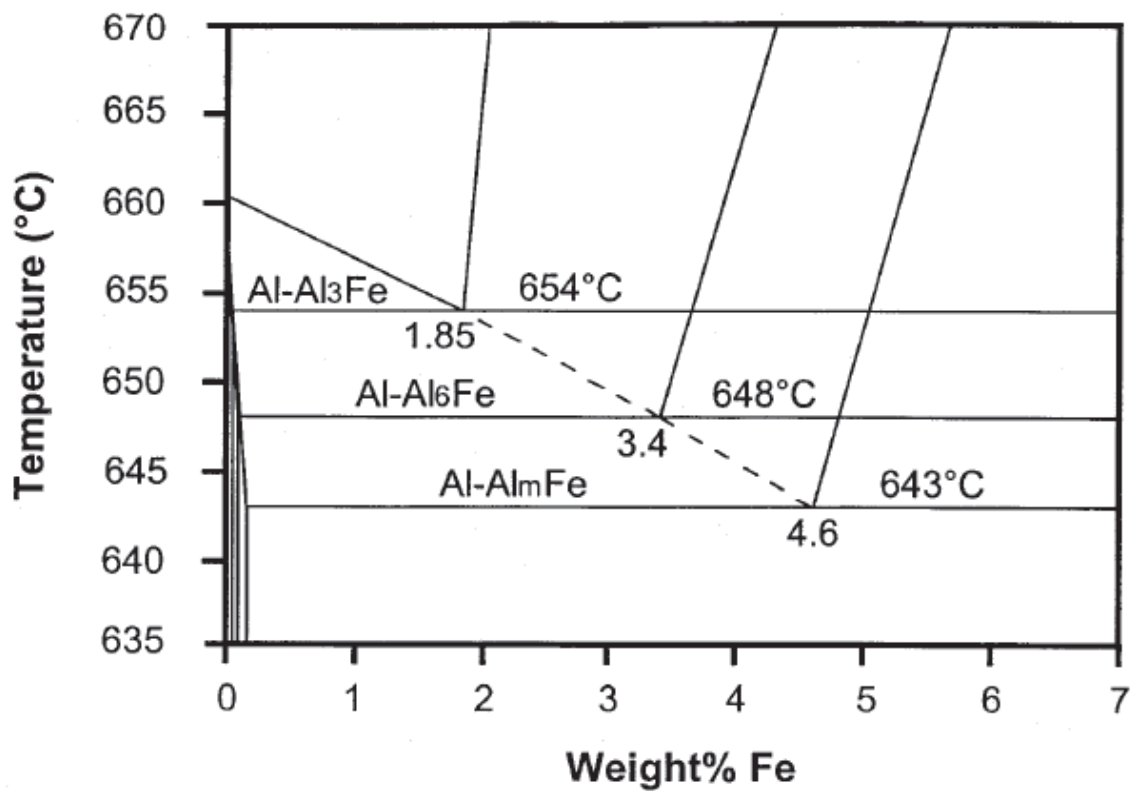

Figure 2.9: Superposition of the enlarged Al-rich ends of the three Al-AlFe phase diagrams [12].

2.2 Fir-tree Structure

Fir-tree structure, also known as Altenpohl-zone, is caused by formation of Al_mFe particles during casting [6]. During the anodising process, the aluminium is etched to achieve a matte homogenous surface and remove the natural oxide layer and scratches. The most common method for etching of aluminium is alkaline etching with caustic soda in aqueous solution. Different phases, such as Al_mFe and Al_3Fe, respond differently to chemical treatment [8]. If zones of Al_mFe grow into the ingot matrix and beyond normal scalping depth, there will be a defect on the finished anodised aluminium sheet, which is termed as streaking, see Figure 2.10. This results in an unacceptable anodising surface quality. Preventing surface defects related to Fir-tree structure can be achieved by either preventing formation of Al_mFe, to keep the zone smaller than the scalping depth or to move the zone into the bulk of the ingot. Cooling rate and chemical composition are parameters that are known to influence the formation of Fir-tree structure in one way or another, this will be discussed in Section 2.3.
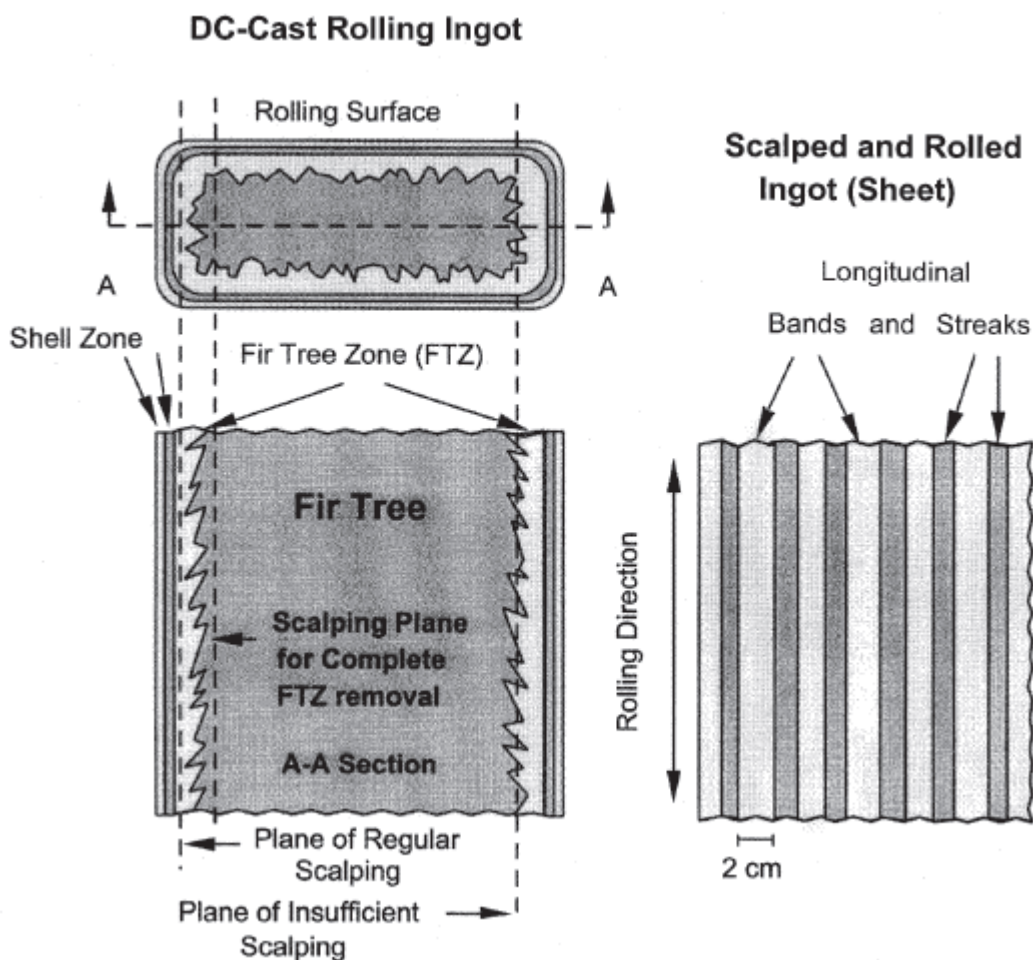
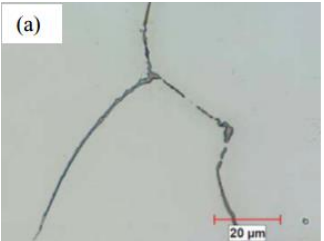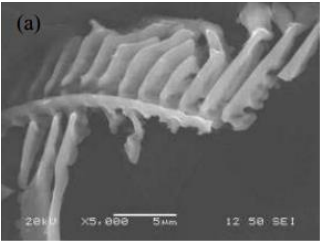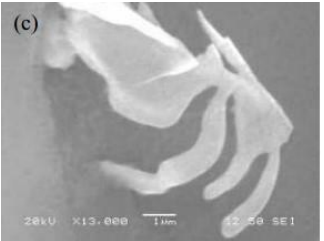Figure 2.10: Schematic illustration of Fir-tree structure formed in DC casting. Regular scalping depth is marked. If the regular scalping depth is insufficient, the anodised sheet will get the streaking defect. Streaking is illustrated to the right in the figure [12].

12

2.2.1 Nucleation and Growth Mechanisms of Intermetallic Phases

The different Al-Fe phases nucleate and grow in different manners and will therefore have different morphologies. This is illustrated in Table 2.2, which shows the morphology of Al_mFe, Al_3Fe and Al_6Fe in both plane polished and deep etched samples [24]. The phases are found in an AA5657 DC cast ingot. In principle, will the presence of Si in addition to Fe, lead to formation of ternary Al-Fe-Si compounds. In alloys with 0.09 wt% Si, approximately 93% of the Si will be existing as solute in the aluminium phase after solidification and the remaining Si will not be sufficient to form ternary intermetallic phases [23]. The alloy studied in this thesis has 0.0919 wt% Si, and descriptions of the ternary intermetallic particles are therefore not included in the theoretical background for this thesis.

Though Table 2.2 shows the characteristic morphology of the different phases, it is worth noticing that it has been reported that the morphology of the particles differs with the chemical composition of the alloy. For instance, Chen described the morphology of Al_mFe as feathery with many fibers growing in different orientations in AA1xxx [25], while Y. J. Li and L. Arnberg in their study described the morphology as skeletal and to consists of many coarse branches and irregular blocks in AA5182 [14].

Table 2.2: Key characteristic regarding morphology, nucleation and growth for different Al-Fe intermetallic phases [24].

	Al_mFe	Al_3Fe	Al_6Fe
Morphology in LM			
3D-morphology			
Description of Morphology	Feathery- like and possess many branches	Fiber- or needle-like	Flake-like with curved branches

13

The equilibrium phase Al_3Fe has a very complex crystal structure [23]. At higher cooling rates, there will not be sufficient time for atoms in the alloy to rearrange themselves to a stable solid phase with such a complex crystal structure. Therefore, less densely packed phases with simpler crystal structure will form. Crystallographic data for Al_3Fe, Al_mFe and Al_6Fe is presented in Table 2.3. The next subsections will give key characteristics regarding nucleation and growth for the three different phases.

Table 2.3: Crystallographic data for the different iron bearing particles [23].

Particle	Structure	Space Group	Lattice Parameters [Å]
Al_3Fe ($Al_{13}Fe_4$)	C-centered monoclinic	C2/m	a = 15.49 b = 8.08 c = 12.48 β = 107.75°
Al_mFe	Body centered tetragonal	I$\bar{4}$2m / I4/mmm	a = 8.84 b = 21.6
Al_6Fe	C-centered orthorombic	Ccmm / Cmc2	a = 6.49 b= 7.44 c = 8.79

2.2.1.1 Al_3Fe Phase

$Al_{13}Fe_4$ is a more appropriate formula, however, the stable phase of the Al-Fe eutectics is most commonly referred to as Al_3Fe. The growth mechanisms for the phases can be explained by atomic attachment theories [23]. There are two different kinds of atomic attachments: continuous and lateral. Microscopically, aluminium grows non-faceted. On the atomic scale, the solid/liquid (S/L) interface is rough. This rough S/L interface allows the phase to easily grow normal to itself, by continuous attachment of new atoms. On the other hand, Al_3Fe grows faceted microscopically, but has a smooth S/L interface on the atomic scale. This results in strong anisotropic growth. It advances by the restrictive lateral growth mechanism, but the phase frequently branches to overcome the growth restrictions. With an increased temperature gradient, the tendency of branching reduces. It may need higher undercooling (ΔT) than aluminium to grow due to the lateral growth mechanism. Hence, Al_3Fe grows at temperatures a couple of degrees lower than aluminium. This allows the aluminium to overgrow Al_3Fe, resulting in irregular flakes for the Al_3Fe phase. The preferred growth direction for Al_3Fe is parallel to the heat flow. Al_3Fe nucleates heterogeneously on impurities in the melt. Studies have shown that aluminium is not an effective nucleation site for the phase. The phase has a strong tendency for twinning and stacking fault is common.

2.2.1.2 Al$_m$Fe Phase

The eutectic phase Al$_m$Fe is formed under highly non-equilibrium conditions. Though there have been performed a lot of research on the FTZ (Fir-tree zone) and the metastable Al$_m$Fe phase, the crystal structure and space group are not completely established yet. Two different space groups have been suggested by Skjerpe and Gjønnes, as presented previously in Table 2.3.

Studies of the nucleation of these intermetallic phases have been few and there is a lack of knowledge, particularly concerning the phase Al$_m$Fe. X.G. Chen has studied the growth morphologies and nucleation behaviour of different iron bearing particles in DC cast AA1xxx alloys [25]. In his article he reported that a transition from Al$_3$Fe to Al$_m$Fe could be observed from SEM micrographs, which indicated that Al$_m$Fe can nucleate from already existing Al$_3$Fe and grow further. He explained this by the different temperatures for the two eutectics: Al$_3$Fe has a higher eutectic temperature and will form first in the interdendritic liquid during solidification and Al$_m$Fe follows at a lower temperature. Chen's research also showed that Al$_m$Fe can nucleate from an agglomeration of a few particles, which proved to be a compound with a high Ti-concentration.

A. Aliravci discussed in his study of Al$_m$Fe and FTZ, that Al$_m$Fe can nucleate on multicell boundaries, where the liquid is enriched in solute and the constitutional undercooling is at a maximum [23]. From the nucleation site, it seems like four main branches grow. To change growth direction and adjust the eutectic spacing, secondary, tertiary and quaternary branches grows out from the main branches. The morphology of Al$_m$Fe is commonly described as either dendrite-like, feathery or skeletal. Microscopically, Al$_m$Fe grows non-faceted, which results in semi-spherical tips. Since primary Al forms first during solidification, Al$_m$Fe is forced to grow in in channels between Al dendrites, which is the reason why the phase appears with a complex structure. If there is a more continuous growth path, the phase can grow as thin sheets. Consequently, the morphology of Al$_m$Fe will be influenced of the microstructure by Al. The Al dendrites will be coarse-equiaxed at low growth velocity and fine-equiaxed at high growth velocities. The phase can curve and enclose the Al dendrites. If two branches grow in the same interdendritic channel, they can meet and stop each other's growth. A new nucleation on a multicell boundary must then occur. Aliravci reported that the presence and a high level of Si, low temperature gradient and high growth velocity will promote the formation of Al$_m$Fe. He suggested that DC casting of AA1050 should be performed with high superheat to increase the temperature gradient and that the alloy should have less than 0.07 wt% Si, to prevent Al$_m$Fe to form.

2.2.1.3 Al_6Fe Phase

Al_6Fe was first believed to be the phase that caused the FTZ. Just like Al_mFe, it is a phase which forms under non-equilibrium conditions. It requires higher undercooling than Al_3Fe, but not as high as Al_mFe. It has been shown that Al is an active nucleation site for Al_6Fe [23]. Aliravci found that a high temperature gradient is essential for Al_6Fe to form. Microscopically, Al_6Fe grows between faceted and non-faceted. With increased cooling rate, the tendency for non-faceted growth increases. The morphology has both been described as rod-like and flake-like with curved branches. The phase cannot dissolve any Si.

2.3 Eutectic Phase Selection

2.3.1 Effect of Cooling Rate

Earlier studies have showed that the different Al-Fe compounds are formed at certain cooling rates. As discussed earlier, DC-casting causes different cooling rates as a function of distance from ingot surface. Consequently, zones with different Al-Fe compounds across the ingot thickness can be expected. Miki et al. reported the following relationship between cooling rate and phases formed in a 1xxx aluminium alloy [6]:

$$< 1 \text{ K/sec: } Al_3Fe$$
$$1\text{-}10 \text{ K/sec: } Al_6Fe$$
$$> 10 \text{ K/sec: } Al_mFe$$

Thus, the formation of Al_mFe, is promoted by high cooling rates, i.e. high casting speed. However, different researchers have reported different critical cooling rates for the formation of Al_3Fe, Al_6Fe and Al_mFe in Al-Fe and Al-Fe-Si alloys [23]. In one study, the critical cooling rate for formation of Al_mFe and Fir-tree structure was for AA1050 (0.25 wt% Fe, 0.13 wt% Si, 0.03 wt% Ti) and AA5005 (0.43 wt% Fe, 0.13 wt% Si, 0.85 wt% Mg, 0.03 wt% Ti) determined to be 8 K/s and 8.5 K/s, respectively [23]. The various researchers have reported the same trend: at the lowest cooling rates, the stable Al_3Fe phase form. At higher cooling rates, the metastable Al_6Fe phase form and that the metastable Al_mFe phase form at even higher cooling rates.

Experiments performed with an aluminium alloy with 0.24 wt% Fe and 0.02 wt% Si, have showed that the Fir-Tree structure disappears when the casting speed is lowered from 80 to 60 mm/min [8]. By lowering the casting speed, one can avoid exceeding the critical cooling rate for formation of Al_mFe. Trials have shown that the critical casting speed is between 60 and 80 mm/min, which can vary with the ingot dimensions [8]. The reason why Al_mFe is favoured at high casting speed, can be explained by the relationship between (i) cooling rate, (ii) nucleation temperature and (iii) growth temperature.

For a given cooling rate the phase with the highest precipitation temperature will nucleate first and start to grow [6]. The binary metastable Al-Fe phase diagram shows that Al_3Fe has the highest nucleation temperature, see Figure 2.11 a). However, the cooling rate will affect the nucleation temperature as shown in Figure 2.11 b). Al_mFe has the highest nucleation temperature at high cooling rates. Thus, high cooling rates promote formation of Al_mFe.
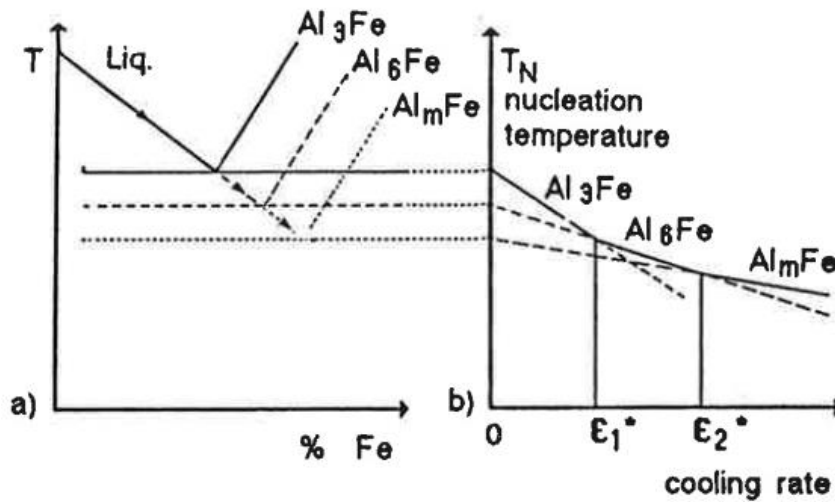

Figure 2.11: a) Al-Fe phase diagram b) Effect of cooling rate on the nucleation temperature [6].

Increasing cooling rate gives increasing growth velocity of the eutectic phases. Figure 2.12 shows how growth temperature of different eutectic phases are influenced by growth velocity. The eutectic phase with the highest growth temperature will dominate in a system where there are several intermetallic phases competing [14]. Figure 2.12 also shows that at increased cooling rate, Al_mFe has the highest growth temperature. Hence, Al_mFe will dominate at high cooling rates.
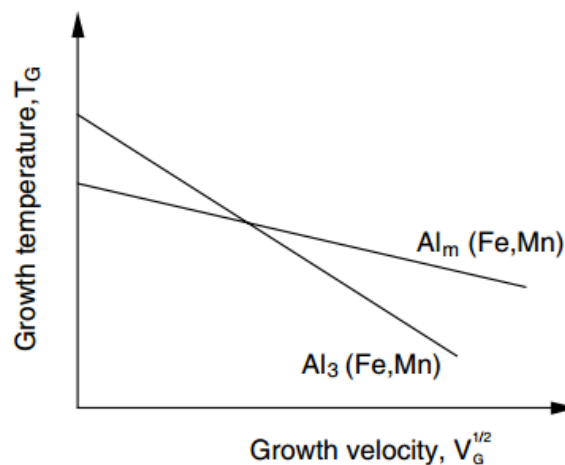

Figure 2.12: Schematic diagram of the influence of growth velocity on the eutectic growth temperature of Al_3(Fe, Mn) and Al_m(Fe, Mn) [14].

17

2.3.2 Chemical Composition

Previous studies have shown that the formation of the Fir-tree structure does not only depend on solidification velocity and/or the cooling during solidification. Impurity elements can influence the phase selection by providing nucleation sites and alter growth kinetics for a given phase [26]. To study the effect of impurity elements is not straight forward, since there are variations in purity, solidification parameters and bulk composition between different research studies. Elements which are not strongly partitioned in the interdendritic liquid during solidification, are not believed to influence the phase selection at low levels (<500 ppm). On the contrary, elements which are strongly partitioned to the interdendritic liquid during the final stage of solidification, can influence the phase selection even at very low levels. Allen et al. [26] made a summary of the results by different researchers of how different trace elements effect phase selection in high purity alloys, see Table 2.4.

Table 2.4: Effect of trace elements on phase selection in high purity alloys [26].

Phase	Phase promoted (+) or inhibited (-)	Elements
Al_3Fe	+	Mg, Cu, V, Ti, Ca
Al_mFe	+	Si, Cu, V, TiB$_2$
	-	Mg
Al_6Fe	+	Mn
	-	Si

Otani et.al performed a study to see how different trace elements influenced the formation of the Fir-tree structure [11]. Lithium, beryllium, potassium, barium and calcium were added in the amount of 0.01 wt% and with exception of the last element, they all gave approximately the same Fir-tree height. The addition of calcium gave a significantly increased Fir-tree height. Follow-up studies showed that the height was maximized at a calcium level of 0.005 wt%, see Figure 2.13. An amount above 0.03 wt% gave the same height as when no calcium was added.
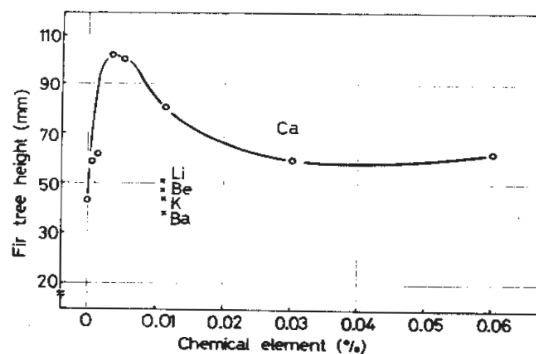

Figure 2.13: Fir-tree height as a function of amount of chemical element [11].

Brusethaug et al. reported that the the Fe/Si ratio has a major influence on the formation of Fir-tree structure [6]. They found that a Fe/Si ratio of 2 is the ratio giving the largest Fir-tree zone. A Fe/Si ratio of 2 is believed to give the lowest nucleation cooling rate threshold for Al_mFe. Lowering the ratio to 1 is not relevant as this has proven to be unacceptable with respect to grain structure of rolled sheet. To avoid the formation of the Fir-tree zone, the Fe/Si ratio should therefore be increased to a level of 3. Brusethaug et.al reported that the Fir-tree zone was eliminated by increasing the Fe/Si ratio from 1.8 to 5. Their study also showed a correlation between Al_mFe as the dominant primary constituent and the appearance of Fir-tree structure. Other researchers have also looked into the effect of Si on the formation of Al_mFe [26]. Al_mFe is promoted in Al-0.3 wt% Fe-0.1 wt% Si with Al-Ti-B addition (grain refiner). In the absence of Si, Al_mFe is not promoted. Al_mFe is also promoted if Al-Ti-B or Al-Ti-C grain refiner is added in Al-0.3 wt% Fe-0.1 wt% Si with approximately 100 ppm V.

Allen et al. and Zhang et al. have studied the influence of V on phase selection. Both studies reported that V promotes formation of Al_mFe. Allen et al. found that typical content of V in commercial alloys (10-100 ppm) combined with a 1:1000 addition of Al-B-Ti addition (Al-0.3Fe-0.1Si), promotes formation of Al_mFe [26]. In the study, Al_mFe did not form in grain refined DC cast alloy with low level of V. Zhang et al. also reported that V strongly encourages Al_mFe phase, but at higher V levels [13]. In the study, the content of V was gradually increased in AA5657. In the material with lowest content of V (170 ppm), the volume fraction of Al_mFe drops from 20 to 40 mm in distance to surface, see Figure 2.14 At higher levels of V, the drop in Al_mFe disappears. However, by increasing the level of V, the fraction of Al_mFe increases in positions with lower cooling rates.
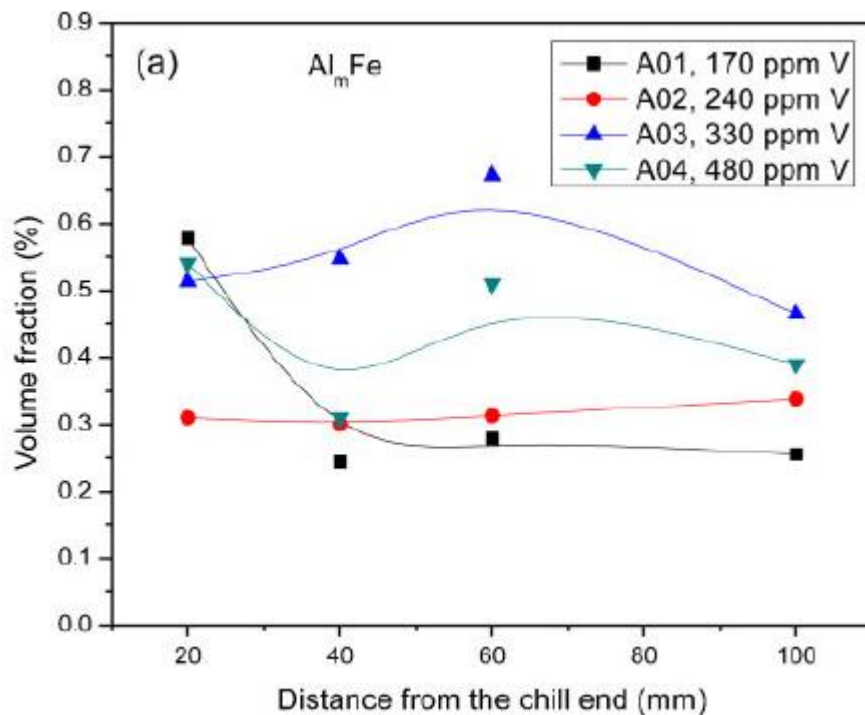

Figure 2.14: Distribution of Al_mFe at different levels of V [13].

Zhang et al. also studied the influence of Ni level on the phase distribution of iron bearing particles. From the study, it was clear that the volume fraction of Al_mFe decreased with increased content of Ni [13]. At the same time, it was evident that the volume fraction of Al_3Fe increased with increased content of Ni, see Figure 2.15. The effect of Ni on eutectic phase selection was discussed with basis in competitive nucleation and growth theory. The EDS-analyses of Al_3Fe particles, did often show presence of Ni. This indicates that the interdendritic region, enriched with Ni, acts as favourable nucleation sites for Al_3Fe. It has been suggested that impurities can promote twinning by providing higher density of edges and corners, which atoms more easily can attach to [26]. This will again promote the faceted phase Al_3Fe, which has strong tendency for twinning, as mentioned in Section 2.2.1.1.
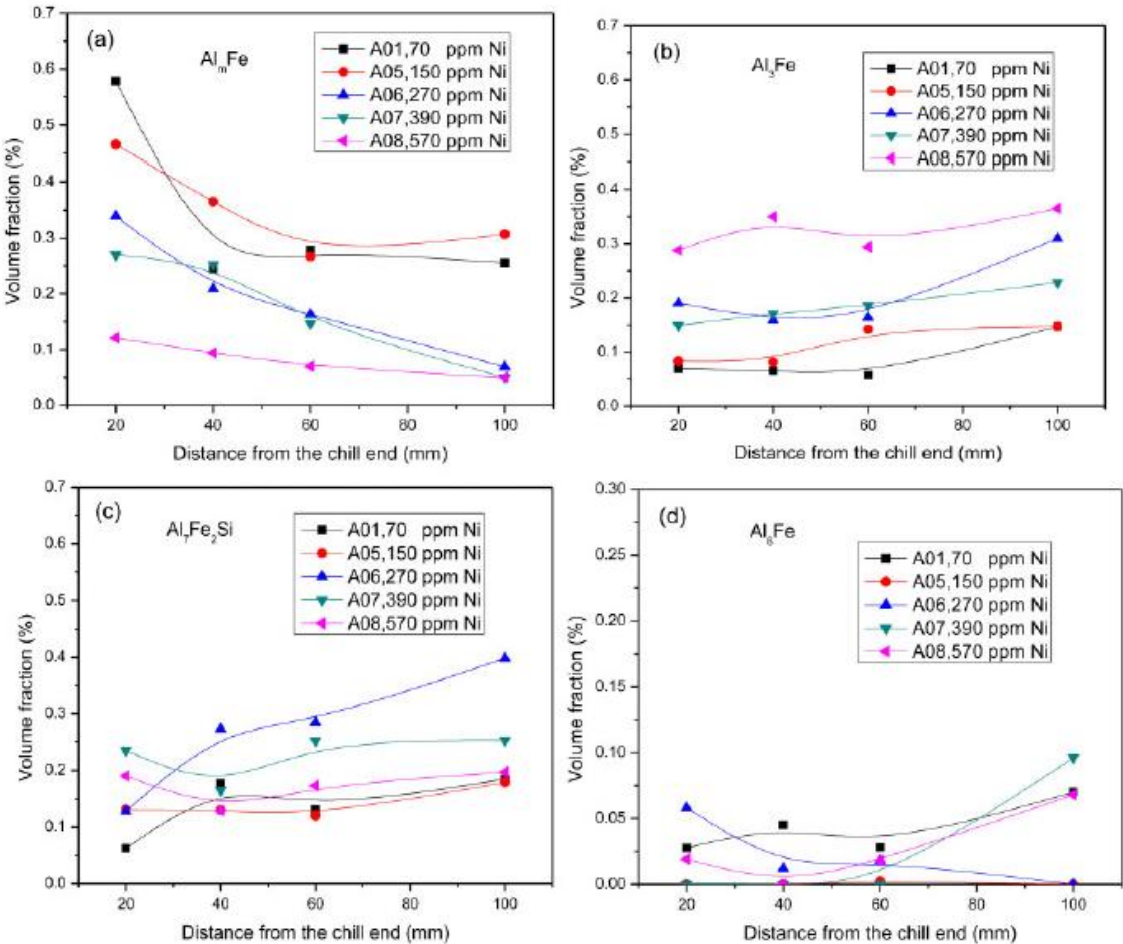
Figure 2.15: Distribution of different iron bearing particles at different Ni levels a) Al_mFe, b) Al_3Fe, c) Al_7Fe_2Si, d) Al_6Fe [13].

2.4 Techniques to Distinguish Different Iron Bearing Particles

In order to study the cause of Fir-tree structure, reliable phase identification is essential. Extensive research efforts have been made to understand what influences the phase selection between the different iron bearing particles during DC casting, but there are still challenges with distinguishing between the different phases. The iron bearing particles have very similar chemical composition and are usually very small, which make reliable phase identification difficult. Earlier studies have identified the particles by morphology and chemical composition, but due to the complex shape of the phases, only a small fraction of the particles will display the distinct morphology [13]. In addition, Al_mFe and Al_6Fe have very similar characteristic morphology, which makes it difficult to distinguish between the two phases even though the characteristic morphology is displayed. In addition to traditional imaging of the plane polished material by light microscope (LM) and scanning electron microscope (SEM), deep etching is a commonly used technique to reveal the 3D-morphology of the particles. Morphology studies of intermetallic phases can more easily be conducted with deep etched samples.

Energy dispersive spectroscopy (EDS) has been used to determine the chemical composition of particles with characteristic morphology. Recent studies have also applied electron backscatter diffraction (EBSD) technique to distinguish between the different iron bearing particles [27], [13], [24]. The particles have been identified by powder XRD measurements. Then the particles are first extracted from the aluminium matrix. Crystallographic data for the particles of interest must be known to identify particles by EBSD and XRD. Basic crystallographic data for the expected phases in this study, Al_mFe, Al_3Fe and Al_6Fe, could be seen in Table 2.3. Information regarding atomic positions and occupancy for each phase can be found in Appendix 1.

A combination of the different techniques mentioned will increase the reliability of the phase identification. It is necessary to have good insights in the methods to understand the different method's advantages and limitations. Therefore, the next subsections will give a brief introduction to the relevant techniques used in this project.

2.4.1 EBSD

The electron backscatter diffraction (EBSD) technique is based on acquisition of diffraction patterns from a bulk sample in a SEM. The acquired electron backscatter pattern (EBSP) is unique for an individual phase. It is defined by the crystal's lattice parameters and orientation. Therefore, the technique can be applied for phase identification and distribution, as well as achieving information about grain size, grain orientation, character of grain boundaries and texture [28]. The wavelength of the incident electron beam and the proximity of the EBSD detector to the sample will also affect the EBSP.

EBSD is carried out by studying a flat, highly polished sample [28]. The sample surface must be well polished and free of deformation. Sometimes it is necessary to carry out chemical or electrochemical polishing to remove surface deformation caused by mechanical polishing. Other final steps can also include ion milling or vibration polishing.

During EBSD, the sample is tilted 70° (20° with the incident electron beam) to ensure interaction close to the surface, thus reducing the number of absorbed electrons [29]. At the point where the incident electron beam impinges the sample surface, the electron beam will interact with the crystal lattice. Beneath the surface, the electron beam is inelastically scattered in all directions. As a consequence, there are always some electrons that satisfy the Bragg angle of every plane in the crystal:

$$n\lambda = 2d\sin\theta \qquad (1.14)$$

Where

n: An integer

λ: Wavelength of the electrons

d: Interplanar spacing for a given set of lattice planes

θ: Bragg angle

These electrons will form two diffraction cones for each lattice plane, see Figure 2.16 [15]. In the EBSP this will appear as parallel lines, known as Kikuchi bands. When a phosphor screen is placed in the path of the diffracted electrons, the EBSP can be seen since the phosphor screen will convert the diffracted pattern into light [28], [30]. This can be recorded by a CCD camera.
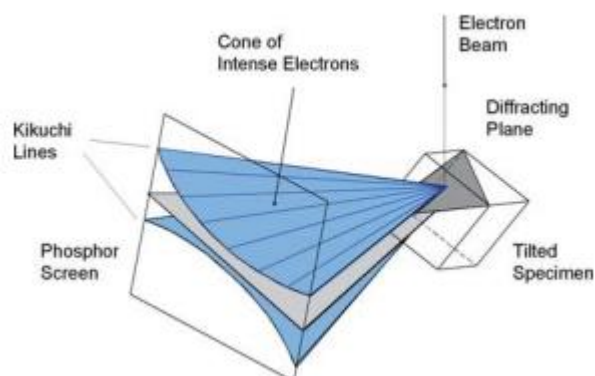
Figure 2.16: Schematic illustration of the formation of Kikuchi lines [15].

The center of a Kikuchi band represents the virtual intersection between a lattice plane with the screen [29]. Intersections of bands correspond to intersection of planes and gives the zone axes in the crystal [15], [29], [30]. The angles between the Kikuchi bands represent angles between planes, while the band width is inversely proportional to plane spacing (d). The calculated angle between the Kikuchi bands are compared to a list of interplanar angles of known structures, to find the solution with the best fit.

The fit parameter is a part of the indexing procedure and is a measure of the average angular difference between recalculated bands and detected bands [2]. Another parameter that is calculated during automatic indexing of a diffraction pattern, is the confidence index (CI). For one EBSP, there can be several orientations which satisfy the diffraction bands. The CI-value describes how reliable it is that the EBSP is correctly indexed. The software ranks the different solutions by a voting scheme. The CI is defined in Equation (1.15).

$$CI = \frac{V_1 - V_2}{V_{IDEAL}} \hspace{4cm} (1.15)$$

Where

V$_1$ and V$_2$: Number of votes for the solutions with most and second most votes

V$_{IDEAL}$: Total possible number of votes from the detected bands

CI is a value between 0 and 1 [2]. It should be noticed that if V$_1$ equals V$_2$, CI is 0. This does not necessarily mean that pattern is wrongly indexed. If an EBSP cannot be indexed, it results in a CI equal -1. Figure 2.17 shows the correlation between CI and the probability for correct indexed EBSP for a fcc material. It can be seen that with a CI of 0.1 or greater, the probability of correct indexing is 95%.
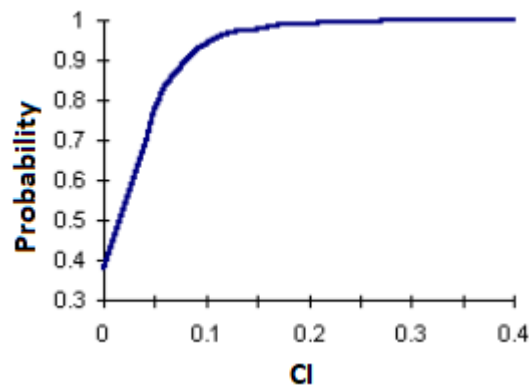
Figure 2.17: The correlation between the probability for correct indexing and CI for a fcc material [2].

To perform automatic EBSD mapping, image analysis techniques have been developed. One well known technique is the Hough transformation. This transformation reduces all lines in real space to a single point in Hough space, see Figure 2.18 [30], [1]. The relationship is given in Equation (1.16). Through Hough transformation, the bands positions and angles are detected. This allows the Kikuchi bands to be indexed by Miller indices. Hence, the crystal structure and orientation can be determined.

$$\rho = x \cos \omega + y \sin \omega \qquad\qquad (1.16)$$

Where

ρ: The length of the normal to the line and origo

ω: The orientation of ρ with respect to the x-axis
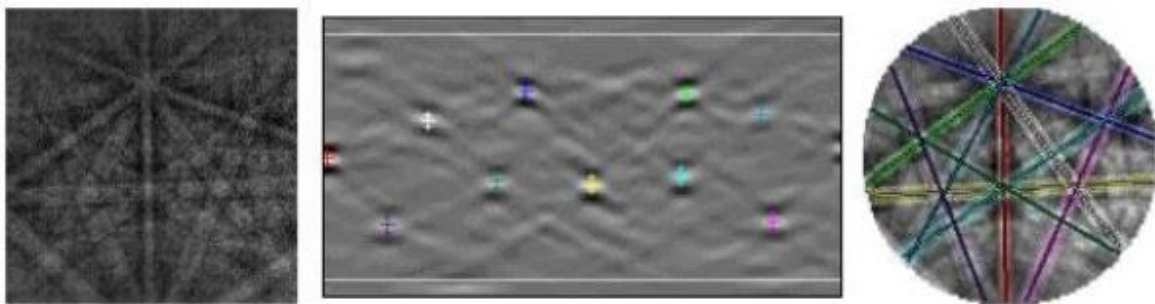
Figure 2.18: The Kikuchi bands are detected through Hough transformation [1]

For phase identification by automatic indexing, the diffraction patterns must be of high quality. It can be a challenge to achieve patterns with high enough quality to index. Some EBSPs can have a high level of noise, resulting in a large fraction of non-indexed or misindexed patterns in an EBSD map [31]. This can be due to the material itself or the EBSD detector. If the material has a high degree of deformation or is fine grained, the interaction volume can be too large and the resolution too poor to achieve patterns with good enough quality, giving noisy EBSPs. Sometimes it is desired to collect the data with high speed. This can be achieved by adjusting gain and exposure time, but this tends to give degraded pattern quality. A new method developed to increase pattern quality is *averaging* [32]. With averaging, several diffraction patterns are acquired from the same point and the average intensity is used. The number of diffraction patterns that can be included is between one and five, where the quality increases with increased number of summed diffraction patterns. However, the time to accomplish an EBSD map also increases with increased number of summed patterns. With good pattern quality, phases can be identified by EBSD if the crystallographic data for the expected phases is known.

2.4.2 X-ray Microanalysis

When a sample is studied in SEM, a focused electron beam scans over the sample to create an image. The electrons will always interact with the sample and produce X-rays [33]. The energy of an X-ray is distinct for each element and can therefore be used to determine the chemical composition of the sample. The wavelength of the X-rays is also characteristic for each element and related to the energy of the X-ray as given in Equation (1.17):

$$\lambda = \frac{hc}{E}$$
(1.17)

Where

λ: Wavelength of the X-ray

h: Planck constant

c: The speed of light

E: The energy of the X-ray

That means there are two different methods for chemical composition measurement of particles in a sample: analyzing the wavelength of the X-rays emitted from the particle (WDS) or by measuring the energy of the X-rays (EDS).

WDS (wave length dispersive spectrometry) relies on Bragg diffraction from an analyzing crystal with known lattice planes (d) [33]. Some X-rays will leave the sample and be incident on the analyzing crystal with an angle θ, see Figure 2.19. X-rays with a wavelength that fulfills Bragg's law will then be diffracted, the rest will be absorbed or pass through and be lost. An X-ray detector, usually a gas proportional counter, will then be triggered and records the X-ray [34]. At a specific position of the analyzing crystal, only one wavelength can fulfill Braggs law. Consequently, only one element can be analyzed at one time. By changing the position of the crystal, Bragg's angle changes and another wavelength is allowed to fulfill Bragg's law. Thus, analyzing a different element. By knowing the angle and lattice plane, one can calculate the wavelength and the energy of the X-ray. The concentration of the elements is determined by the count rate. In this way, an X-ray spectra can be achieved.
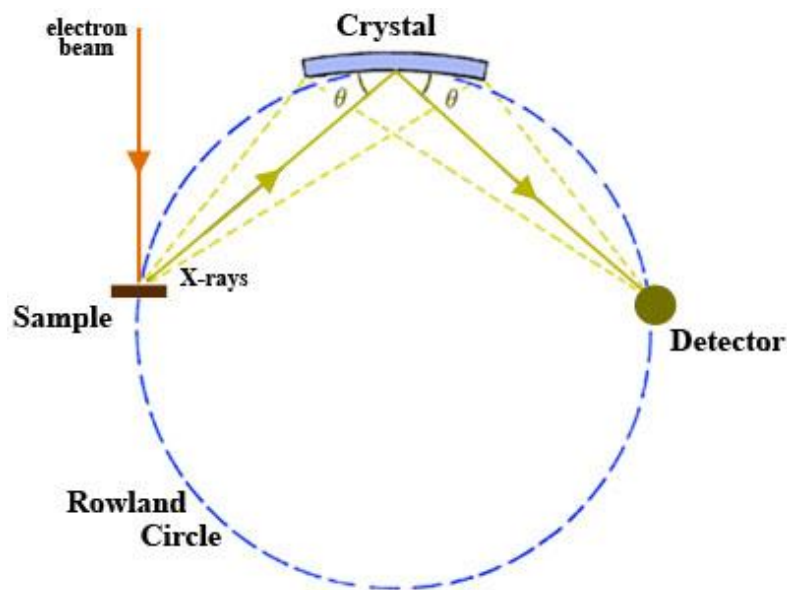
Figure 2.19: Schematic illustration of wavelength dispersive spectrometer [5].

EDS (energy dispersive spectrometry) on the other hand, is a method that records almost all X-ray energies at one time. The X-rays which are emitted from the sample, are directed to a detector at a fixed position. The X-rays are dispersed by electronic processing equipment, using a pulse-height analysis equipment [34]. The measured height of a pulse is related to the energy of the X-ray.

WDS and EDS are clearly quite different methods, hence the performance and preference of application will differ. EDS is used to identify elements and can be used in a semi-quantitative manner by measuring the intensities of the identified elements [29]. It can give a full element spectra within seconds, but peaks from different elements can overlap. A certain background knowledge of the chemical composition of the sample should therefore be considered when interpreting the spectra. In addition, light elements, such as boron, cannot be identified by EDS. Since WDS only can analyze one element at the time, it takes longer time and it also require special expertise to operate. However, WDS is more suitable for quantitative analysis [34]. Compared to EDS, WDS has higher spectral resolution and a lower detection limit. Lighter elements can more easily be detected by WDS. To achieve quantitative analyses with WDS, the measured intensity must be adjusted according to a standard reference sample [29]. The intensity of a reference sample is compared to the intensity of the sample. By knowing the intensity ratio reference/sample, it can be adjusted for atomic number effect (Z), self-absorption effect (A) and fluorescence effect (F). This is known as ZAF-correction.

When using X-ray microanalysis to distinguish phases, it is essential that the detected signals only originate from the phase of interest and not from the surrounding matrix. In other words, a criterion for a successful quantitative analysis, is that the interaction volume is not larger than the particle itself. There is a correlation between the material's density, applied acceleration voltage and diffusion range [29]. The diffusion range increases with applied acceleration voltage, while it decreases with the density of the phase.

Zhang et al. [24] explored the possibility to use a combination of EBSD and EDS to get reliable phase identification of the iron bearing particles. In the study, six SEM-images were taken at 200X magnification for each sample, giving approximately 80-100 particles per image. Every particle was identified before an image analysis program was used to determine the volume fraction of each phase. The particles were identified by entering the crystallographic data for the phases from Pearson's Handbook to a customized Channel 5 software.

2.4.3   Extraction of particles

For EDS and WDS analysis on small particles, there is a risk that the interaction volume is larger than the particle itself. A solution to this can be to extract the particles from the aluminium matrix. To extract particles from aluminium alloys has proved to be a challenge, as most of the particles dissolve more easily than the aluminium matrix [35]. Different dissolution processes have been developed and A.K. Gupta et.al reviewed some of the most popular methods, including both chemical and electrochemical methods. In the latter method, the aluminium is immersed in a proper electrolyte. To dissolve the aluminium, the sample must act as an anode, while a more noble material must be a cathode. A potential at which the aluminium dissolves, but particles are insoluble, is applied. To figure out what is the correct conditions is quite a time-consuming process. This project is related to a problem that can occur in a commercial aluminium alloy and will therefore focus on a chemical dissolution method that is economical and quick.

From the review of A.K. Gupta et al., the most promising methods for extracting the particles of interest in this project (Al_6Fe, Al_mFe and Al_3Fe ($Al_{13}Fe_4$)) are the butanol- and phenol-method, see Table 2.5 for review of the two procedures. The butanol-method is a technique developed by SINTEF for selective matrix dissolution in commercial aluminium alloys. The method has been shown to give very good results for separation of intermetallic compounds [36]. Relatively short dissolution time is needed, but the preparation time in advance is long; the residual particles are collected on a filter and this filter needs to be washed in butanol for a long time to avoid hydroxide formation. The butanol also needs to be double distilled. In addition, the technique requires a special setup, where the glassware needs to be thoroughly cleaned ahead of each extraction. Altogether, this makes the butanol-method an expensive and time-consuming process.

In commercial settings, a more economical method is desired. The phenol method seems to be a more suitable method for this project. Aluminium is dissolved in boiling phenol by the following chemical equation [37]:

$$3C_6H_5OH + 2Al \rightarrow 2Al(C_6H_5O)_3 + 3H_2 \qquad (1.18)$$
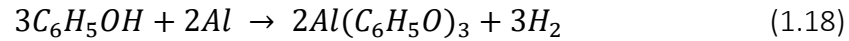
This method for extracting intermetallic particles was first described by Sato and Izumi [38]. It was reported that the procedure caused aluminum phenolate to form and contaminate the particles when larger samples were dissolved. Gupta et. al modified this method to avoid formation of aluminium phenolate [35]. When the sample is completely dissolved in phenol, the solution is treated with benzyl alcohol. Sato and Izumi let the solution cool to room temperature before the solution with the residue was centrifuged, while the modified method by Gupta et.al centrifuged the solution while still warm. It was reported that this would restrict the formation of aluminium phenolate. The modified method suggests that a 3 g sample is dissolved in 50 mL of boiling phenol and treated with 120 mL of benzyl alcohol immediately after completion of dissolution. It also proposed that a sample should consist of several thin sheets (10 mm x 25 mm x 0.1-0.2 mm) to get short dissolution time.

The principle for deep etching is the same as for extraction of particles; the sample is immersed in a solution which will dissolve the aluminium matrix, but not the intermetallic particles. Under deep etching, it is only desired to dissolve the aluminium matrix in the surface layer [25]. This leaves the intermetallic particles free at the surface, allowing studying of their 3D-morphology. Zhang et.al have performed deep etching in NaOH (10-15%) at 60-70°C, having the same intermetallic particles of interest as in this project. Deep etching is a fast and easy method to enable studying of 3D-morphology. Deep etched samples are only suited for imaging. In order to perform EDS or WDS analyses on deep etched samples, particles with a planar surface have to be found, which is difficult.

Table 2.5: Two chemical methods for extraction of intermetallic particles in aluminium alloys, reproduced after Gupta et al. [35]

Chemicals	Procedure	Conditions	Residue treatment	Phase identified	Remarks
1-Butanol	The sample is dissolved in distilled and dried 1-butanol at 117°C in an inert atmosphere	0.3-5.0 g 117°C 2 h	The residue particles are collected by separation	Al(Fe,Si) types, Al_8Fe_2Si, $Al_{13}Fe_4$, $Al_6(Fe,Mn)$, Mg_2Si, Al_xFe, $AlMnSi$, $Al_{12}Mn$, $AlCuMgSi$ type, $CuAl_2(?)$	Requires special setup. Dissolution time is longer in the presence of high Mn and Cu in the material. Not a routine process. Expensive.
Phenol	The sample is dissolved in 120 mL of boiling phenol.	0.3-6.0 g 182°C 10 min	Stop boiling phenol and add 80 mL benzyl alcohol; centrifuge the content for 10 minutes and decant the liquid; wash and centrifuge the residue a couple of times in benzyl alcohol several times and give at least two final washed in methanol	Al_3Fe, Al(Fe,Si) type, Mg_2Si, Al_6Fe, Al_mFe, $CuAl_2$, $Al(Fe,M,Si)$, $Al_5Cu_2Mg_6Si_6$, Si, $MgZn_2$, $CuMgAl_2$	Very simple process. Inexpensive, quick, and can be routinely used in the commercial environment. Phenol is acute toxic; the experiment must be carried out in a fume hood and with suitable protective clothing. Reported to isolate most of the intermetallic particles found in commercial alloys. Cannot be used to isolate fine aging particles.

When X-rays interact with a crystalline material, there will be a diffraction pattern. This diffraction pattern is unique for a substance and can therefore be seen as a fingerprint of a crystalline substance [39]. X-ray diffraction (XRD) is a non-destructive analyzing technique which utilizes the characteristic diffraction pattern of crystalline substances to determine size of crystals, identifying phases by comparing measurements with data from known structure. A quantitative analysis can also be performed by Rietveld Refinement.

X-rays are generated and directed to the sample through a slit of chosen size [39]. When the X-rays are incident on the sample, they are either transmitted or scattered by the electrons of the atoms in the sample. In the case of scattering, the X-rays are scattered in all directions. Constructive interference is when two different waves add to make a new wave with a larger amplitude. When constructive interference occurs, there will be a peak in intensity. Constructive interference occurs when Braggs law is fulfilled.

$$n\lambda = 2d_{hkl}\ sin\theta \qquad\qquad (1.19)$$

Where:

 n: An integer

 λ: Wavelength of X-ray

 d_{hkl}: Interplanar spacing between hkl planes

 θ: Incident angle

X-ray scattered from two adjacent planes in a crystal will constructively interfere when the path difference is an integer number of wavelengths, see Figure 2.20. From Equation (1.19) it can be seen that θ, the peak position, is dependent on cell parameters [39]. The peak intensity is related to chemical composition, which can be seen from Equation (1.20) and Equation (1.21). However, when analyzing samples which is a mixture of different phases, changes in intensity is also related to the amount of each phase. According to Scherrer equation, Equation (1.22), the width of the peaks is inversely proportional to the crystalline size. Several defects can cause line broadening, but small crystals are the most common one.
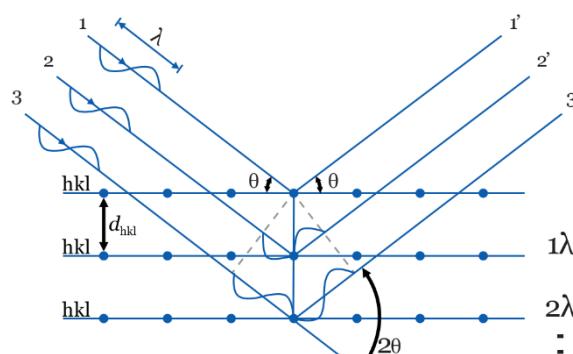
Figure 2.20: Bragg's law [3].

$$I \propto |F_{hkl}|^2 \tag{1.20}$$

$$F_{hkl} = \sum_i f_i exp 2\pi i(hx_i + ky_i + lz_i) \tag{1.21}$$

Where

    F_{hkl}: Structure factor of a reflection, hkl

    f_i: Scattering factor for atom i, which is related to atomic number

    x, y, z: Atom positions

$$L_{hkl} = \frac{\lambda}{\beta cos\theta} \tag{1.22}$$

Where:

    L_{hkl}: Crystallite size

    β: Peak width in radians

When a single crystal is measured, there is only one orientation and few reflections can be seen [39]. In powder diffraction, the material will be polycrystalline and have all possible orientations. This means that similar planes in different crystals will scatter in different directions, giving a characteristic diffraction pattern for each phase. When an XRD measurement has been performed, the peaks in the diffraction pattern needs to be identified. Phases are identified by peak position by comparing the measured multiphase diffraction pattern with a database of known phases. In the database, phases that are expected (e.g. Al_mFe, Al_3Fe, Al_6Fe) are included. Often, it is also desired to not only perform a qualitative analysis, but also a quantitative analysis. However, to determine the proportion of each phase in a multiphase sample requires further post-processing. There are several methods to do a quantitative analysis, Rietveld refinement is the method which will be used in this project. The identified phases give a theoretical calculated pattern. The calculated pattern is compared to the measured XRD pattern. In Rietveld refinement, the least squares method is used to minimize the difference between calculated and measured pattern, see Equation (1.23) [40]. The running index, i, represents the angular position in the powder pattern, see Equation (1.24).

$$Min = \sum_{i=0}^{n-1} \left(w_i \left(Y_{obs_i} - Y_{calc_i} \right)^2 \right) \tag{1.23}$$

$$2\theta_i = 2\theta_{start} + i\Delta2\theta \tag{1.24}$$

Where

    $Y_{obs,i}$ = Observed intensity

    $Y_{cxalc, i}$ = Calculated intensity

    w_i = Weight derived from the variance of $Y_{obs,i}$

    θ_{start} = Starting angle

    $\Delta2\theta$ = Angular step width

3 Experimental

3.1 Material

Hydro has provided this project with material. Twelve slices were cut from an AA5005 sheet ingot, where a minimum Fir-tree height of 59 mm has been measured from the rolling surface of the ingot. The dimensions of the ingot were 600 mm x 1600 mm. There were six slices from the top of the ingot and six slices from the bottom. The slices comprised an area going from the ingot surface of the rolling side and 14.6 cm into the material towards the center. The chemical compositions of the alloy are given in Table 3.1.

Table 3.1: Chemical composition of the alloy

Element	Mg	Si	Fe	Mn	Ti
Wt%	0.7286	0.0919	0.2823	0.018	0.0082

One slice from the top (T) of the ingot and one slice from the bottom (B) were randomly selected for characterization. Both slices were cut into nine samples of equal size using "Struers Labotom-5", see Figure 3.1. The numbered surface in Figure 3.1 shows the plane which was studied. The approximate distance to the surface is given in Table 3.2 for each sample.
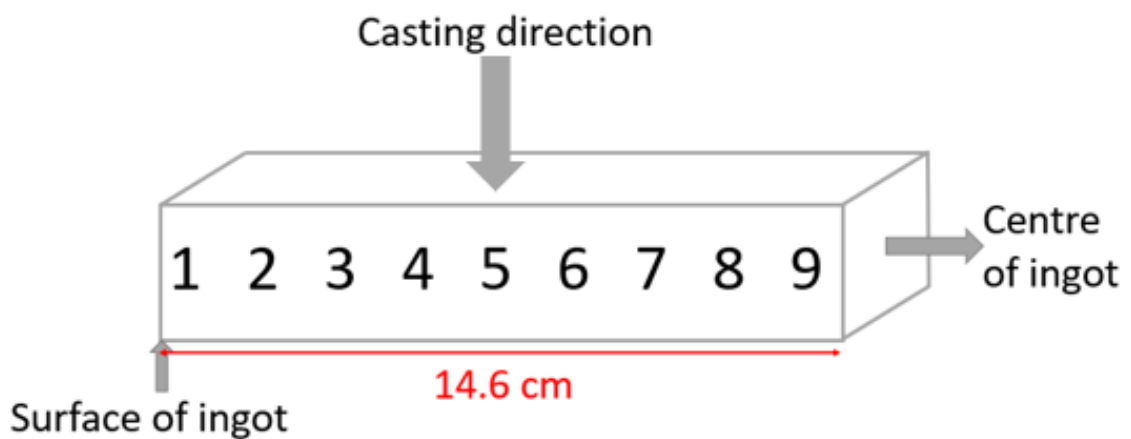
Figure 3.1: Position of samples with respect to the surface of the ingot.

Table 3.2: Showing the mean distance to surface (DTS) for each sample

Sample	1	2	3	4	5	6	7	8	9
DTS [cm]	0.8	2.4	4.0	5.6	7.2	8.8	10.4	12.0	13.6

33

3.2 Characterization of the Material by Studying Plane Polished Samples

The samples (B1-B9 and T1-T9) were cold mounted and ground on SiC paper (P500), using a "Struers RotoForce-4". After some trial and error, a polishing programme that gave a satisfying surface quality for characterization in LM and SEM was determined. The different polishing steps are listed in Table 3.3 and were carried out by using a "Struers Tegramin-30" with an applied force of 20 N.

Table 3.3: The different polishing steps used during sample preparation

Step	Polishing plate	Suspension	Time [min]
1	MD-Largo, 9 μm	DiaPro Allegro Largo 9	5
2	MD-Mol, 3 μm	DiaPro Mol 3	4
3	MD-Nap, 1 μm	DiaPro Nap B1	2
5	MD-Chem	OP-S Suspension	1

All 18 samples were studied in LM (LEICA MEF4M). The first set of images were taken with lower magnification (200x) to get an overview of the morphology of the iron bearing phases. This was the basis for acquiring pictures at higher magnification. At least three images were taken with both 500x and 1000x magnification.

The morphology of the iron bearing particles in the 18 samples were studied in a more detailed manner in SEM (Zeiss Supra 66VP). The aperture diameter was set to 60 μm and the accelerating voltage to 15 kV. Every sample was studied in the range of 200-1500x magnification in backscattered electron (BSE) imaging. A few close-up images were taken at even higher magnifications for some samples.

In order to relate possible changes in phase distribution with cooling rate, the samples were anodised so that the grain size could be measured in LM. This was carried out in HBF_4 (5%) for 1.5 minutes. The grain size of each sample was determined by the linear intercept method. Three images at 500x magnification were taken of each sample and three lines were superimposed on each image.

3.3 Phase Identification by EBSD Technique

To study if the iron bearing particles could be identified by the EBSD technique, samples with different distances to the surface of the ingot were selected (T3, T5, T8). An attempt to acquire EBSP from particles with a high-speed detector equipped on Zeiss Gemini Ultra 55 was made. This gave poor pattern quality and further work with phase identification by EBSD technique was carried out with a Zeiss Supra 66VP equipped with a high-resolution detector (NORDIF HR4M EBSD). The aperture diameter was set to 120 μm and the accelerating voltage to 20 kV. The sample was tilted 70° and the working distance was 20 μm. Electron backscatter diffraction patterns (EBSPs) were acquired for particles with characteristic morphologies, using NORDIF 3.0. One EBSP from the aluminium matrix in the proximity of the particle of interest were acquired and saved for calibration during indexing. In the software NORDIF 3.0, single patterns from particles and aluminium matrix are saved under the term "calibration patterns". The settings used for acquiring calibration patterns are given in Table 3.4.

Table 3.4: Settings used in NORDIF 3.0 for acquiring calibration patterns

Averaging [#]	5
Frame rate [fps]	7
Resolution [px]	410x410
Exposure time [μs]	142757
Gain	0

TSL OIM Data Collection 7 was used to index the patterns. When indexing particles in a particular area, a calibration was always performed first. This was done by tuning after indexing a pattern from the aluminium matrix acquired close to the particles. The expected intermetallic phases, Al_mFe, Al_3Fe and Al_6Fe, were not in the software's database. These phases were generated by the procedure given in "OIM DC 7.2 Manual" under the subsection "Tutorial – Material File", using the crystallographic data presented in Table 2.3 and Appendix 1. Settings in the software will affect the performance of the indexing. Different settings were tried and the optimum settings for identification of the iron bearing particles, are given in Table 3.5. These settings were used for all results present in this work. Solutions with a god *fit* were used for phase identification.

Binned Pattern Size	120
Convolution Mask	9 x 9
Theta Step Size	0.5°
Min/Max Peak Count	10/12
Min Peak Magnitude	5
Min Peak Distance	15

3.4 Phase Identification by WDS Analyses

T1, T3, T5, T7 and T9 were selected for WDS analyses using a JEOL JXA-8500F EPMA. An accelerating voltage of 10 kV was applied. For each sample, approximately 40 analyses were carried out on particles with different characteristic morphologies. The content of Al, Fe, Mg, Si, Mn and Ti in the particles were quantitatively analysed. An image was taken for every particle analysed, so that the chemical composition of the particle could be related to the morphology of the particle.

3.5 Study of Particles' 3D-morphology by Deep Etching Technique

Sample T1, T7 and T9 were chosen for further examinations by the deep etching technique. The samples were removed from the epoxy embedding and then ground to remove the anodised layer, before polishing manually on "Struers Tegramin-30", following the developed polishing programme. The samples were etched in NaOH solution (6 g/L, 1L) at approximately 70°C for 20 minutes. The experimental setup is shown in Figure 3.2. The deep etched samples were studied in SEM using secondary electron (SE) imaging. The aperture was set to 30 μm and the accelerating voltage to 10 kV. The samples were studied at different magnifications.

Figure 3.2: Experimental setup for deep etching in heated NaOH.

3.6 Extraction of Iron Bearing Particles from the Aluminium Matrix by the Phenol Method

To get quantitative analyses of the phase fractions, a new slice from the top of the ingot was randomly chosen for further studies by XRD. The iron bearing particles were extracted from samples with different distances to the surface by the phenol method. The mean distance to surface for each sample is given in Table 3.6. One sample consisted of several thin sheets, with approximate dimensions of 10 mm x 22 mm x 0.30 mm. The thin sheets were cut by using Struers Accutom-5, with a cutting speed of 0.100 mm/s. Enough sheets for samples of approximately 3.5 g were prepared, see Table 3.6. This corresponds to approximately 17 sheets.

Table 3.6: Position and mass of the seven samples

Sample	Mean Distance to Surface [mm]	Mass [g]
S1	7.5	3.37
S2	30.2	3.62
S3	51.5	3.41
S4	65.3	3.53
S5	78.8	3.58
S6	106.8	3.76
S7	134.7	3.17

The experimental setup for extraction of intermetallic phases by the phenol method is shown in Figure 3.3. A Liebig condenser cooled with water was attached to a two-neck round-bottom flask (250 mL). The other neck was plugged. The round-bottom flask was fastened by a clamp to ensure that the glassware was held in place. The glassware was placed in a heating mantle. For safety reasons, the heating mantle was placed upon a jack. If something unexpected happened during the experiment, the glassware could be removed immediately from the heating source by moving the jack.

60 g of solid phenol was melted in the flask and heated to the boiling point (182°C). The plugged neck was opened, and all the sheets of S1 was added to the boiling phenol, resulting in large gas generation. The heat was turned off and the experiment was paused until all the gas had been sucked away in the fume hood. In this time, some of the solution solidified. The solution was heated again and gently boiled until the dissolution was complete. Benzyl alcohol (120 mL) was added immediately.

Only two centrifuge tubes of the size 145 mL were available. The solution was therefore split into two centrifuge tubes. The round-bottom flask was washed with some more benzyl alcohol to ensure that all particles were transferred to the centrifuge tubes. Then the solution was centrifuged while still warm, using "Centrifuge VWR Mega Star 600". The solution was centrifuged at 4350 rpm (the upper limit for the centrifuge) for 20 minutes. The residue had not completely sedimented after centrifuging and the discarding needed to be performed very carefully. Benzyl alcohol was added to the tubes until they were approximately half full, centrifuged and separated again. This was performed one more time, before the residue was washed with methanol three times, following the same procedure. Since the particles had not completely sedimented after the last centrifuging, the solution with the residue was transferred to a small beaker and kept still for a while. Some supernatant solution was then removed by using a pipette. The beaker was placed in the fume hood so that the methanol could evaporate, and the particles dried.

The whole procedure was repeated for S2-S7, but when the samples were added to the boiling phenol it was performed more carefully to avoid too high gas generation. 3 sheets were added and dissolved, before 3 new sheets were added and so on.

Figure 3.3: The experimental setup for the phenol method.

The powder was studied by XRD using D8 focus X-ray diffractometer. In order to find the optimal range for 2θ, the expected phases were simulated in the software TOPAS, see Appendix 2. Each sample was scanned in the range 2θ = 10-66° with a step size of 0.0128496°. The counting rate was set to 6 sec/step. A slit of 1 mm was used, and a fluorescence script was applied (recommended when measuring Fe-containing samples). For each sample, a quantitative analysis by the Rietveld refinement method was carried out. This was performed in the software TOPAS. The iron bearing particles extracted from the sample close to the surface (S1) and the sample 134.7 mm in distance to surface (S7) were studied in SEM.

4 Results

4.1 Grain Size

Figure 4.1-Figure 4.2 and Figure 4.3-Figure 4.4 illustrates the difference in grain size between the samples close to surface and 12.0 cm towards the center of the ingot for the bottom and top slice, respectively. The grain structure at surface is dendritic for the bottom slice, but for the top slice the grain structure is more globular. At 12.0 cm distance to surface the grain structure is globular for both bottom and top slice. Figure 4.5 gives the grain size of sample T1-T9 and B1-B9. Generally, the grain size increases with distance to the surface of the ingot. From ingot surface to the location with 13.6 cm distance from ingot surface, the grain size increases with 36% and 30% for the top-series and bottom-series, respectively. The grain size was approximately 100-120 μm for sample 1-4, 120-130 μm for sample 5-7 and 150-160 μm for sample 8-9.
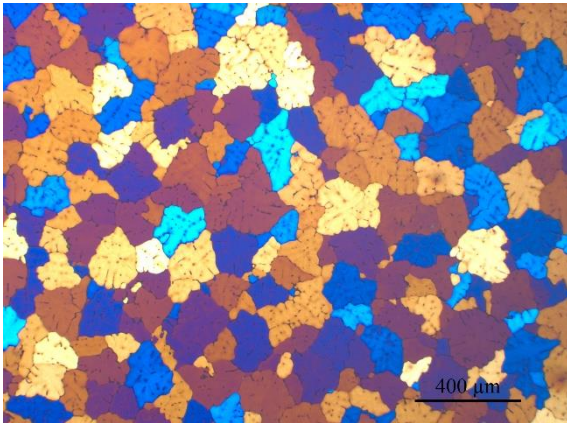
Figure 4.1: Grain structure of the sample closest to the surface from the bottom of the sheet ingot (B1, 50x).
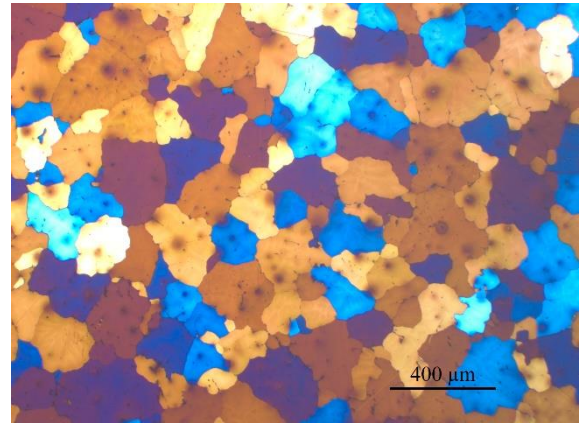
Figure 4.2: Grain structure of the sample with 12.0 cm in distance to surface from the bottom of the sheet ingot (B8, 50x).
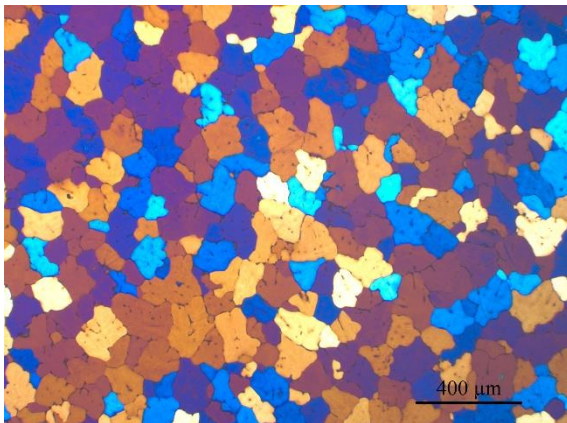
Figure 4.3: Grain structure of the sample closest to the surface from the top of the sheet ingot (T1, 50x).
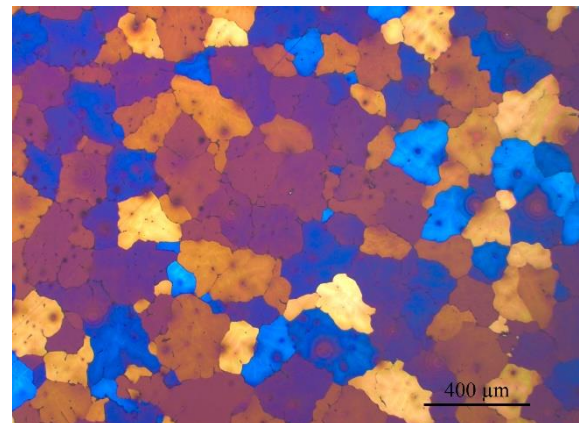
Figure 4.4: Grain structure of the sample with 12.0 cm in distance to surface from the top of the sheet ingot (T8, 50x).
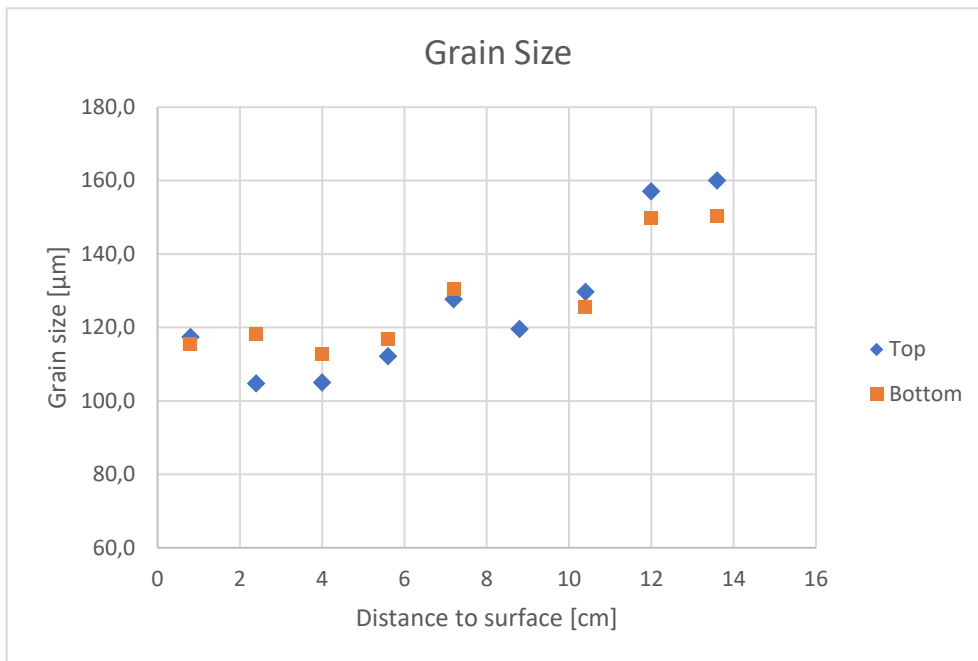
Figure 4.5: The grain size of the different samples as a function of distance to the surface of the ingot.

4.2 The Morphology of Intermetallic Particles

All samples were studied in LM at 200x, 500x and 1000x magnification. Different morphologies were clearly observed along the grain boundaries. Two different *characteristic* morphologies were observed: skeletal and needle-like morphology. Figure 4.6 shows examples of skeletal morphology found in sample T5 and B8, respectively. This type of morphology is also often called Chinese script. Examples of needle-like morphology can be seen in Figure 4.7. The needles with sharp and sometimes jagged edges are not evenly distributed, but they seem to somehow be connected to each other. From the surface and to the center of the ingot, a change in the particle's morphology can be seen. In sample B1-B4 (distance to surface: 0.8-5.6 cm) the dominating morphology seems to be the skeletal one. However, some needle-like particles can be seen in sample B4 as well. More needle-like particles can be observed as the distance to surface increases. In the samples closest to the center of the ingot, the needle-like morphology dominates. However, particles with skeletal morphology can still be observed. The same applies for the series from the top of the sheet ingot (T1-T9). The change in the particle's morphologies can be further studied in Appendix 3 and Appendix 4.

(a)   (b)
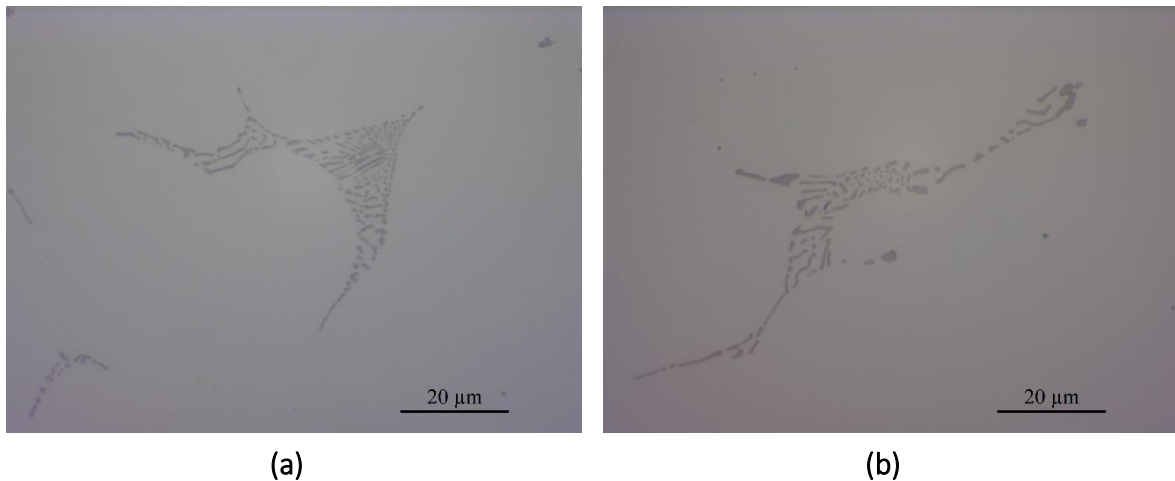
Figure 4.6: Particle with skeletal morphology a) T5, 1000x b) B8, 1000x

(a)   (b)
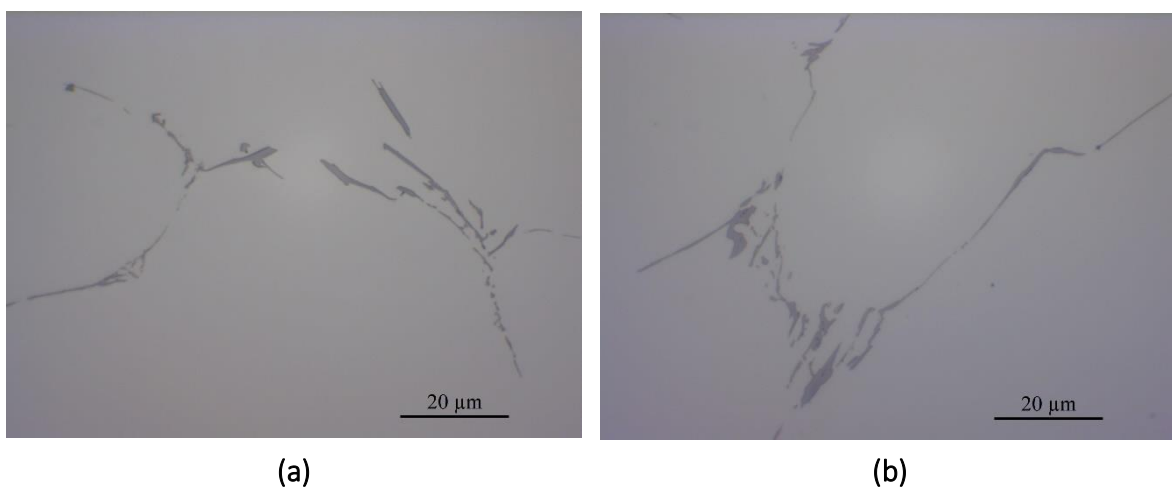
Figure 4.7: Particle with needle-like morphology a) B9, 1000x b) T8, 1000x

43

4.3   EBSD

EBSD was performed on particles with characteristic morphologies in sample T3, T5 and T8. Table 4.1 shows examples of typical morphologies indexed as either Al_mFe, Al_6Fe or Al_3Fe. All lines point towards branches of a particle where an EBSP was acquired and successfully indexed. The table shows that particles with different versions of skeletal morphology, were indexed as Al_mFe. Bundles of particles with needle-like morphology, were indexed as Al_3Fe, see Example 1 and Example 2 in the row for Al_3Fe. Particles with plate-like morphology with jagged edges, were also indexed as Al_3Fe, see Example 3. Few particles could be identified as Al_6Fe by EBSD. Table 4.1 shows that the few particles indexed as Al_6Fe appeared among or adjacent to particles with needle-like morphology. The morphology of Al_6Fe phase was plate-like. More examples of particles identified by EBSD are shown in Appendix 5. The three next sub sections show one example of EBSP acquired from Al_mFe, Al_3Fe and Al_6Fe with the solution.

Table 4.1: Examples of characteristic morphologies of particles identified as Al_mFe, Al_3Fe and Al_6Fe by EBSD.

4.3.1 Al$_m$Fe

Figure 4.8 (a) shows a particle with typical skeletal morphology. Table 4.1 showed that several of the branches of this particle were identified as Al$_m$Fe by EBSD. The EBSP achieved from the highlighted branch in Figure 4.8 (a) is shown in Figure 4.8 (b). The EBSP with overlaid solution can be seen in Figure 4.8 (c). It can be seen that the EBSP and the simulated solution for the Al$_m$Fe phase has the best fit, see Table 4.2. With a fit of 0.97°, the phase can be identified as Al$_m$Fe. In addition, the CI value is high (0.500), which means that the EBSP indexing is reliable.
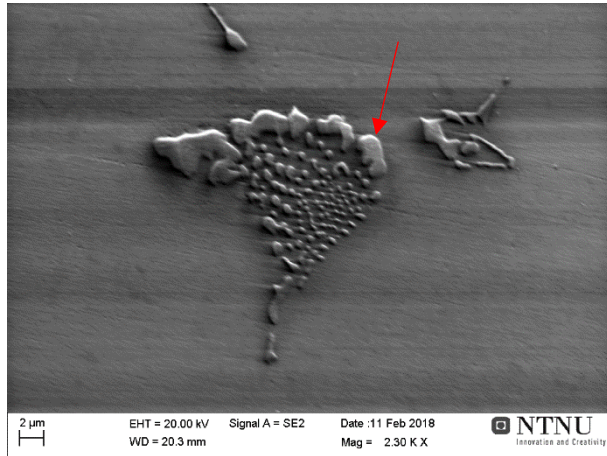
Table 4.2: Parameters achieved from the software

Phase	Votes	Fit [°]	CI	Rank Factor
Al$_m$Fe	115	0.97	0.500	1.00
Al$_3$Fe	63	1.71	0.114	0.55
Al$_6$Fe	28	2.16	0.005	0.24
Aluminium	5	2.60	0.005	0.04

(a)
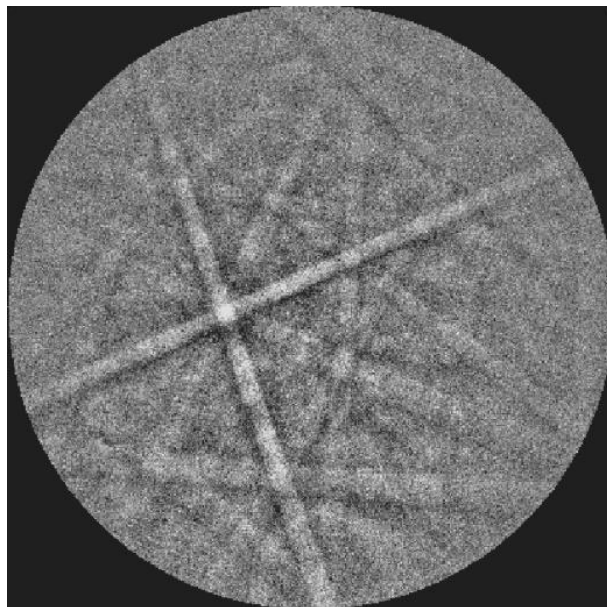
(b)
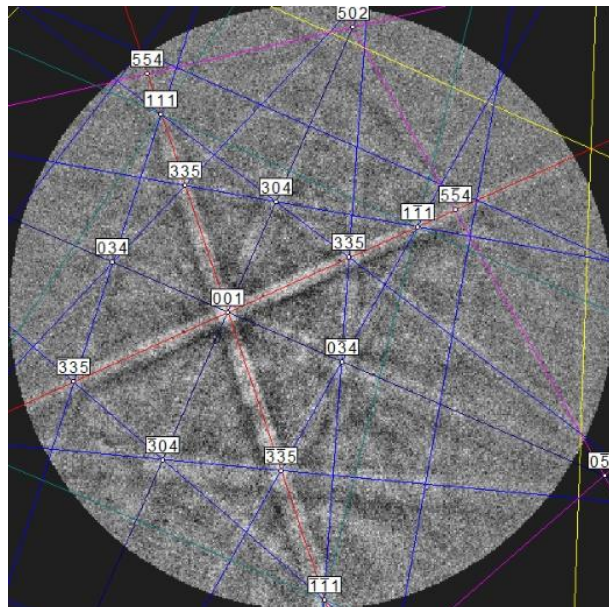
(c)

Figure 4.8: a) Particle with skeletal morphology, b) Electron backscatter pattern (EBSP) from the highlighted particle, c) The EBSP with solution overlaid, indexed as Al$_m$Fe.

4.3.2 Al₃Fe

Figure 4.9 (a) shows a SEM image of two particles with jagged plate-like morphology, which were both identified as Al$_3$Fe by EBSD. The corresponding EBSP from the highlighted particle, can be seen in Figure 4.9 (b). It can be seen by the naked eye that the overlaid solution in Figure 4.9 (c) is a very good fit. The fit value achieved from the software confirmed this, see Table 4.3. In addition, the CI-value is very high (0.950). This means that the Al$_3$Fe particle can be identified with high certainty.

Table 4.3: Parameters achieved from the software

Phase	Votes	Fit [°]	CI	Rank Factor
Al$_3$Fe	50	0.40	0.950	1.00
Aluminum	15	1.83	0.050	0.34
Al$_6$Fe	11	2.13	0.014	0.13
Al$_m$Fe	7	1.88	0.005	0.04
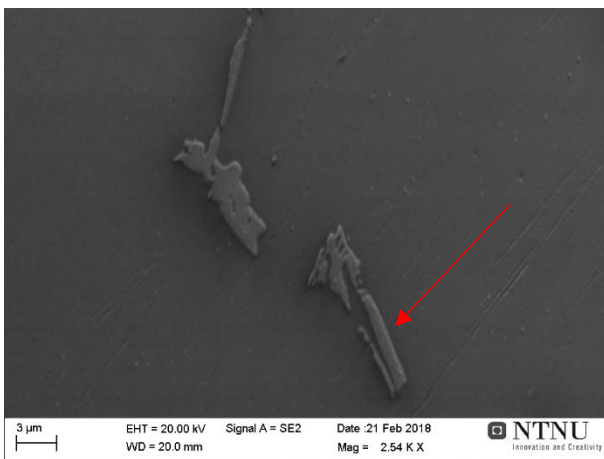
(a)
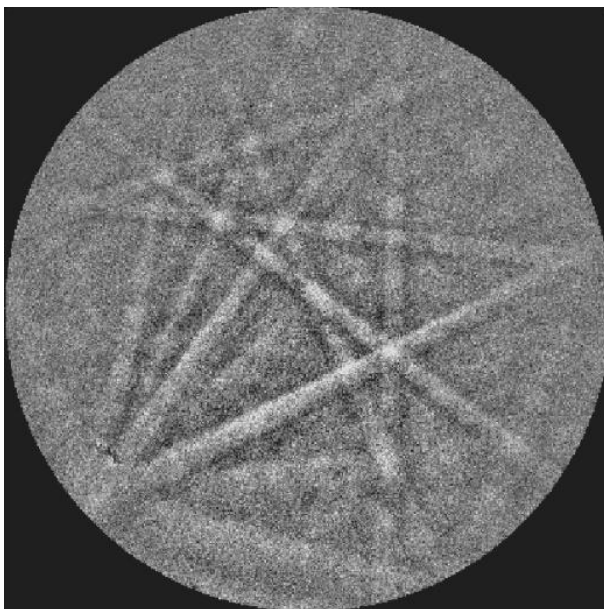
(b)
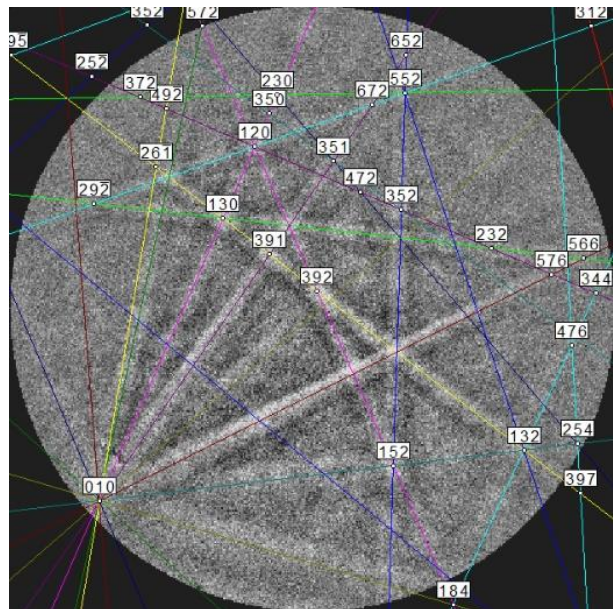
(c)

Figure 4.9: a) Particles with jagged plate-like morphology, b) EBSP from the highlighted particle, c) The EBSP with solution overlaid, indexed as Al$_3$Fe.

46

4.3.3   Al$_6$Fe

Close to some particles with needle-like morphology, there was found a particle with plate-like morphology, see Figure 4.10 (a). Figure 4.10 (b) shows that a clear and defined EBSP was achieved from this particle. The simulated pattern for Al$_6$Fe has a clearly better fit compared to the other phases, see Table 4.4. With a CI-value of 0.427, it is reliable that the EBSP is correctly indexed. The overlaid solution can be seen in Figure 4.10 (c).

Table 4.4: Parameters achieved from the software

Phase	Votes	Fit [°]	CI	Rank Factor
Al$_6$Fe	120	0.87	0.427	1.00
Al$_3$Fe	10	2.19	0.014	0.08
Al$_6$Fe	7	2.37	0.014	0.06
Aluminium	6	2.14	0.009	0.05
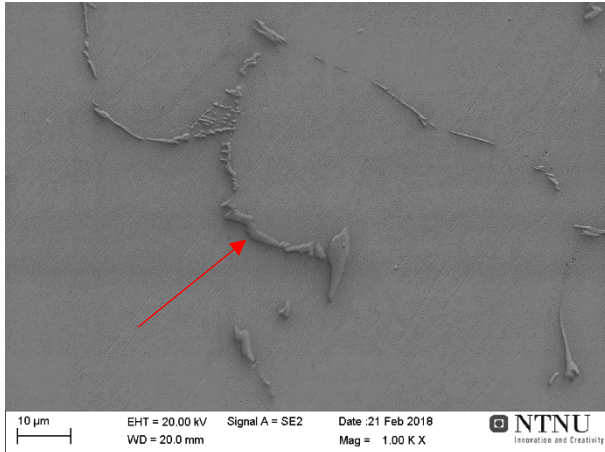
(a)
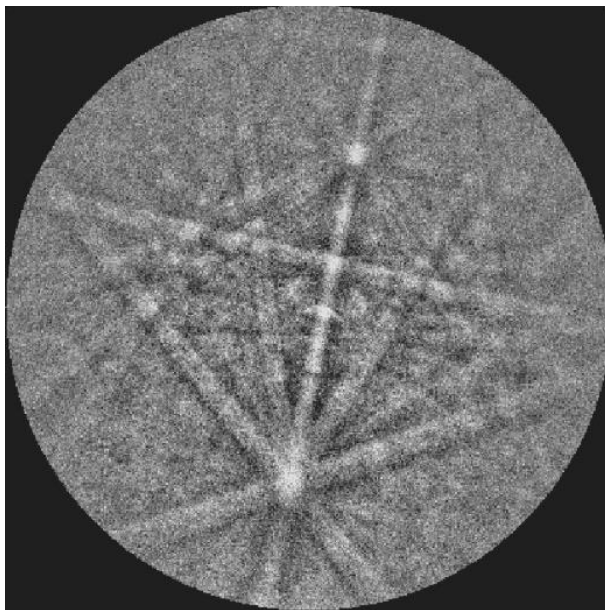
(b)
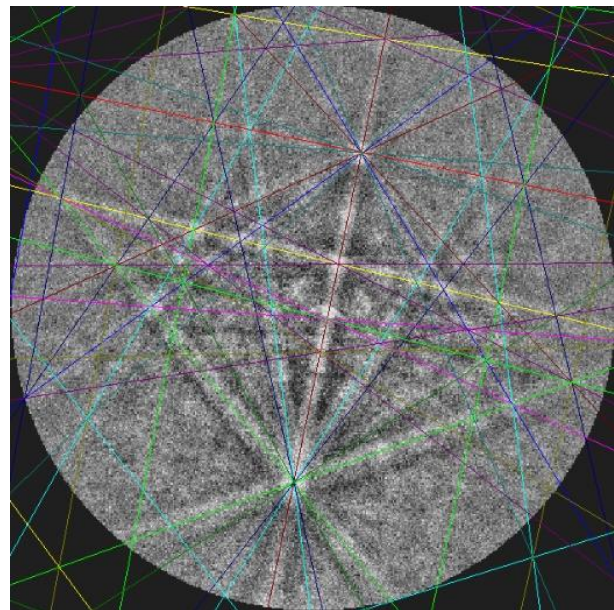
(c)

Figure 4.10: a) Particle with plate-like morphology, close to particles with needle-like morphology, b) EBSP from the highlighted particle, c) The EBSP with solution overlaid, indexed as Al$_6$Fe.

4.4 WDS

Approximately 40 WDS analyses were performed on particles with characteristic morphologies in sample T1, T3, T5, T7 and T9. Figure 4.11 shows the atomic percent of iron (at% Fe) in the particles. When analyzed for all elements (here: Al, Fe, Mg, Si, Mn and Ti), the total weight percent in one analysis should add up to approximately 100%. Analyses which gave a total weight percent below 98% or above 103% are excluded in Figure 4.11. Analyses which are not within these limits, indicates that not only the particle has been analyzed, but that the aluminum matrix is also within the interaction volume. From the figure three different ranges of at% Fe in the iron bearing particles can be set:

  i)   14.3-15.5 at% Fe indicating Al_6Fe phase
  ii)   18.9-21.3 at% Fe indicating Al_mFe phase
  iii)   21.8-24.0 at% Fe indicating Al_3Fe phase

The ranges for the different phases will be discussed later. For simplicity, is the at% Fe in the expected phases shown in Table 4.5. Figure 4.12 shows that Al_mFe are present across the entire thickness of the ingot. For the samples close to the surface and 4.0 cm towards the center of the ingot, all analyses indicate that only Al_mFe phase exists. There are only a few analyses indicating the constitution of phase Al_6Fe, which are found 7.2 and 10.4 cm in distance to surface. At 7.2 cm towards the center of the ingot, four analyses indicate the phase Al_3Fe. Further towards the center of the ingot, the number of Al_3Fe increases, while the number of analyses indicating Al_mFe constitutions decreases. The next subsections will show examples of typical morphologies for the three different ranges of at% Fe for each sample analyzed.

Table 4.5: at% Fe of the different iron bearing particles

Particle	at% Fe
Al_mFe (m= 4.0-4.4)	20.0-18.5
Al_3Fe ($Al_{13}Fe_4$)	23.5
Al_6Fe	14.3

Figure 4.13 shows how the at% Si varies for the different phases. The content of Si varies from zero up to 1.8 at% for the Al_mFe phase. While the content of Si for the Al_3Fe phase never exceeds 0.5 at%. Al_6Fe phase contains approximately no Si. Figure 4.14 shows how the at% Mg varies for the different phases. It shows the same trend as the content of Si. While the Al_mFe phase can have up to 1.9 at% Mg, the figure shows that the Al_6Fe phase never exceeds 0.2 at% Mg. Al_3Fe has also a low content of Mg, with a maximum of 0.6 at%. The amount of Mn in all samples were low (<0.3 at% Mn). No analyses indicated the presence of Ti.
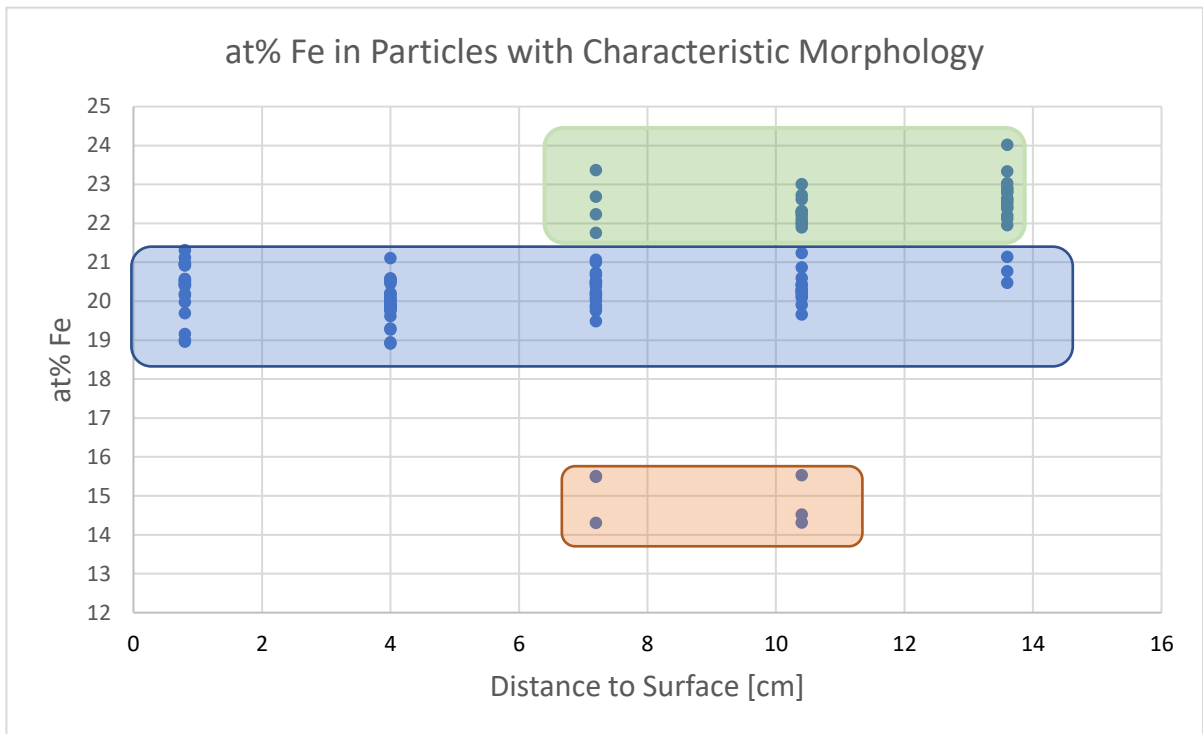
Figure 4.11: Atomic percent of iron in particles with characteristic morphology, green: Al₃Fe, blue: AlₘFe, red: Al₆Fe.
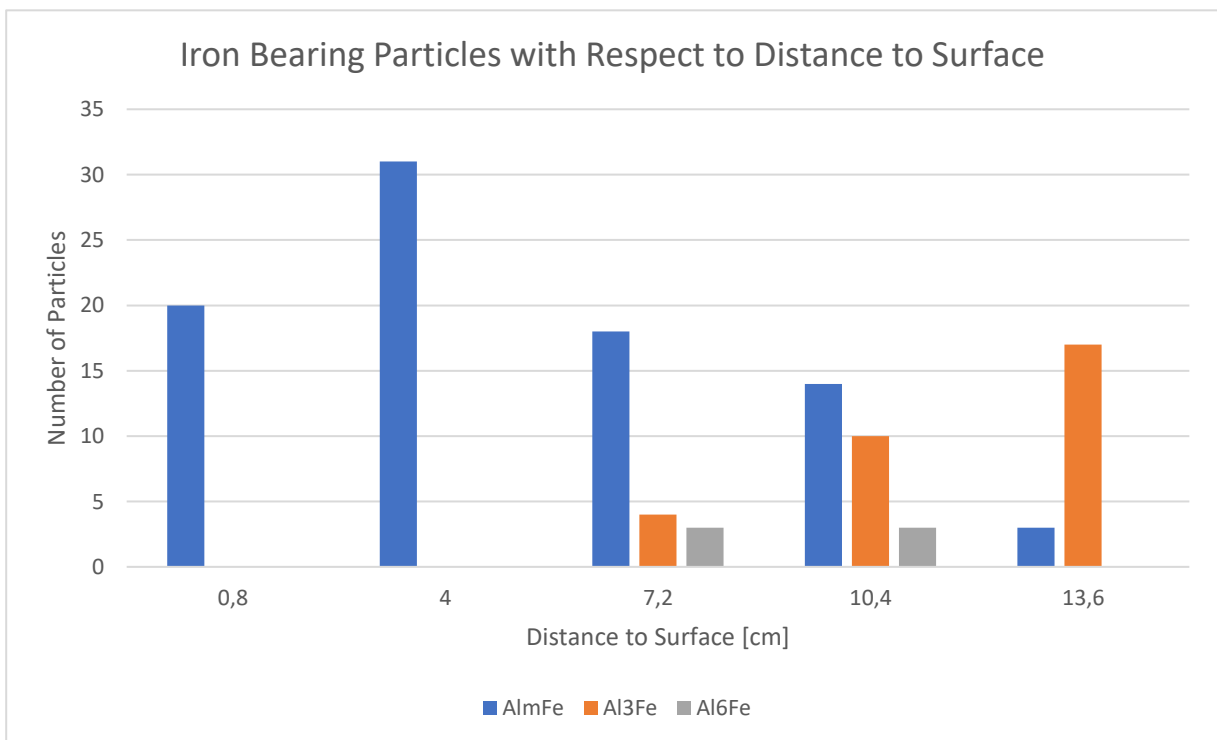
Figure 4.12: Distribution of analyses indicating AlₘFe, Al₃Fe and Al₆Fe with respect to the surface of the ingot.
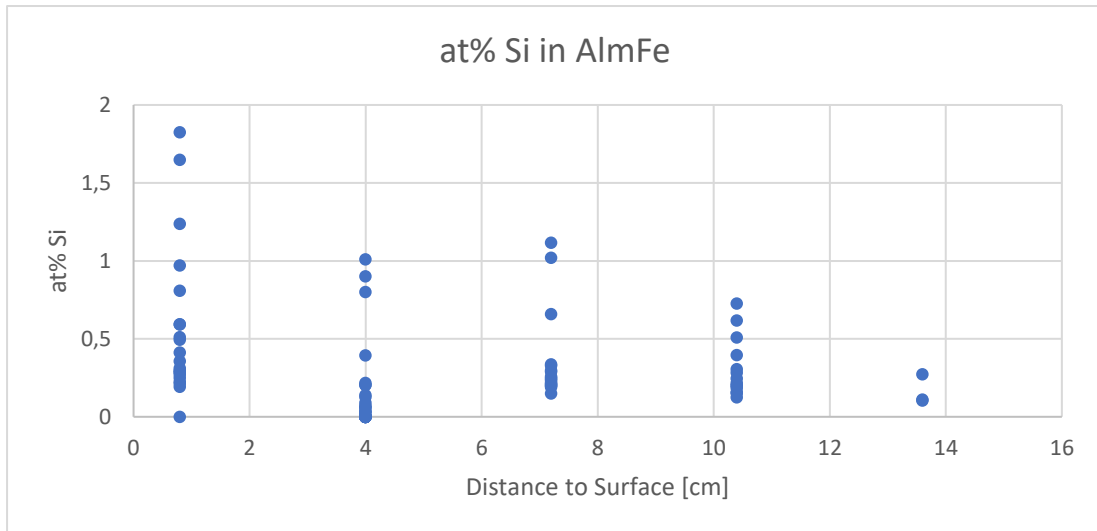
(a)
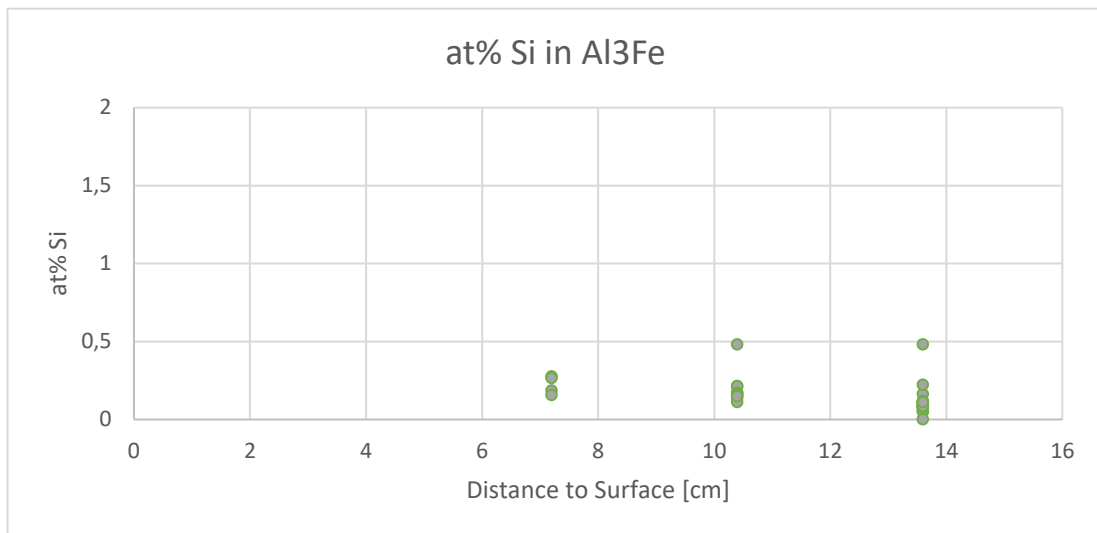
(b)
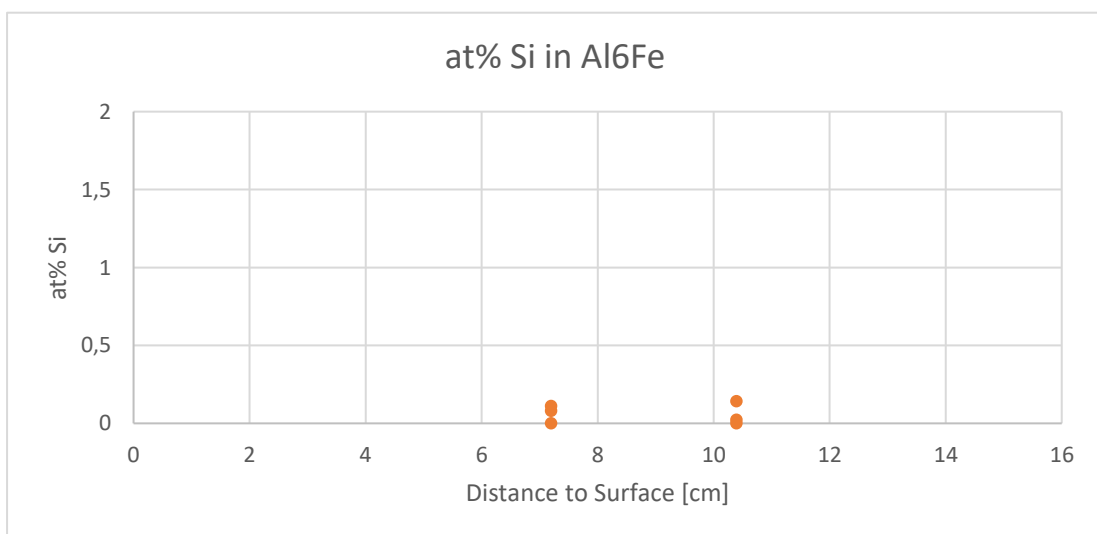
(c)

Figure 4.13: at% Si in the three different phases a) Al$_m$Fe, b) Al$_3$Fe, c) Al$_6$Fe
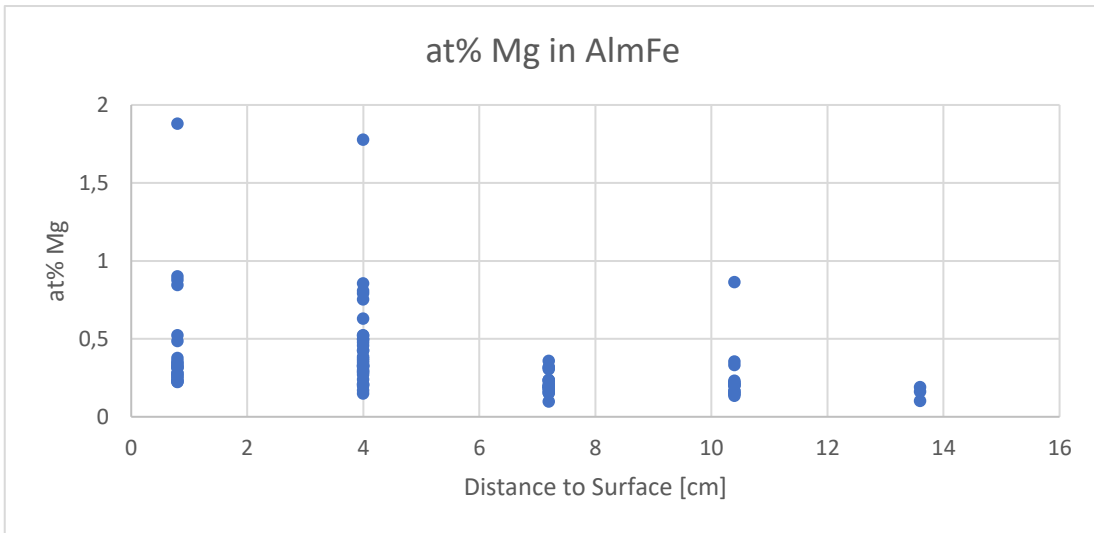
(a)
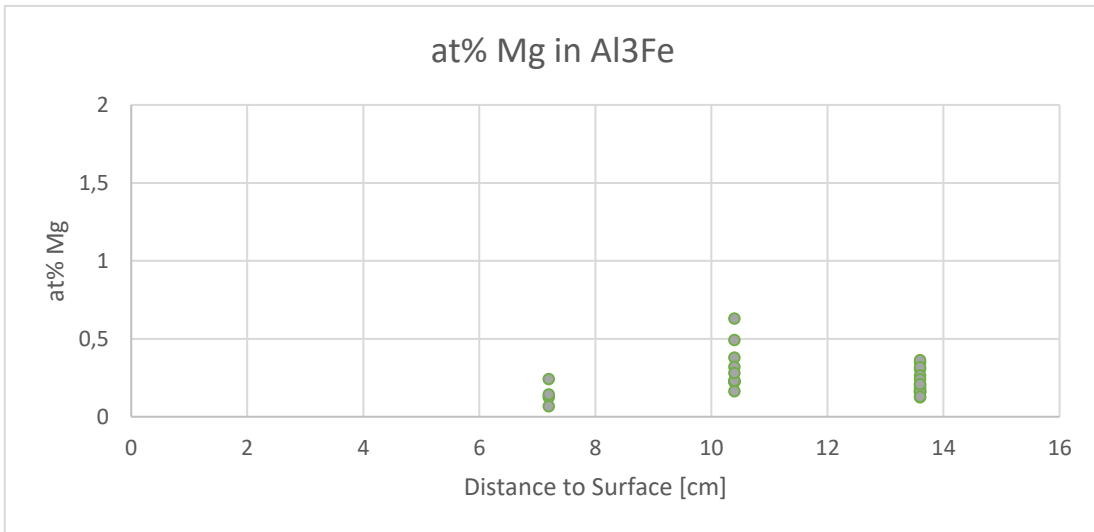
(b)
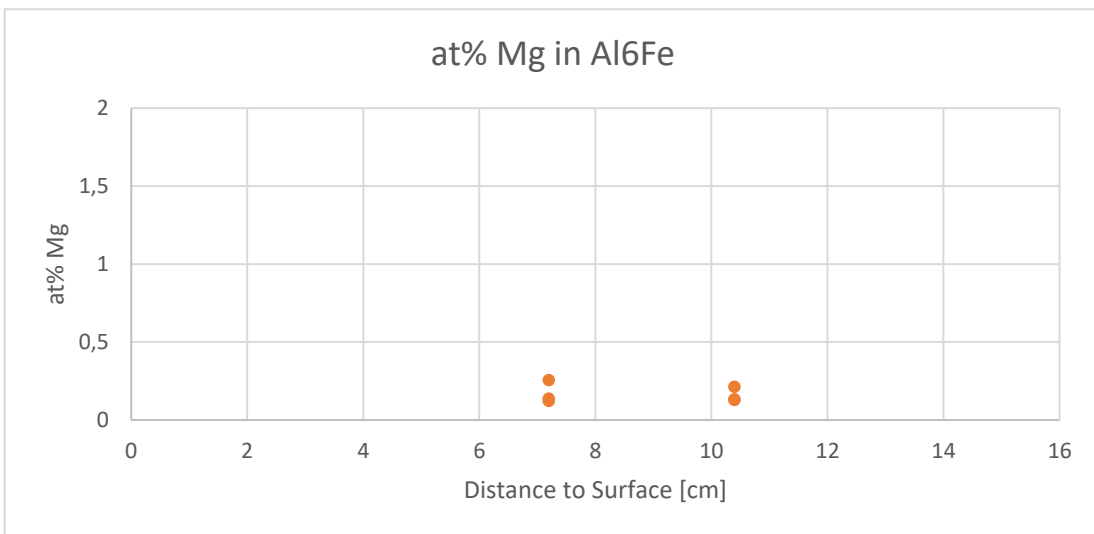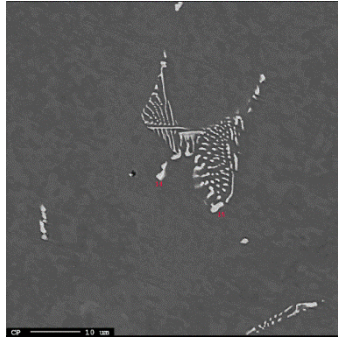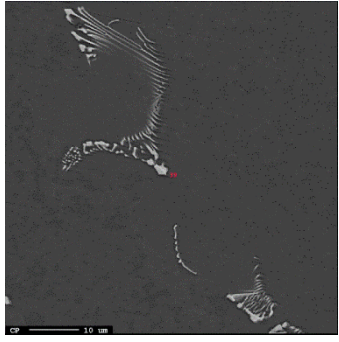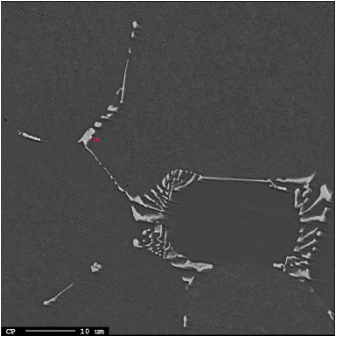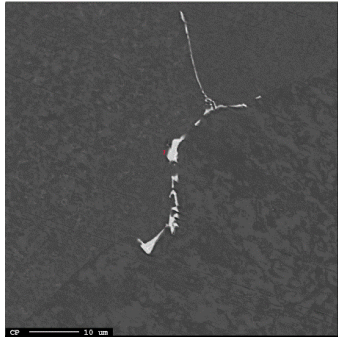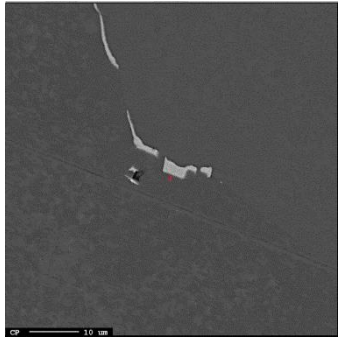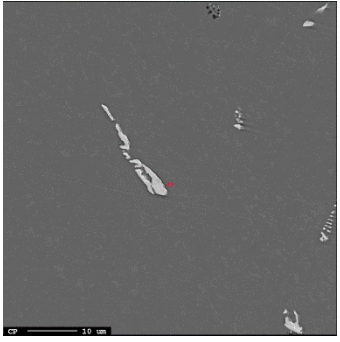
(c)

Figure 4.14: at% Mg in the three different phases a) Al_mFe, b) Al_3Fe, c) Al_6Fe

4.4.1 Sample T1

Only 20 of 40 WDS analyses were reliable for quantitative analysis (as explained in Section 4.4) for sample T1. All the reliable analyses indicated the constitution of Al_mFe phase. The characteristic morphology for Al_mFe is skeletal, as shown in Table 4.6a). Notice that even if the extent of the particle can be 30 µm, most of the branches of the particle is less than 1 µm thick. The orientation of the particle in the aluminium matrix will affect the apparent morphology in the surface of a plane polished sample. This is illustrated in Table 4.6b), which also shows particles with at% Fe within the set range for the Al_mFe phase for this WDS experiment. These particles have a more plate-like morphology, with uneven edges and curved formation.
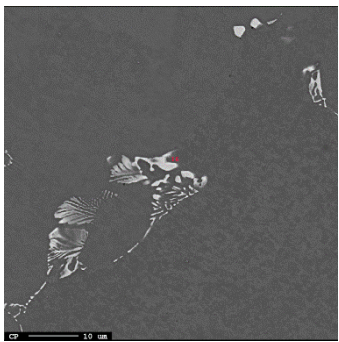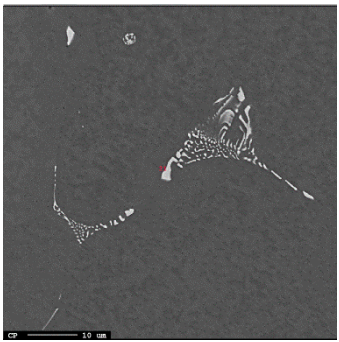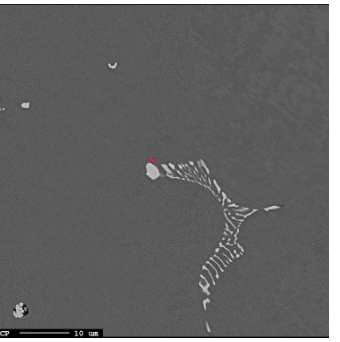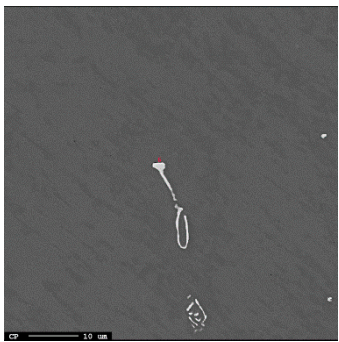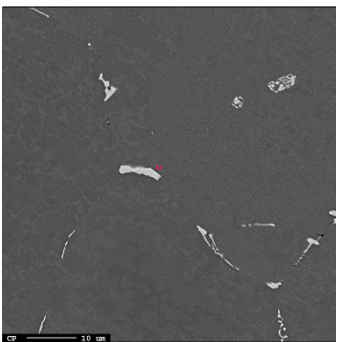
Table 4.6: Example of morphology for the AlmFe phase in sample T1. The scale bar is 10 µm and the red dot gives the branch of the particle where the analysis was taken.

	Example 1	Example 2	Example 3
(a) Characteristic morphology: Skeletal			
(b) Not characteristic morphology			

4.4.2 Sample T3

42 WDS analyses were performed on particles in sample T3 and 32 of these were successful. Sample T3 corresponds to approximately 4.0 cm in distance to surface of the ingot. All 32 analyses indicate the chemical composition of Al_mFe phase. The same apply for T3 as for T1: Al_mFe has a complex structure and its orientation in the aluminium matrix will affect the morphology displayed in the sample surface. This results in various morphologies for the phase, which is illustrated in Table 4.7. Example 1 of the characteristic morphologies shows a morphology which can be described as feathery. While in Example 2, there is less of the plate-like areas which gives the feathery appearance, instead numerous thin, circular branches seem to appear in the surface. Examples 3 shows a particle with curved formation, consisting of several thin branches. In this report, all of these three morphologies are within the term skeletal morphology. Later in this report, *skeletal morphology* will be used to refer to this characteristic morphology.
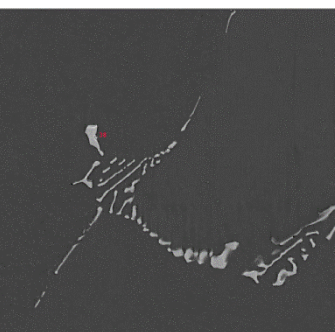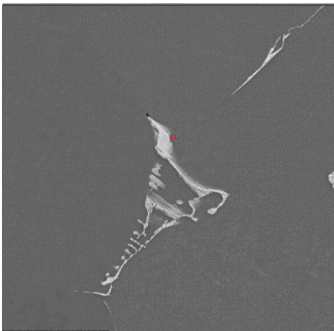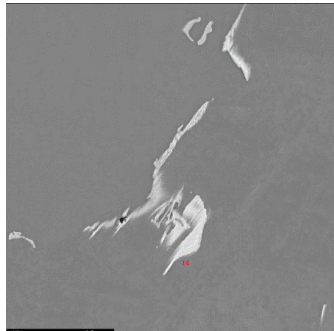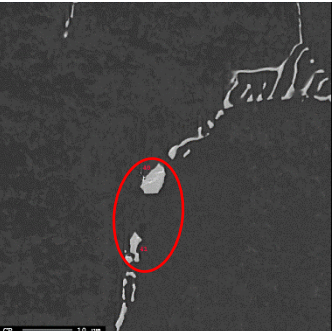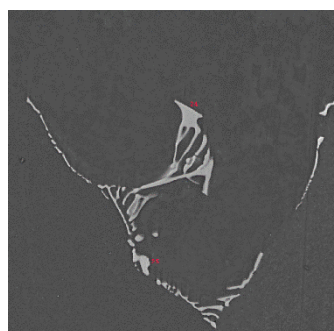
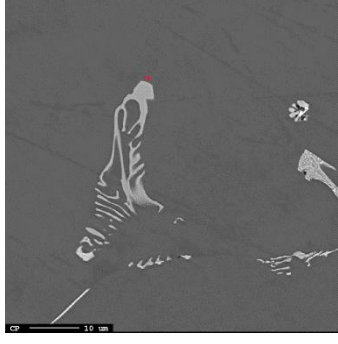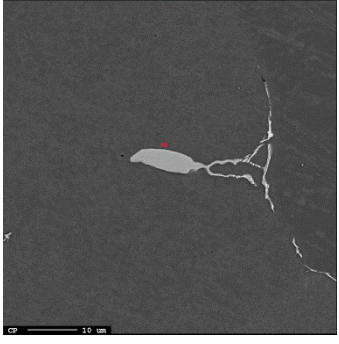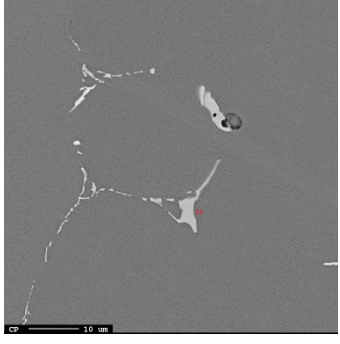*Table 4.7: Example of morphology for the AlmFe phase in sample T3. The scale bar is 10 μm and the red dot gives the branch of the particle where the analysis was taken.*

	Example 1	Example 2	Example 3
Characteristic morphology: Skeletal			
Not characteristic morphology			

4.4.3 Sample T5

In sample T5, 41 WDS analyses were performed, with 25 successful analyses. T5 corresponds to 7.2 cm in distance to surface of the ingot. In addition to the dominating phase Al_mFe, the two phases Al_3Fe and Al_6Fe were also identified, see Table 4.8. Al_mFe has skeletal morphology, as described previously. Al_3Fe was identified as particles with stacked plate morphology, see Example 1 and Example 2. The phase also appeared with a denser plate-like morphology and found adjacent to typical Al_mFe morphology, see Example 3. The morphology of two of the particles identified as Al_6Fe were skeletal-like and very similar to the typical morphology of Al_mFe, see Example 1 and Example 2. However, by studying these particles in detail, the two Al_6Fe particles seem to give a different impression than the typical morphology of Al_mFe. Example 3 of Al_6Fe shows a plate-like morphology adjacent to particles with needle-like morphology. The needle-like particles are brighter than the particle identified as Al_6Fe. In BSE-imaging, this is called Z-contrast and indicates that the brighter phase has a higher mean atomic number. In this material, a higher fraction of Fe is expected in the brighter phase.
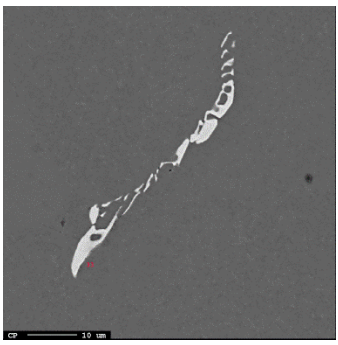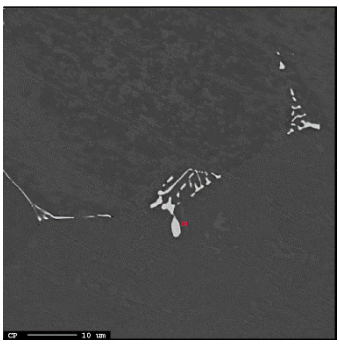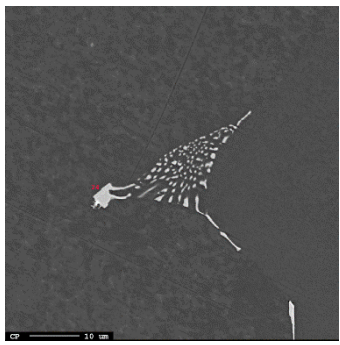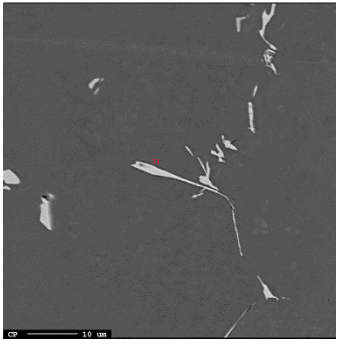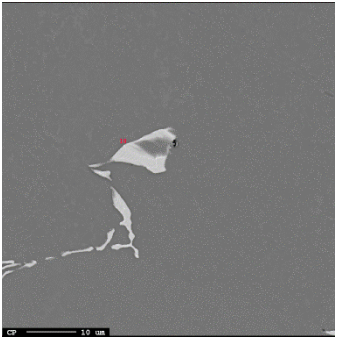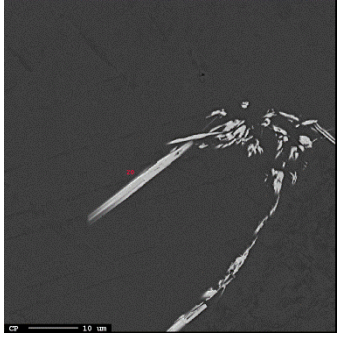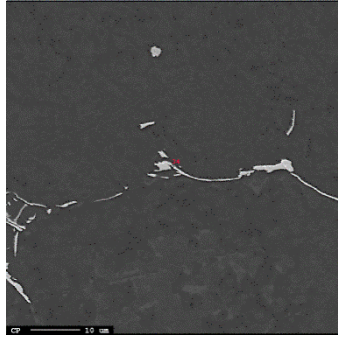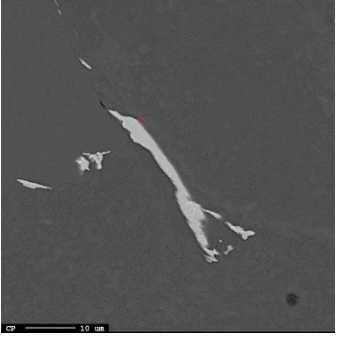
Table 4.8: Example of morphology for the different phases identified in sample T5. The scale bar is 10 μm and the red dot gives the branch of the particle where the analysis was taken.

	Example 1	Example 2	Example 3
Al_mFe			
Al_3Fe			
Al_6Fe			

4.4.4 Sample T7

40 WDS analyses were performed in sample T7, with 27 successful analyses. T7 corresponds to approximately 10.4 cm in distance to surface of the ingot. At this distance, the fraction of analyses indicating the Al_3Fe phase increased. The phase can appear with different morphology; needle-like, plate-like and a stacked plate, as shown in Example 1, Example 2 and Example 3 in Table 4.9, respectively. Al_mFe is also present at this distance from surface, with the same characteristic skeletal morphology as described earlier. Al_6Fe was identified at one particle with skeletal-like morphology and at two particles with plate-like morphology. The two particles with plate-like morphology were found close to particles with needle-like morphology. Also in these three examples, Z-contrast can be observed between the Al_6Fe phase and a couple of the surrounding needle-like particles.
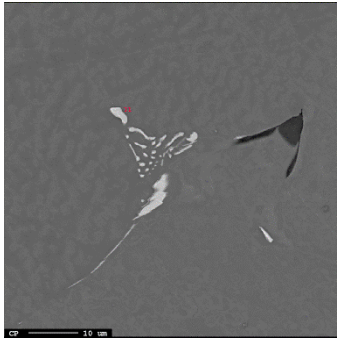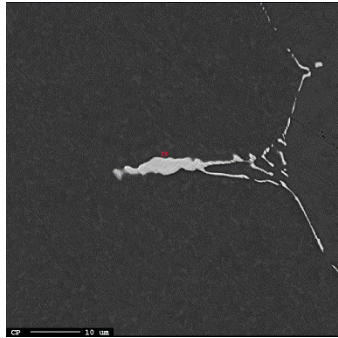
Table 4.9: Example of morphology for the different phases identified in sample T7. The scale bar is 10 μm and the red dot gives the branch of the particle where the analysis was taken.

4.4.5 Sample T9

38 WDS analyses were performed in sample T7, with 20 successful analyses. Sample T9 corresponds to the sample with the longest distance to surface. The dominating phase was Al_3Fe. The phase appeared with both plate-like morphology, needle-like and stacked plate morphology as shown in Table 4.10. Three analyses indicated the phase Al_mFe. Al_mFe is present with a simpler form of skeletal morphology, as not so many branches can be seen. No analyses indicated the existence of Al_6Fe phase.

Table 4.10: Example of morphology for the different phases identified in sample T9. The scale bar is 10 μm and the red dot gives the branch of the particle where the analysis was taken.

	Example 1	Example 2	Example 3
Al_mFe			
Al_3Fe			

4.5   Deep Etching

Three samples (T1, T7 and T9) were deep etched to study 3D-morphology of different phases. In the sample close to the surface (T1), particles with skeletal morphology dominated. At 10.4 cm (T7) and 13.6 cm in distance to surface (T9), the dominating morphology were bundles of needles, flakes and rods or stacked plates. The small sizes of the particles should be emphasized. The branches of the skeletal particles were often less than 1 µm. The thickness of plate- and flake-like areas were usually in the scale of nanometers. The next subsections will show and describe the different kind of morphologies found in the three samples.

4.5.1   Sample T1

In the deep etched sample T1, only particles with dendritic morphology were observed. Figure 4.15 shows an area with several particles with this morphology. In Figure 4.16 it can be seen that the dendrite-like eutectic particles tend to have semi-spherical tips. This is a typical morphology of the Al_mFe phase. This morphology can also be described as skeletal; a defined spine can often be seen in center of a flake-like area. From the flake, there is frequent branching. Figure 4.17 shows what can be a part of the beginning of a new branch of dendritic eutectic phase. The spine is curved and has frequent branching. The branches on the different sides of the spine are at some places touching each other, almost enclosing the curved spine. From Figure 4.18 another skeletal particle can be seen. The spine is not completely enclosed, but new branches with the characteristic semi-spherical tips have grown from the spine in the interdendritic liquid during solidification.
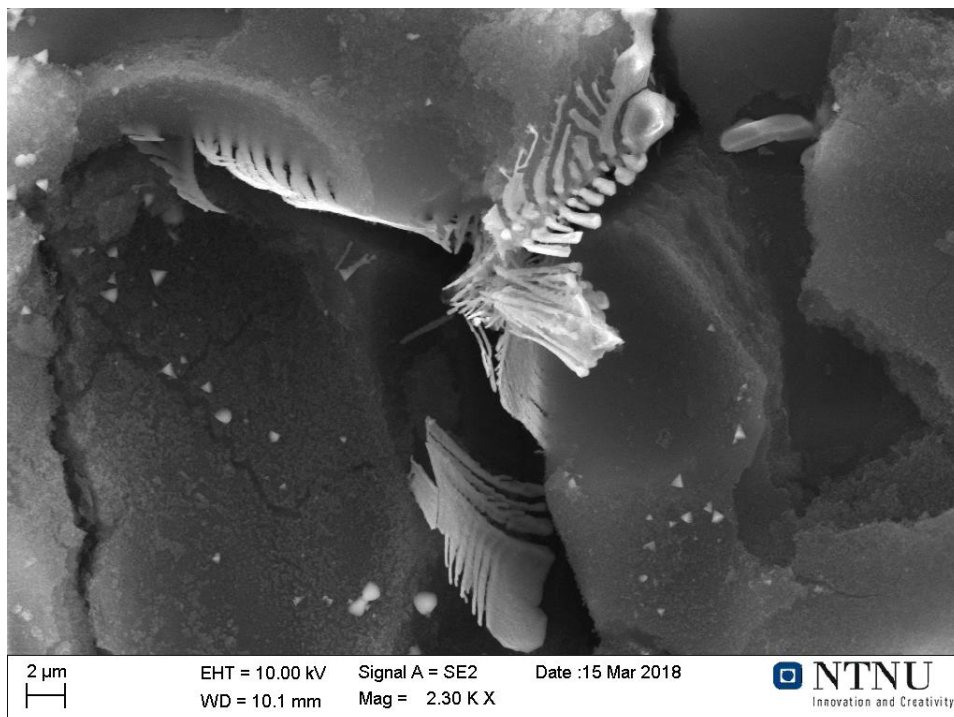

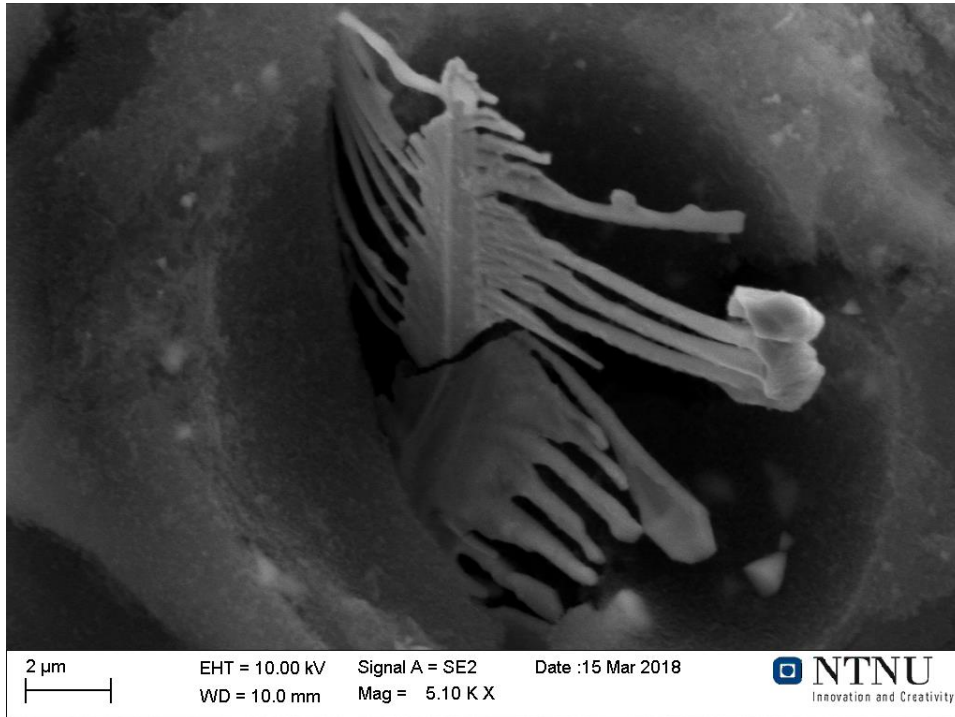*Figure 4.15: Overview of several dendritic eutectic particles.*

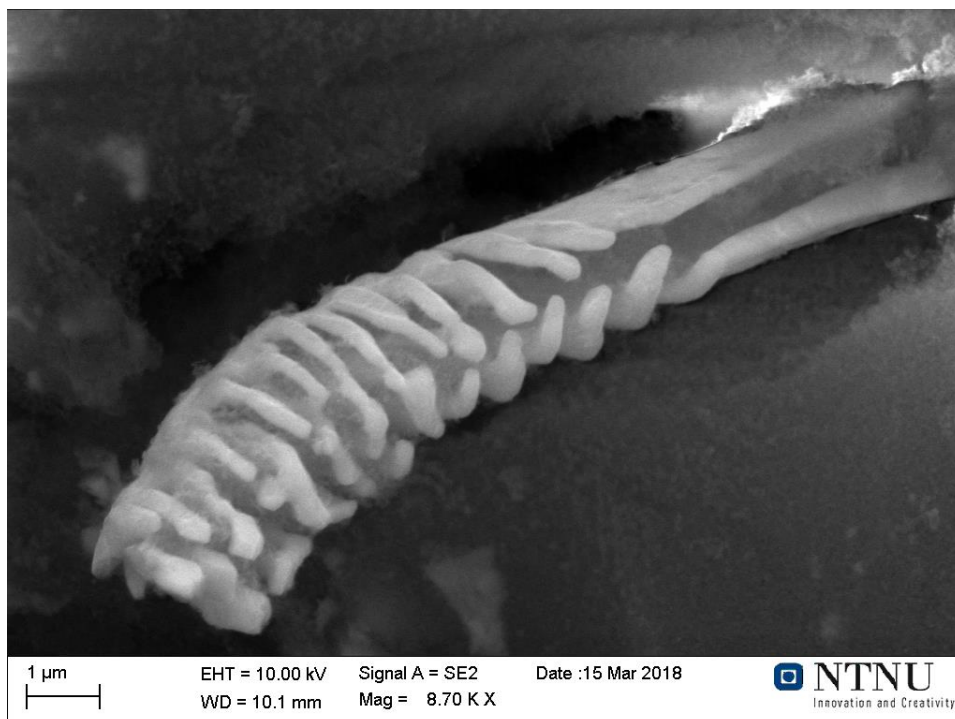*Figure 4.16: Dendritic eutectic particle with semi-spherical tips.*

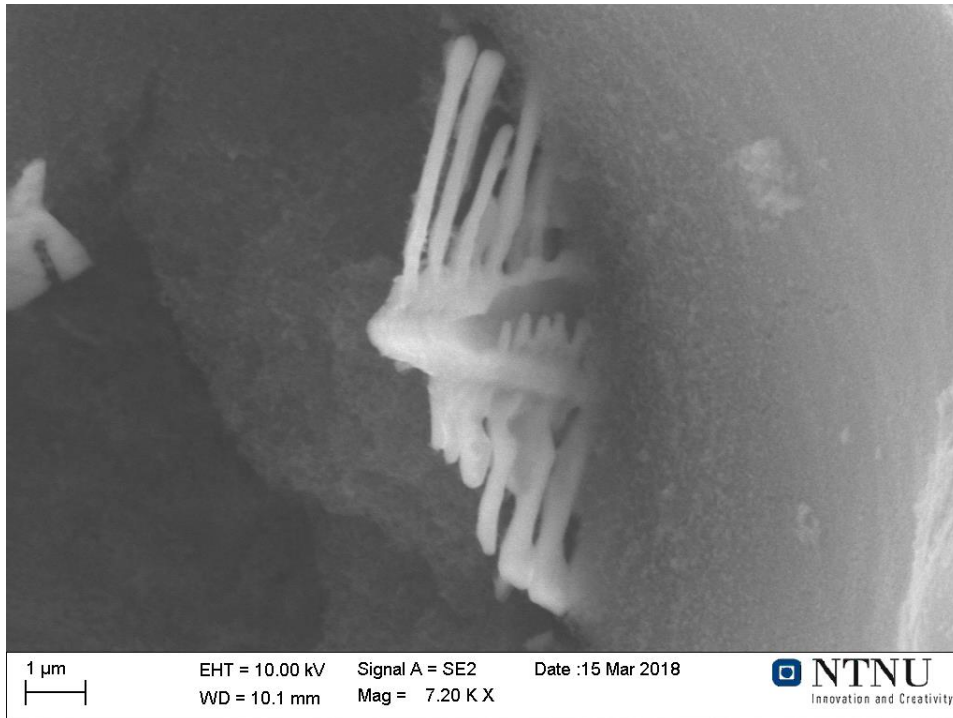*Figure 4.17: Close up of a particle with spine-like morphology.*

Figure 4.18: Particle with skeletal morphology, where a "spine" can be seen in the middle.

4.5.2 Sample T7

In sample T7, particles with different kind of morphology were seen: skeletal/dendritic, needle-like and plate-like. Figure 4.19 shows a particle with skeletal morphology. From the center of the particle, it seems like four main branches radiate in different directions. This indicates an Al_mFe phase. The particle has both branches with semi-spherical tips and branches which have become flake-like. The center of the particle can be a possible nucleation site. Another example of a particle with skeletal morphology can be seen in Figure 4.20. The particle is curved, and the outermost branches seem to have grown into each other. Some of the tips of the branches are semi-spherical, indicating to be an Al_mFe phase.

The typical 3D-morphology of the particles described as needle-like in polished samples is shown in Figure 4.21. The figure shows bundle of needle-, rod- and small flake-like particles growing in different directions. This kind of morphology is typical for Al_3Fe. In Figure 4.22, three particles with stacked plate morphology can be seen adjacent to particles with needle-like morphology. The stacked plate particles appear to consist of densely packed rods which grow in the same direction, probably parallel to heat flow. This morphology indicates an Al_3Fe phase. Figure 4.23 also shows a particle with plate-like morphology. However, here the densely packed rods appear to have branched from one principal branch.
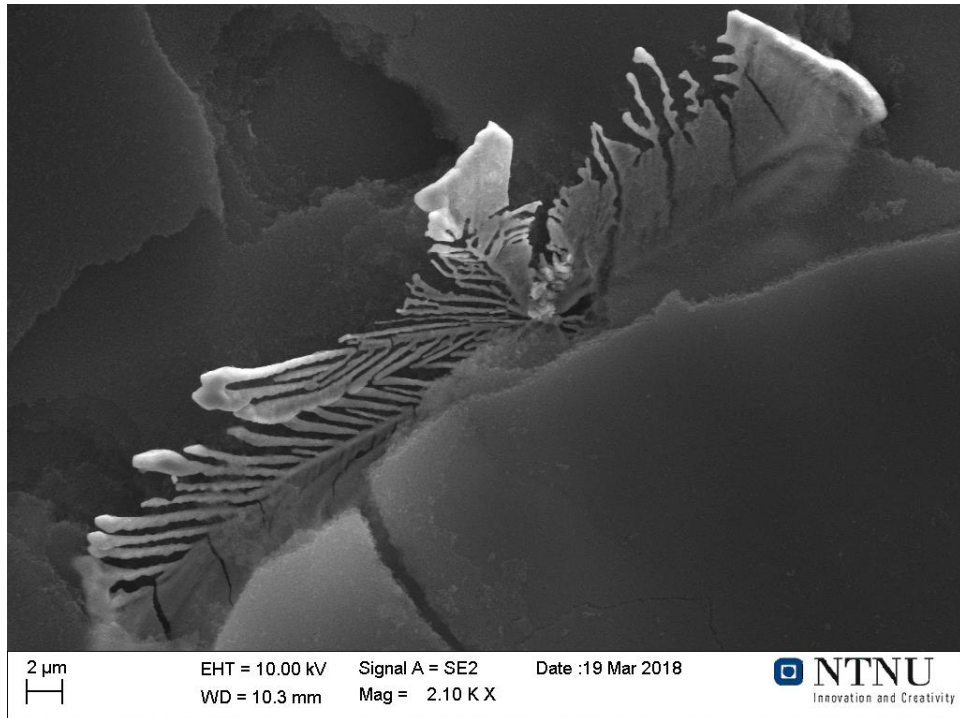
Figure 4.19: Particle with skeletal morphology, the center is a possible nucleation site.
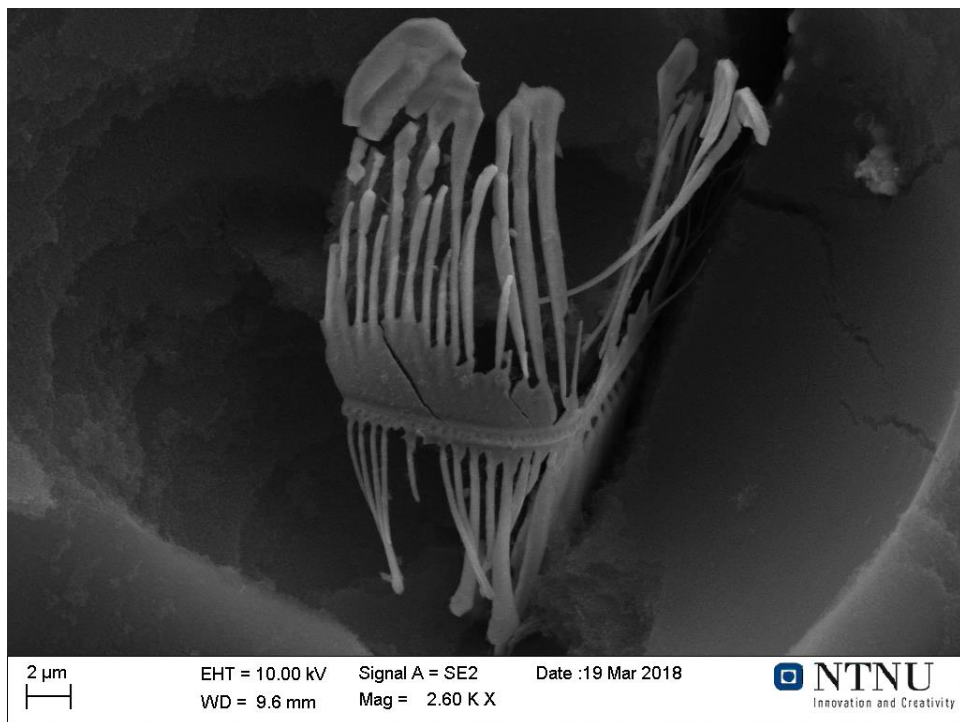

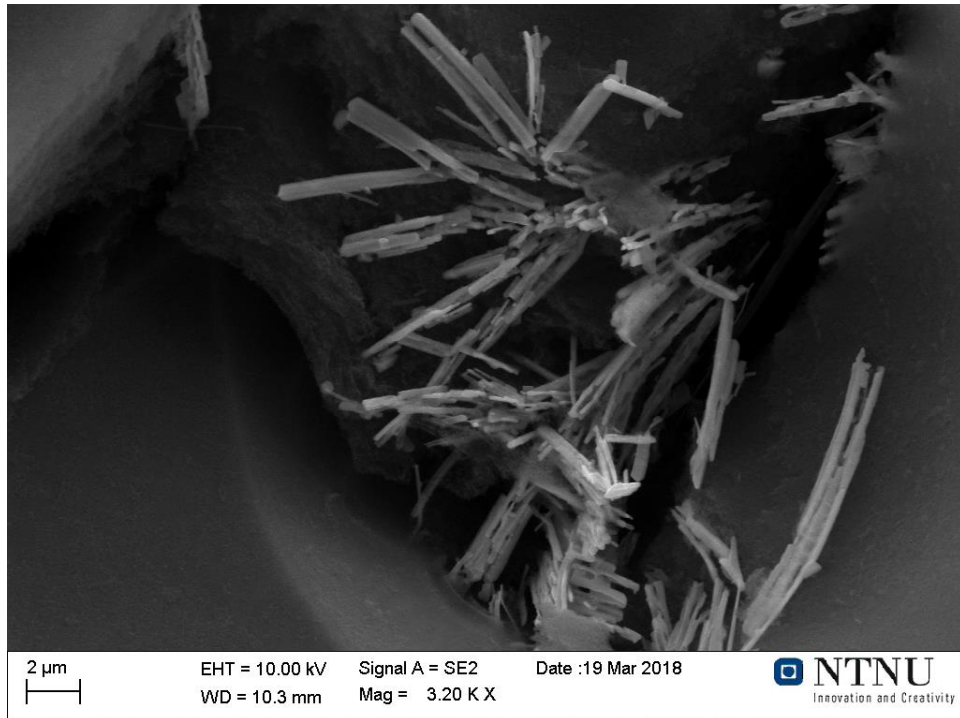*Figure 4.20: Particle with curved skeletal morphology.*

Figure 4.21: Bundle of particles with needle-, flake- and rod-like morphology.
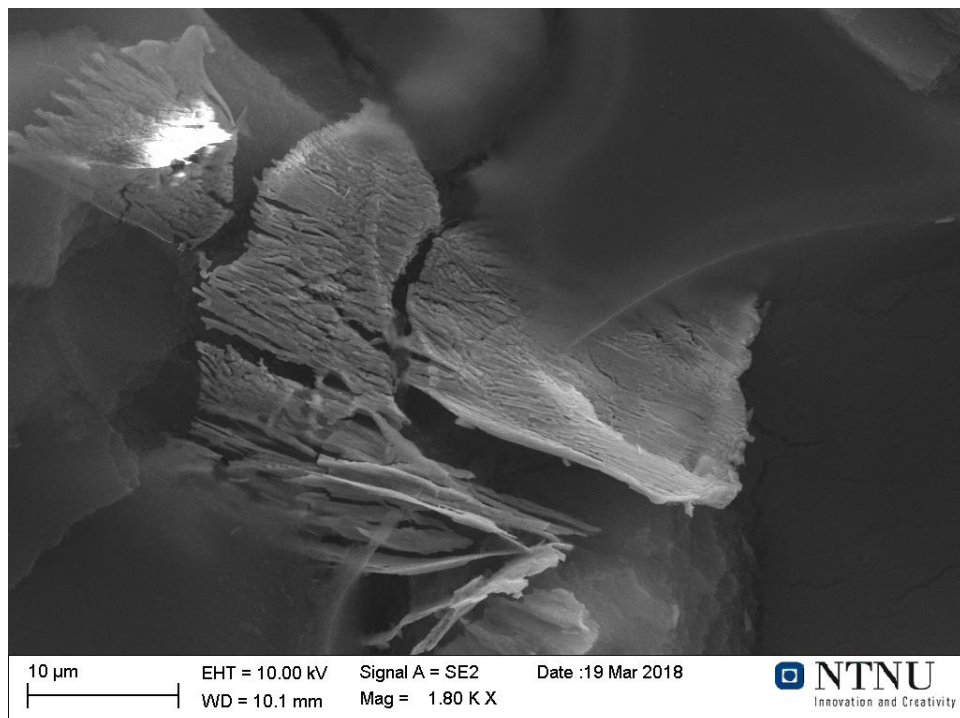

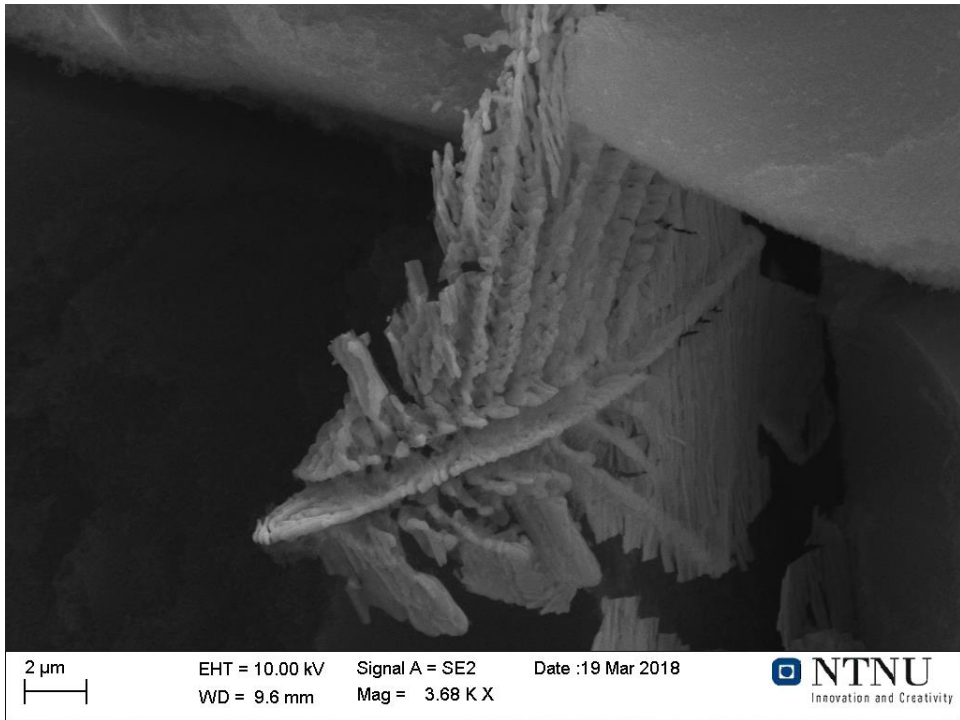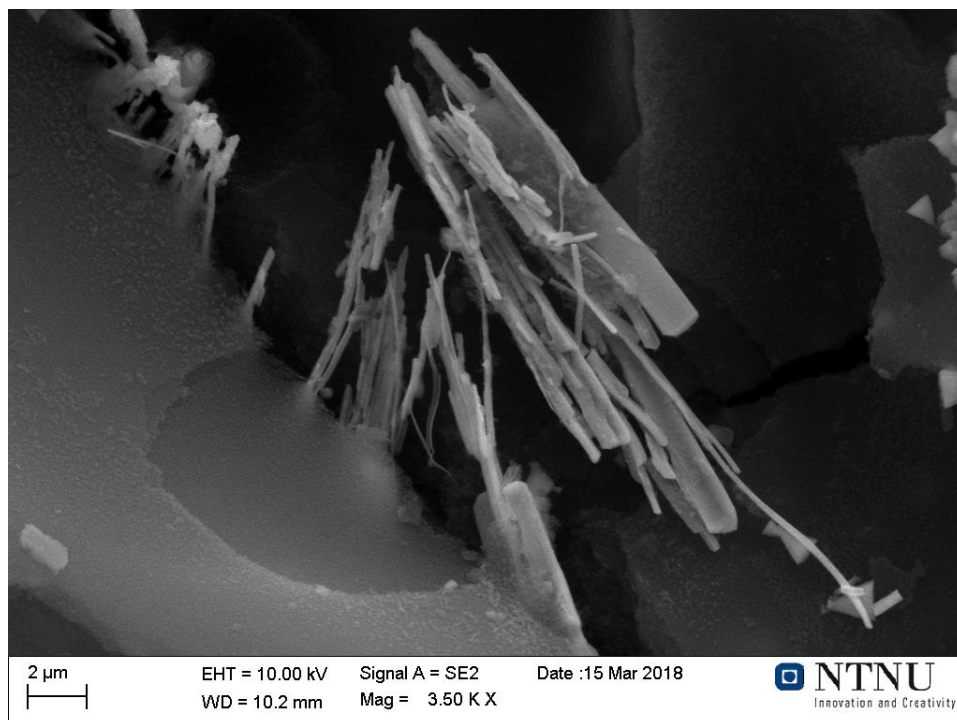*Figure 4.22: Particles with stacked plate morphology.*

Figure 4.23: Particle with plate-like morphology, where a kind of branching can be seen.

4.5.3   Sample T9

In sample T9, the fraction of morphologies indicating Al_3Fe increased. The needle-like and plate-like morphologies, described in the previous sub section, dominated, see Figure 4.24 and Figure 4.25, respectively. In addition, particles with curved flake-like morphology were observed, see Figure 4.26. Some particles with skeletal morphology indicating Al_mFe phase were also found. However, this morphology has been shown in the previous sub sections (e.g. Figure 4.15, Figure 4.16, Figure 4.19 and Figure 4.20) and is therefore not imaged in this sub section.

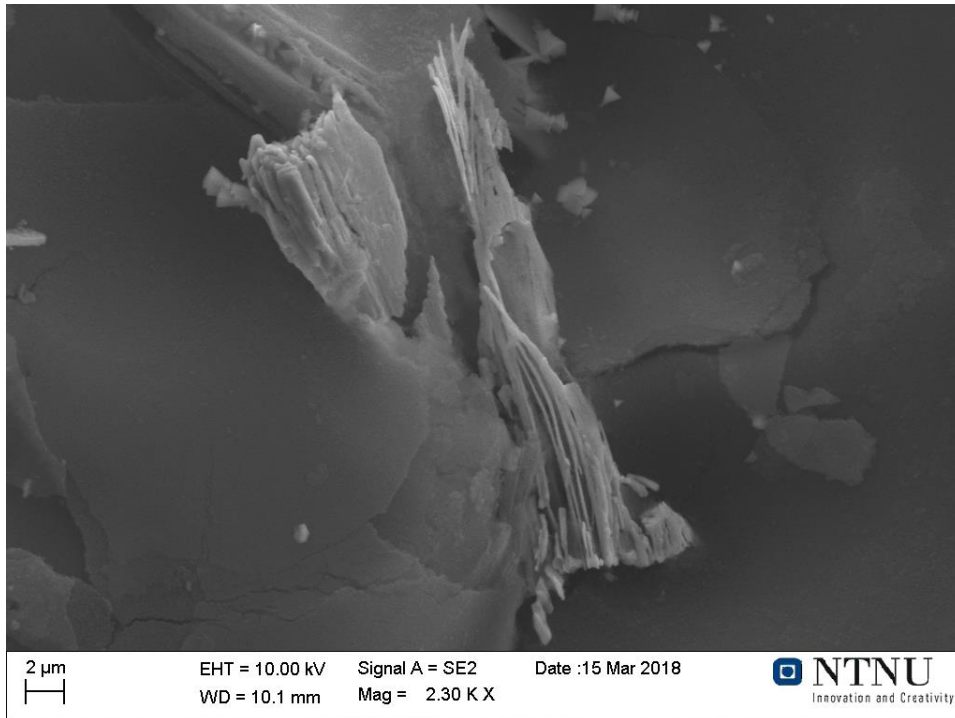*Figure 4.24: Bundle of particles with needle-, flake- and rod-like morphology.*

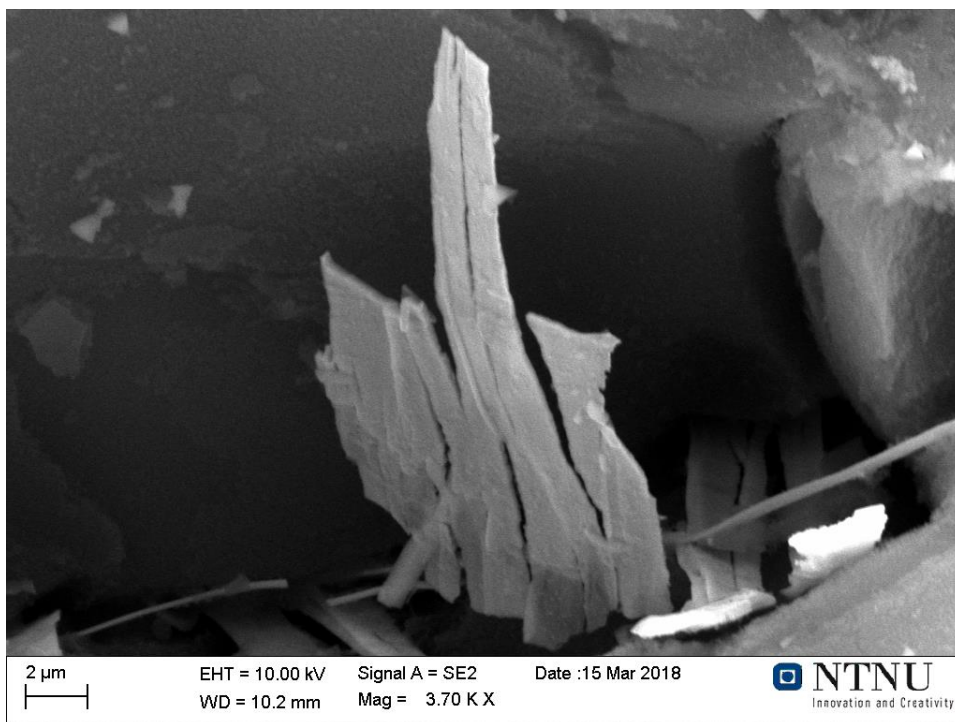*Figure 4.25: Particles with stacked plate morphology.*

Figure 4.26: Particle with flake-like morphology.

4.6 XRD

The quantitative analysis of the powder XRD data was carried out in the software TOPAS by the Rietveld refinement method. Figure 4.27 shows the distribution of iron bearing particles as a function of distance to surface. From the figure it can be seen that both Al_mFe and Al_3Fe is present in all the samples. Close to the surface, there is approximately 90 wt% Al_mFe and 10 wt% Al_3Fe. At 135 mm to surface, the relationship between the two phases is the opposite: approximately 10 wt% Al_mFe and 89 wt% Al_3Fe. Al_6Fe is also present at this distance, but just with approximately 1 wt%. The drop of Al_mFe between 65 to 79 mm in distance to surface should be noticed. Al_6Fe is not present at the samples closest to the surface. The phase can first be seen at 65 mm to surface. The wt% of Al_6Fe increases from 1 to 6 wt% from 65 to 79 mm in distance to surface. At 107 mm in distance to surface, the amount of Al_6Fe is still 6 wt%, but at 135 mm the amount decreases to 1 wt%. The results from the quantitative analysis of powder XRD measurements can also be seen in a table in Appendix 6.

The XRD spectra for each sample and the calculated diffraction pattern can be seen in Figure 4.28. The two space groups of Al_6Fe (Ccmm/Cmc2) are very much alike and give similar results for quantitative analysis. The crystallographic structure om Al_mFe is not completely established yet and there are two suggestions for space group for Al_mFe. I4/mmm and I$\bar{4}$2m are suggested by Skjerpe [41] and Gjønnes et al. [42], respectively. For analysis of the powder XRD data, the structure reported by Gjønnes et al. was used because the intensity was closer to the measured XRD data in this experiment. However, it is obvious that there is a significant discrepancy; a large intensity difference can be observed between the calculated and measured pattern for low intensity peaks. An estimation of 5 wt% of error was made based on observations. This will be further discussed later.
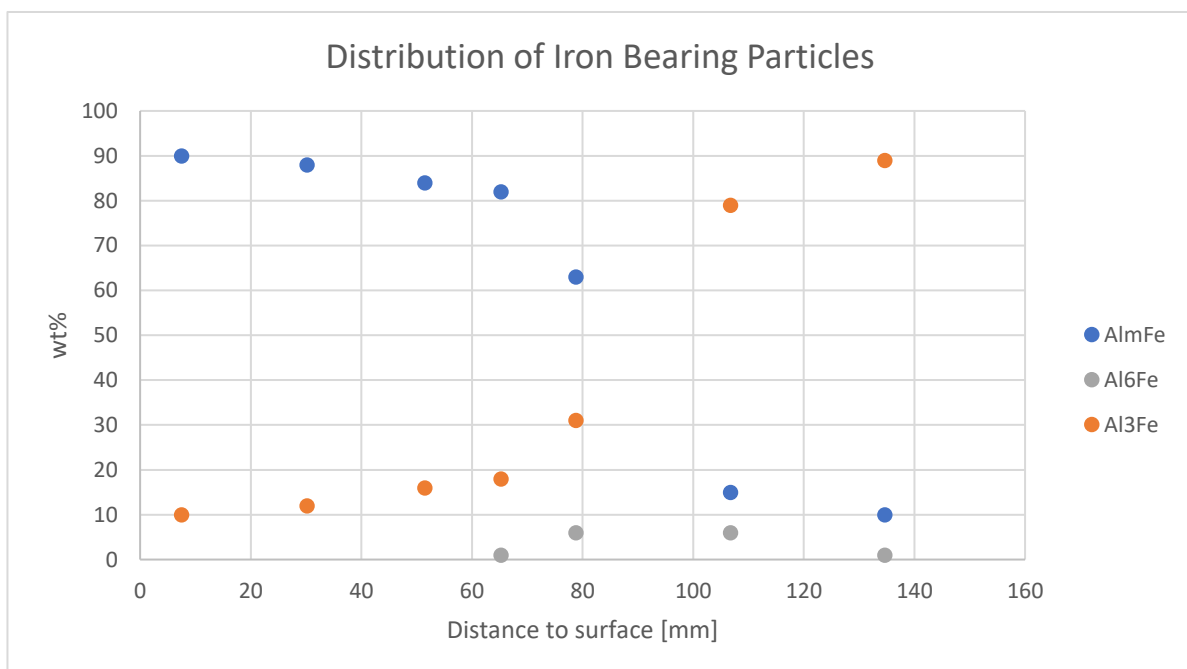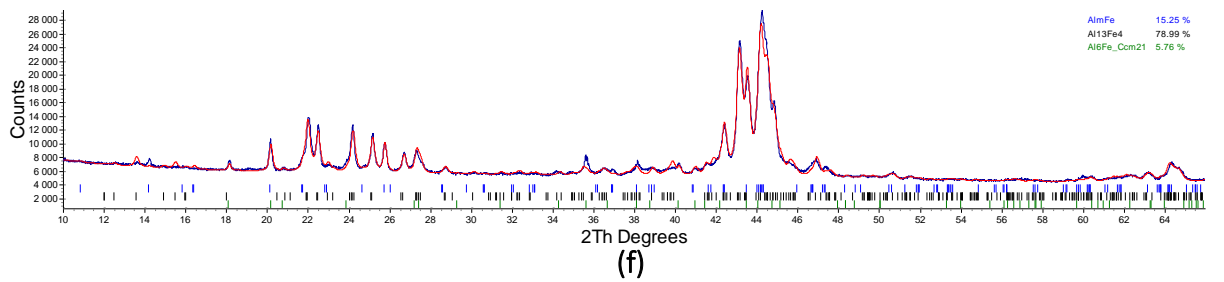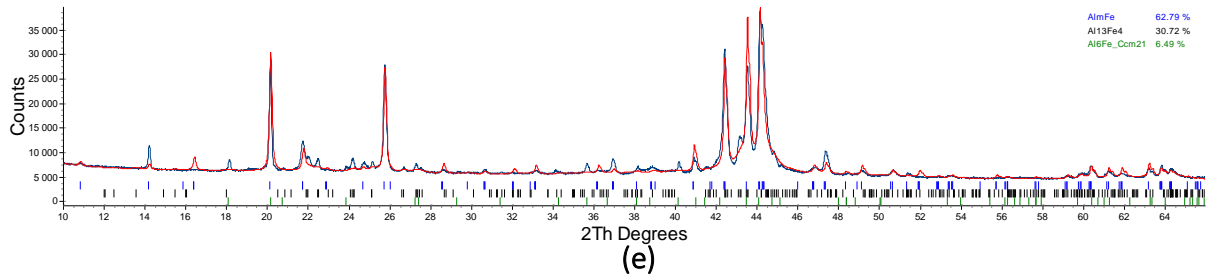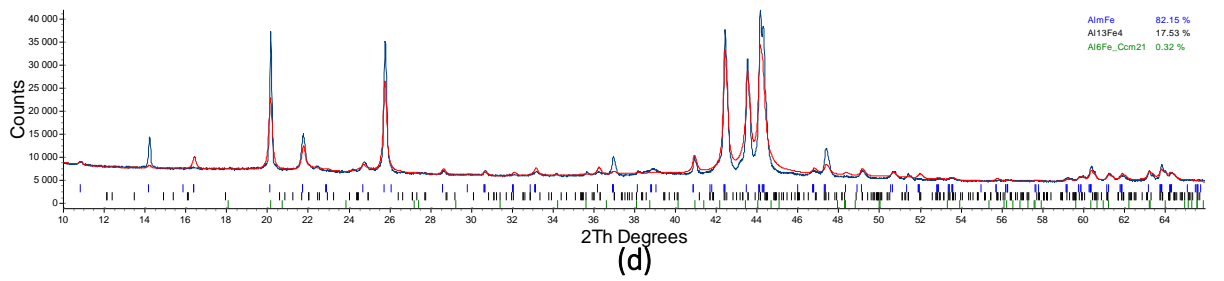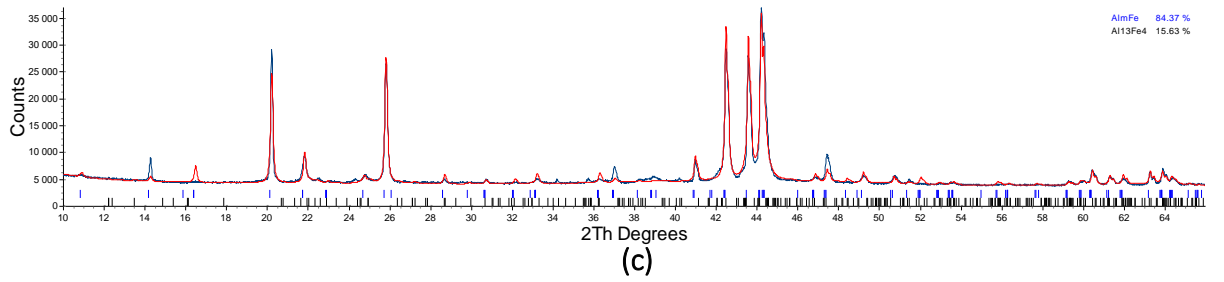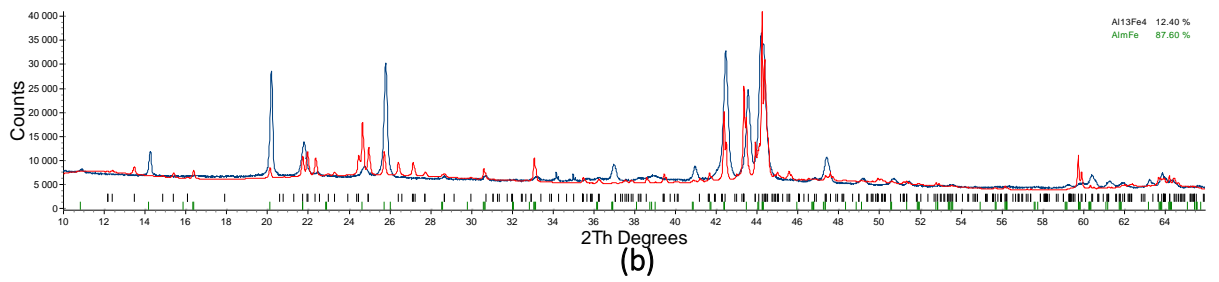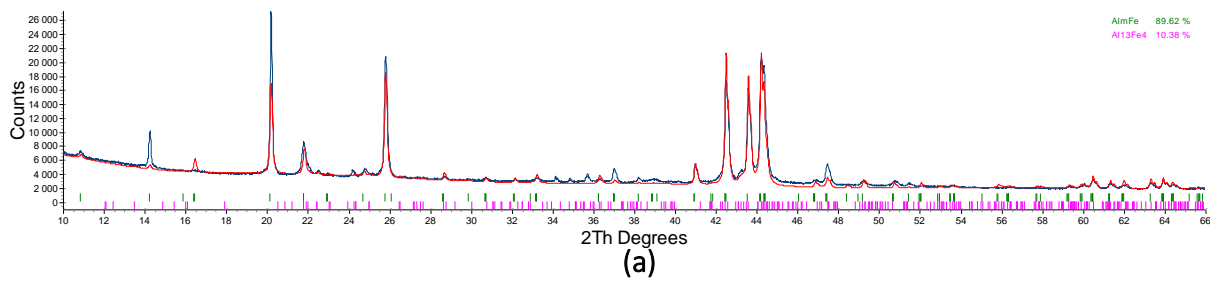

Figure 4.27: wt% of the different iron bearing particles as a function of mean distance to surface.
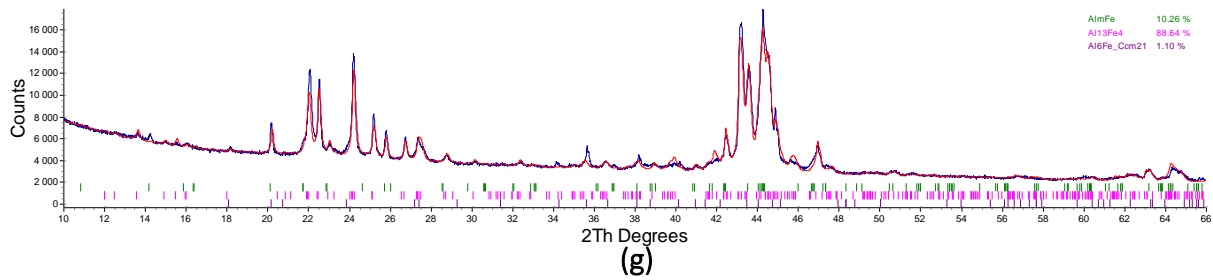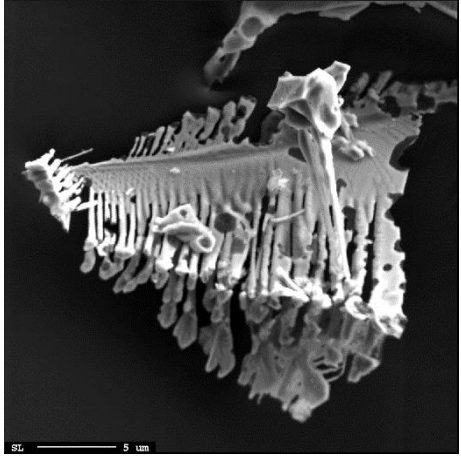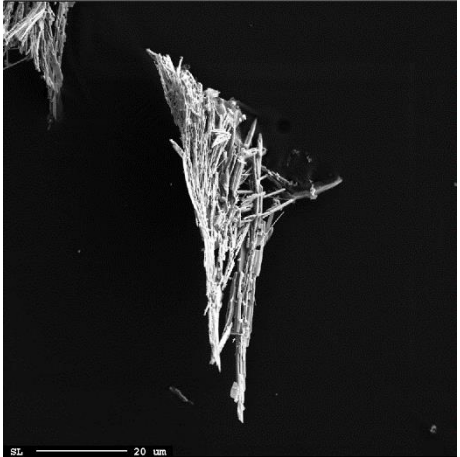
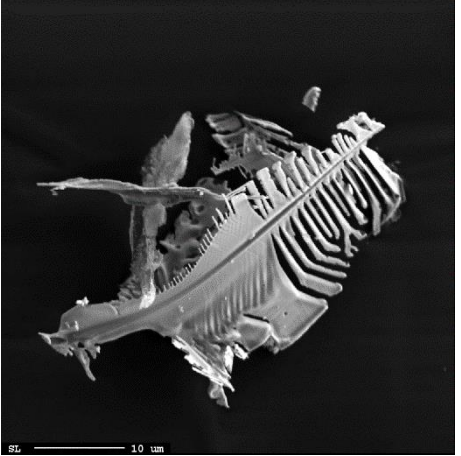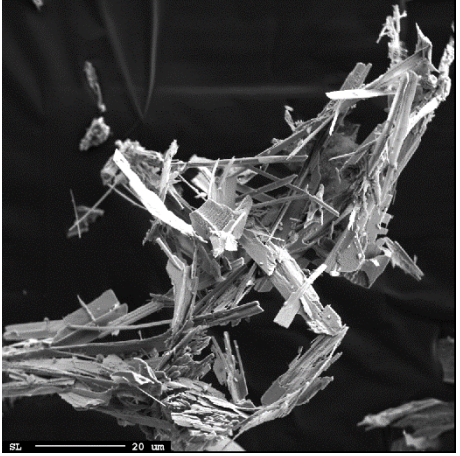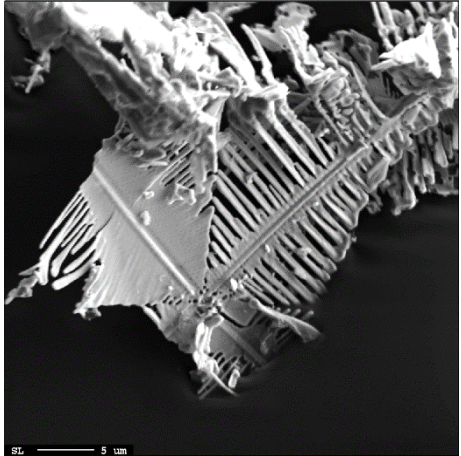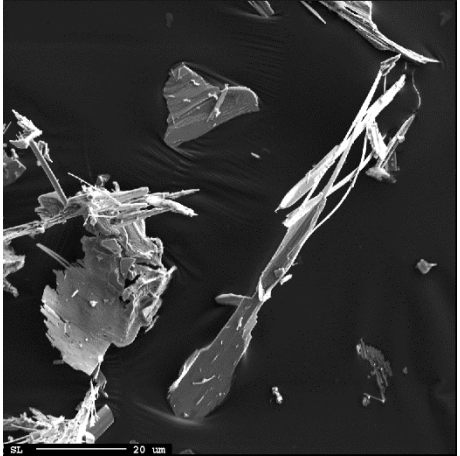*Figure 4.28: Measured XRD spectra (blue line) and calculated diffraction pattern (red line) for a) S1, b) S2, c), S3, d) S4, e) S5, f) S6, g) S7.*

4.6.1   Imaging of Particles Extracted by the Phenol Method

The powder from the sample close to surface (S1) and the sample corresponding to 134.7 mm in distance to surface (S7), was studied in SEM with the intention to perform WDS analyses on the iron bearing particles extracted from the aluminium matrix. The iron bearing particles have agglomerated and any WDS analyses would be futile. The agglomeration of particles made morphology study challenging. Some particles were not agglomerated, and the 3D morphology could be studied, see Table 4.11. The XRD results shows that Al_6Fe is not present in S1. Hence, the skeletal particles showed in Table 4.11 are Al_mFe. Example 1 shows a bit different branching of Al_mFe than shown in the deep etched morphology. For Example 2, the curved morphology and the flake-like area could be noticed. While Example 3, shows a particle where four main branches radiate in different directions, indicating Al_mFe phase. In S7, particles with the typical Al_3Fe needle-like morphology were found, along with particles with some particles with plate-like morphology, see Example 3.

67

Table 4.11: Examples of morphology of iron bearing particles extracted from the aluminium matrix by the phenol method.

Phase	Al$_m$Fe (S1)	Al$_3$Fe (S7)
Ex. 1		
Ex. 2		
Ex. 3		

5   Discussion

The last decades, a lot of research on the formation of Fir-tree structure and the iron bearing particles has been done. Though there has been extensive research within the topic, it is still a challenge to predict the formation of Fir-tree structure. The reason for this, is the difficulties with reliable phase identification of the iron bearing particles. Their small size and similar chemical composition make identification difficult. Thus, limited quantitative analysis have been done in this field. In this master thesis, the iron bearing particles were studied with different techniques:

-    Study of morphology in plane polished and deep etched samples
-    Electron backscatter diffraction (EBSD) technique
-    Wave length dispersive spectrometry (WDS)
-    X-ray diffraction (XRD)

Samples from a sheet ingot (600 mm x 1600 mm) of AA5005 alloy was studied. It is clear from the presented results that the three phases Al_mFe, Al_3Fe and Al_6Fe exist in the ingot. Identification of different iron bearing particles by morphology revealed in plane polished samples is not a sound method, at least not with respect to distinguishing Al_6Fe and Al_mFe since they have very similar characteristic morphology in 2D. In the following chapter, the results from the different techniques for identification of iron bearing particles will be discussed. When using WDS and EBSD the morphology of the particles can be linked to the identified phase. The results from EBSD and WDS will therefore be discussed first. Next, the quantitative analysis from Rietveld refinement of XRD measurements will discussed before the morphology of the particles will be interpreted. The techniques will be compared to study advantages and disadvantages with different identification techniques. Finally, the results will be put in context with cooling rate calculations to study why there was a Fir-tree structure in this particular sheet ingot.

5.1 EBSD

Zhang et al. [24] explored the possibility to use a combination of EBSD and EDS for phase identification of iron bearing particles, instead of performing powder XRD on particles extracted by the butanol method. The intention was to achieve a quantitative analysis without needing to extract the iron bearing particles from the aluminium matrix, as this can be a rather time-consuming process. However, the article does not mention any details about settings on the SEM or the software to manage to identify all the particles. In this project, only certain large particles could be positively identified by EBSD due to low pattern quality. Consequently, EBSD could only be used for qualitative analysis.

When the samples were studied in SEM by EBSD, it was clear that only some particles had a high enough pattern quality for phase identification. Thus, mapping could not be performed, and the particles were identified by single spot analyses. That means that every pattern needed to be indexed manually and carefully evaluated. The reason for poor pattern quality can be both due to the EBSD detector and the material itself, as mentioned in Section 2.4.1. Two different EBSD detectors were tried: one high-speed detector and one high-resolution detector. At the best, the high-speed detector gave patterns which were very noisy and only a few Kikuchi bands were barely visible. These patterns were very difficult to index and could not be used for reliable phase identification. Mostly, a pattern could not be acquired by using this detector. With so poor initial results, no great effort was made to try to optimize the settings in the software.

By changing to the high-resolution detector, the pattern quality improved significantly. The parameters in the software were optimized. Electron backscatter patterns (EBSPs) were acquired from particles with different characteristic morphologies. However, only certain particles had good enough pattern quality, although the EBSD detector was changed and the software settings optimized. The width of both the particles with skeletal and needle-like morphology could be very small (<1 µm). It is therefore likely that the interaction volume could then be larger than the particle itself, resulting in a noisy EBSP. To increase the possibility of good pattern quality, the EBSD was carried out on the samples closest to the center of the ingot, where the particles are largest. When particles gave a good pattern, it was easy to distinguish between the particles as the solutions gave great difference in the fitting parameter.

From the EBSD the skeletal particles were identified as Al_mFe and the particles with needle-like morphology as Al_3Fe. Particles identified as Al_6Fe by EBSD showed a plate-like morphology. The Al_6Fe particles were adjacent to particles identified as Al_3Fe or unidentified particles with the typical needle-like morphology indicating Al_3Fe phase. From the morphology study, the skeletal particles dominated close to the surface, while particles with needle-like morphology dominated closer to the center of the ingot. This EBSD results indicate that there is a transition from Al_mFe to Al_3Fe as a dominating phase at a certain distance to surface. The EBSD results also indicate that the fraction of Al_6Fe is small.

5.2 WDS

As mentioned in the introduction part, this master thesis builds on a specialization project from the previous fall [43]. In that project, it was tried to distinguish between the iron bearing particles by EDS. It was evident that the interaction volume was larger than the particles themselves and EDS could thus not be used to distinguish between the different phases. Zhang et al. also found EDS often to be insufficient to distinguish between iron bearing particles [24]. In their study, EDS was used to determine elements which were present. Therefore, an attempt to distinguish the particles by WDS was made in this thesis.

A criterion for a successful quantitative analysis, is that the interaction volume is not larger than the particle itself, as presented in Section 2.4.2. The density of Al_6Fe and Al_3Fe are 3.450 and 3.770 g/cm^3, respectively [23]. This gives a diffusion range of approximately 2 μm when an accelerating voltage of 15 kV is applied. If the accelerating voltage is lowered to 10 kV, the diffusion range decreases to approximately 1μm. That means, if the dept of the analysed particle is smaller than 1 μm, the diffusion range will be larger than the particle self. This will result in an incorrect quantitative analysis because a large volume fraction of the Al-matrix will be included in the interaction volume. It can be discovered if the interaction volume is too large by looking at the total weight percent of the WDS-analysis. If the total weight percent is too high (>103 wt%), it is an indication of that the matrix is diffusion range and the quantitative analysis cannot be trusted [44].

A lower accelerating voltage was used for WDS analyses compared to last year's EDS analyses (10 kV vs. 15 kV). This reduced the interaction volume. In addition, a quantitative analysis of a particle can be achieved with WDS since ZAF-correction is used. However, there were still challenges to achieve successful quantitative analyses. The particles for analysis were carefully selected to find particles which hopefully were big enough for analyses, but most of the parts which constitute the particle were very small (width less than 1 μm). For the sample closest to the surface, where the particles are the smallest, only 50% of the analyses were successful. This was also the case for the sample with longest distance to surface (T9), where the dominating morphology were the thin needles. It should be emphasized that the crucial size of the particle is not what is seen in the surface, but the depth of the particle below the surface. Even if surface area exceeds 1 μm, the dept of the particle does not necessarily do it, see Figure 5.1 for illustration. One of the characteristic morphologies were stacked plate. In 2D these plates looked like larger particles. In deep etched samples it was revealed that the thickness of these plates was in the scale of nanometers, explaining the poor analyses on such particles.
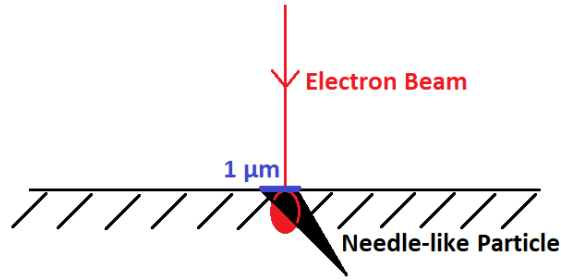
Figure 5.1: Schematic illustration of critical interaction volume

The results from EBSD indicated that three different phases were present in the sample material. The present WDS results shows that WDS analysis is not precise enough to determine the exact chemical formula for each analysed particle. Instead, three groups of particles could be defined, see Section 4.4. Most of the analyses were in the range 18.9-24.0 at% Fe. In addition, it was clear that particles with considerable lower amount of Fe existed in the alloy. These particles were only found at 7.2 and 10.4 cm in distance to surface and contained 14.3-15.5 at% Fe. This corresponds well with the atomic percent of the phase Al_6Fe, see Table 5.1. Since WDS is not precise enough to determine the exact chemical formula, the analyses must be interpreted together with the morphology of the particle. From EBSD results, it could be seen that the particles with skeletal morphology corresponded to Al_mFe and particles with needle-like morphology corresponded to Al_3Fe. Taking this into consideration, the analyses which had 18.9-24.0 at% Fe could be divided into two groups: 18.9-21.3 at% Fe, which indicates Al_mFe and 21.8-24.0 at% Fe, which indicates Al_3Fe. In this way, particles that did no display one of the characteristic morphologies could also be identified. Examples of this was shown in Table 4.6 and Table 4.7.

Table 5.1: at% of the different iron bearing particles

Particle	at% Fe
Al_mFe (m= 4.0-4.4)	20.0-18.5
Al_3Fe ($Al_{13}Fe_4$)	23.5
Al_6Fe	14.3

The set range for Al_3Fe (21.8-24.0 at% Fe) has in some degree lower amount of Fe than expected. From the morphology study, it could be seen that the particles with needle-like morphology were very thin. Probably in some of the analyses, a small amount of the matrix has been within the interaction volume, giving a higher Al/Fe ratio than expected. For the Al_mFe phase it is the opposite: the set range for Al_mFe (18.9-21.3 at% Fe) has a higher amount of Fe compared to the chemical formula (the value of m is often reported to be 4.4, meaning, the at% of Fe should be close to 18.5). The reason for the high limit for Al_mFe can be due to particles

with topography. Though the samples have been carefully polished, some topography in the particles could be seen. If the topography of an analysed particle is an obstacle for the produced X-rays, e.g. characteristic X-rays from Al, it will influence the intensity of the element and thereby the quantitative analysis. The result can be a lower Al/Fe ratio than the expected value. Since the Al/Fe ratio is very similar for the iron bearing particles, the analysis will be highly sensitive for errors, e.g. small topography in sample surface. The similar Al/Fe ratio for the different phases are one of the main reason why it is a challenge the use WDS and EDS technique to distinguish between the phases.

As mentioned, the analyses had to be performed on the largest particles to avoid that the interaction volume exceeded the particle size. To look for large particles was time-consuming, as most of the particles were regarded as too small for quantitative analysis by the operator of the SEM. That means, if one of the phases is in average smaller than the other phases, this phase is not likely to be chosen for any analyses. This will affect the statistics of measured fraction of different phases. This can be one reason why Al_3Fe is not found in the samples close to the surface by WDS analyses, but identified close to the surface by XRD, see Figure 4.12 and Figure 4.27, respectively.

The content of alloying elements in the particles can be used to support the argument of different phases present. The analyses which indicates Al_6Fe, shows approximately no Si. This is in good correspondence with theory, since Al_6Fe cannot dissolve any Si [23]. The analyses indicating Al_mFe have large variations in content of Si and Mg. In general, Al_mFe showed to have higher content of both Si and Mg than Al_6Fe and Al_3Fe did.

From WDS it was found that Al_mFe, Al_3Fe and Al_6Fe existed in the chosen slice of the sheet ingot. The WDS analyses indicated that Al_mFe was the only phase present until a distance of 7.2 cm in distance to surface. At this distance, all three phases were identified, and it seemed to be a transition area. Further towards the center of the ingot, the fraction of Al_mFe decreases, while the fraction of Al_3Fe increases. Only a small fraction is Al_6Fe is found, at 7.2 and 10.4 cm in distance to surface. The WDS analyses showed that the particles with skeletal morphology is mainly Al_mFe, but that Al_6Fe also can exist with a skeletal-like morphology. The analyses showed that Al_mFe is often displayed without the characteristic skeletal morphology. The dominating morphology of Al_3Fe was needle-like, but the phase could also exist with plate-like morphology. Al_6Fe was also identified with plate-like morphology.

5.3 XRD

The iron bearing particles were successfully extracted from the aluminium matrix by the phenol method. The XRD results shows that both Al_mFe and Al_3Fe are present at the surface and at 135 mm in distance to surface. The fraction of the two phases are inversely correlated. Close to the surface, there is approximately 90 wt% Al_mFe and 10 wt% Al_3Fe, while at 135 mm to surface the relationship between the two phases is approximately opposite. From the XRD results, it can be seen that Al_6Fe only make up a small fraction of the iron bearing particles and that the phase is only present 65-135 mm away from the surface.

The XRD data was analyzed using the TOPAS software. Al_mFe, Al_3Fe and Al_6Fe were the phases which were expected. Most of the peaks in the powder XRD data were identified to belong to the characteristic XRD pattern for one these three phases. However, in each sample there were 4 peaks which were not identified, see highlighted peaks in Figure 5.2. To try to find out what these unidentified peaks were, powder from the sample close to surface and the sample with the longest distance to surface, were studied in a SEM equipped with both WDS and EDS. In both samples, large plates that did not seem to be iron bearing particles were observed, see Figure 5.3. The plates were too thin for quantitative analysis (WDS). The EDS analysis gave strong signals of O, but also indicated presence of Al, Mg, Si, Ni, Fe, C and P. Al, Si, Al_5Fe_2, $Al_8FeMg_3Si_5$ and many different oxides were tested in the TOPAS software afterwards, but no match with the unidentified peaks was found. Other researchers who have used the phenol method, have reported that aluminium phenolate can form and contaminate the sample [35]. The available crystallographic information about aluminium phenolate is limited to one article [45]. From the different complexes described in this paper, two of the aluminium phenolate complexes could be excluded based on peak positions. A third one, $C_{18}H_{36}N_2OAl_2$, could not be excluded based on peak positions. Since the intensities were not described physically based, this is not proof that the aluminium phenolate complex is present. However, it will be surprising if such a large complex produces these narrow, unknown peaks. The peaks were not identified, so whether they originate from an unknown phase or contamination from the phenol method, was not determined. When the distribution of phases changed from sample to sample, the unidentified peaks did not alter much. Hence, the unidentified phase does not influence the ratio between the found phases in the quantitative analyses.
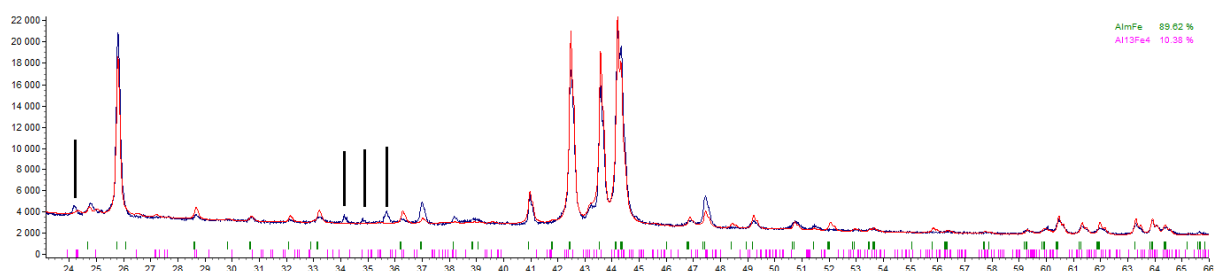

Figure 5.2: XRD spectra and calculated diffraction pattern for S1. Four unidentified peaks are highlighted with black lines.
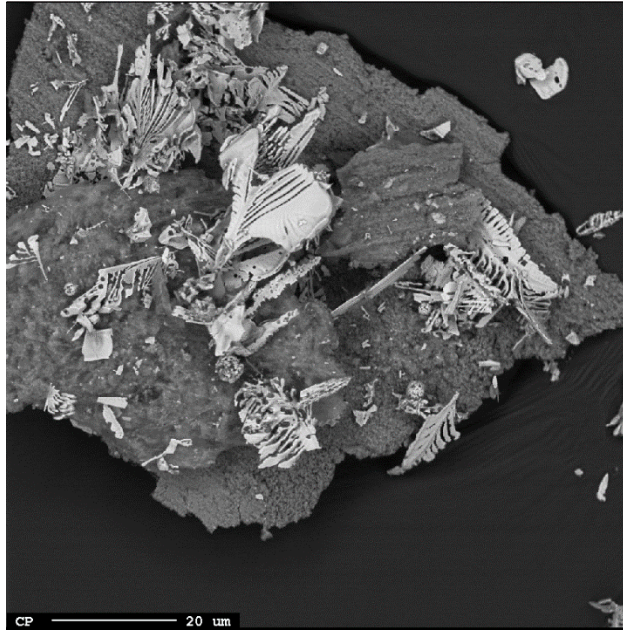
Figure 5.3: Example of large plate found in the powder samples after extraction of iron bearing particles in aluminium matrix by the phenol method.

For the Al_mFe phase, a remarkable discrepancy from the used structural model and the present data was observed. There was a good match in both peak position and intensity for the peaks with highest intensities. Some of the lower intensity peaks matched in peak position, but it was a significant too high or low intensity compared to the experimental data. This indicates that some details of the information about the crystallographic structure are not appropriately described. This change in intensity distribution can be due to Fe atoms and vacancies are differently arranged compared to the structure described by Gjønnes et al.[42] In addition, it cannot be excluded that due to ordering of Fe and vacancies, different superstructures of Al_mFe exists. Furthermore, both Skjerpe [41] and Gjønnes et al. reported extensive faults in the crystal, which can have a significant effect on powder XRD compared to electron diffraction in a TEM. Due to the remarkable discrepancy from the used structural model and the present data, a significant error in the phase fractions can be expected. An estimation of 5 wt% in uncertainty was made based on observations. The phase fractions in the different samples should therefore not be regarded as absolute, but the trend between the different samples should be correct.

5.4 Grain Size

As shown in Figure 4.1-Figure 4.4, the majority of the samples had a globular grain structure, which made precise measurements of SDAS difficult. To get indications of the local cooling rates, the grain size was instead measured. The grain size is inversely correlated to the cooling rate; the grain size increases with decreasing cooling rate [21]. There was a small increase in grain size from 0.8-5.6 cm to 7.2-10.4 cm in distance to surface and a more pronounced increase from the samples corresponding to 7.2-10.4 cm to 12.0-13.6 cm in distance to surface. This is as expected, since the cooling rate will be highest close to the surface due to the effect of primary and secondary cooling in DC casting. The cooling rate will decrease towards the center of the ingot due to longer thermal diffusion paths.

5.5 Morphology of Particles

From WDS and XRD results, it is clear that the distribution of the different phases changes from the surface to the center of the ingot. This change could also be observed by studying plane polished samples in light microscope (LM) Close to the surface, where the cooling rate is highest, the dominating characteristic morphology of the particles were skeletal. The skeletal morphology dominated until a distance to surface of 5.6 cm. At 12.0-13.6 cm in distance to surface, where the cooling rate is lower, the dominating characteristic morphology of the particle were needle-like. There seemed to be a transition area at 7.2-10.4 cm in distance to surface, as there seemed to be a mix of both skeletal and needle-like particles in this region. The skeletal morphology consists of several thin branches which are located along grain boundaries. The extent of the particle can therefore appear with a curved morphology, as seen in Figure 4.6. This morphology indicates the Al_mFe or Al_6Fe phase. The needle-like particles were described as sharp needles which seemed to cluster together, see Figure 4.7. This indicates the Al_3Fe phase. This is in accordance with previous studies that have shown that Al_6Fe and Al_mFe nucleate at a higher cooling rate than Al_3Fe.

The frequent branching of the Al_mFe and Al_6Fe phases give rise to a number of characteristic morphologies. In plane polished samples, the morphology is usually just a cross section of the 3D particles. Depending on the orientation of the particle, the projection can be of many of the branches, the principal branch or only a few of the branches. Consequently, a lot of the particles do not display a characteristic morphology (skeletal or needle-like) in a plane polished surface. An example of this is the particle in the upper corner of Figure 4.6 a) where a kind of round particle can be seen, without any other particles adjacent. Particles with such morphology are impossible to interpret just by 2D imaging. In a study by Zhang et al., it was found that less than 20% of the total number of particles had a characteristic morphology [24].

Since both Al_mFe and Al_6Fe frequently branch and display quite a similar morphology, it is a challenge to distinguish between the two phases. It was not observed any particles with frequent branching which displayed a distinct different morphology than the described skeletal

one. In other words, by only studying plane polished samples it cannot be determined whether Al_mFe, Al_6Fe or both phases are present. Since EBSD, WDS and XRD showed that Al_6Fe only exists as a minority phase, most of the particles with skeletal morphology are assumed to be Al_mFe. The needle-like morphology is considerably different than the skeletal morphology and a clear indication of Al_3Fe phase. Though morphology study cannot give reliable phase identification, information of areas of interest can quickly be obtained by studying plane polished samples. Figure 5.4 shows what kind of morphology that dominated as a function of distance to surface.
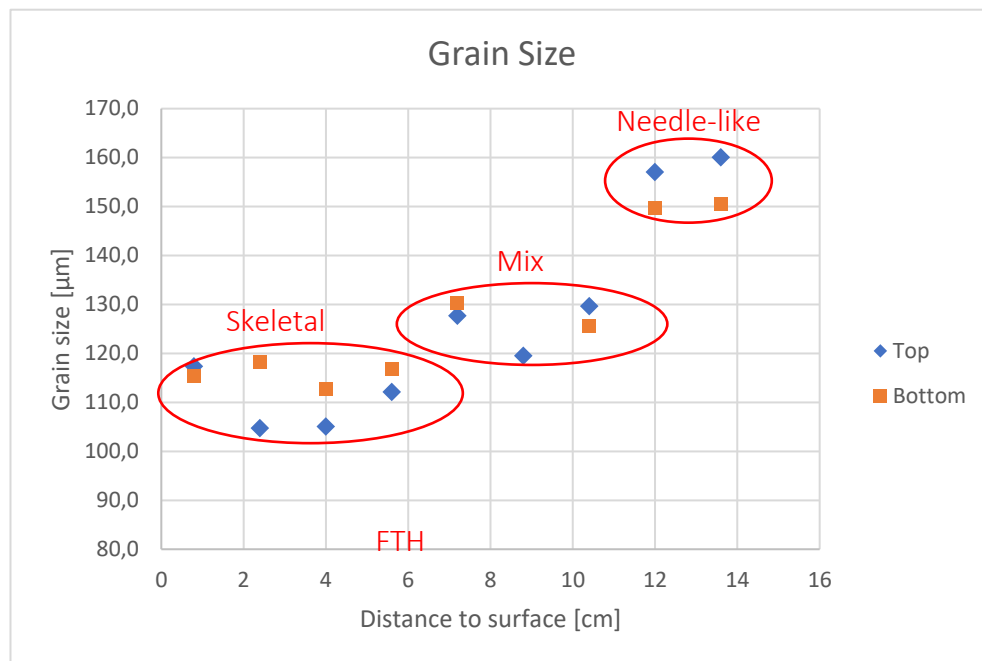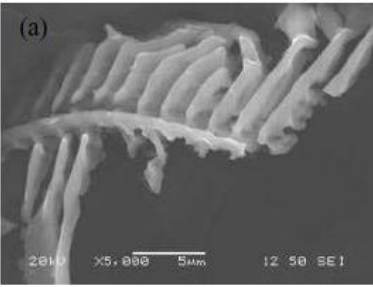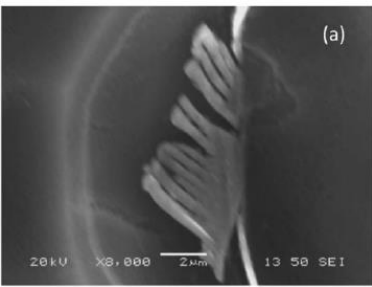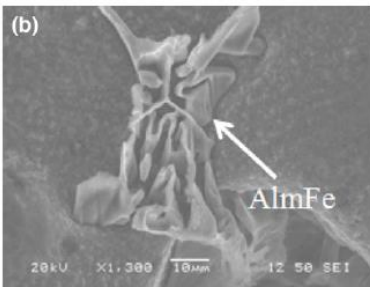
Figure 5.4: Correlation between iron bearing particle and grain size (cooling rate), the measured minimum Fir-tree height is marked as FTH.

The deep etched samples revealed more about the true morphology of the different iron bearing particles as it enabled 3D study of morphologies. When the surrounding aluminium matrix was etched away, the samples gave more information about growth of eutectic particles than plane polished samples did. Nevertheless, studying the particles in 3D can be confusing and there are not that many studies which have identified iron bearing particles in this manner. In addition, the morphology of particles will change with cooling rate and chemical composition of the alloy, this is illustrated in Table 5.2. Hence, it is difficult to compare the morphologies of particles found in this material with morphologies from other studies.

Table 5.2: The morphology of AlmFe is dependent on the chemical composition of the alloy

Alloy	AA5657	AA5657	A206
Morphology in 3D			
Ref.	[24]	[13]	[27]

5.6 Summary: Best Approach for Characterization of Fir-tree Structure

As mentioned before in the thesis, it is still difficult to predict formation of Fir-tree structure, though it has been extensively researched within the field. The iron bearing particles causing the Fir-tree structure phenomenon, are usually very small and have similar chemical composition, which complicate the analysis. A combination of different identification techniques will decrease the possibility of misidentification. In this study, the different identification techniques have good consistency:

I) Morphology study

Both EBSD and WDS analyses indicates that most of the particles with skeletal morphology in plane polished samples are Al_mFe. Particles with needle-like morphology were identified as Al_3Fe by both EBSD and WDS analyses. Both techniques also showed that Al_3Fe can have plate-like morphology. Few analyses indicated the existence of Al_6Fe phase. However, the particles identified as Al_6Fe were found at the same distance to ingot surface by the two techniques. By EBSD, the morphology of Al_6Fe was plate-like. By WDS analyses, the morphology of Al_6Fe was either skeletal-like or plate-like.

II) The distribution of the phases

The morphology study indicates that the distribution of the phases changed from the surface of the ingot to the center. By studying the samples in LM, a transition area was noticed. This is supported by WDS analyses which showed that the dominating phase close to surface was Al_mFe, while the dominating phase at the longest distance to surface was Al_3Fe. These characterizations support the quantitative analysis of XRD measurements. Hence, the quantitative analysis is reliable.

Different methods for extracting the iron bearing particles have been tried, but the extraction methods are regarded as time-consuming experiments. That is why Zhang et al. performed a study with quantitative analyses based on a combination of EBSD and EDS [24]. In a selected area in a sample, every particle needed to be identified to perform quantitative analysis by an image analysis. However, not all particles can be identified by those techniques due to the size of the particles. In the present study, only a minority of the particles gave a satisfying EBSP for phase identification and quantitative analyses by image analysis were not feasible. In addition, to prepare high quality sample surfaces for EBSD of small particles are challenging and the post-processing with indexing of EBSP must be done carefully and for every single particle. Hence, the process is also time-consuming.

The phenol method had not been carried out at the department before. The XRD results showed that the method was successful. From the dissolution process, it was clear that thin sheets reduced the dissolution time. After some trial and error, the best cutting speed to prepare unbroken sheets with a thickness of approximately 0.3 mm, was found to be 0.100 mm/s. Consequently, the preparation of samples demanded some time. Newer versions of the cutting machine with an option to program the machine to prepare all the samples automatically exists. If this experiment is going to be carried out in a larger scale, this will reduce the time cost significantly. Since the particles are very light, it was challenging to get proper sedimentation when centrifuging the particles in methanol. By long-time centrifuging (20 min) and by carefully discarding the supernatant solution, most of the particles were kept. To improve this part of the process and to reduce the time, it is suggested to use a more powerful centrifuge so that the lightest particles can sediment more easily. By doing these two small improvements, the procedure for extraction of iron bearing particles will not be such a work-demanding process. Several samples across the thickness of a sheet ingot can then quickly be prepared.

The phenol method and quantitative analysis achieved by powder XRD seems to be the most reliable and fastest method for quantitative characterization of iron bearing particles. The iron bearing particles are extracted from samples à 3 g, which gives good statistics since numerous particles are analyzed. By the combination of EBSD and EDS, a limited number of particles are identified. The experience from the present work, does not imply that the combination of EBSD and WDS will reduce the time for sample characterization. In this case, the techniques are not as reliable as XRD, due to the reasons discussed in previous sections.

5.7   Formation of Fir-tree Structure

There have been performed several studies on the phase that causes the formation of Fir-tree structure, Al_mFe phase. Though Al_mFe has formed, it has not necessarily caused formation of Fir-tree structure. It therefore seems like there is a critical fraction of Al_mFe that causes Fir-tree structure. This will be further discussed in this section. In addition, the cooling rate and chemical composition of alloy will be discussed to look into why Al_mFe was the dominating phase in the subsurface region.

5.7.1   Cooling Rate

The *minimum* Fir-tree height in this material was measured to be 59 mm. The defect Fir-tree structure was named due to the looks as a fir-tree. Thus, the fir-tree height will vary along the length of the ingot. The XRD-results showed a drop in the fraction of Al_mFe from 82 to 63 wt% ($\pm$5 wt%) between 65.3 and 78.8 mm in distance to surface (critical zone), see illustration in Figure 5.5. This indicates that there can be a critical fraction of Al_mFe will give a Fir-tree structure, roughly 80 wt% Al_mFe. The change in dominating phase between approximately 78.8 and 106.8 mm in distance to ingot surface is also of interest.
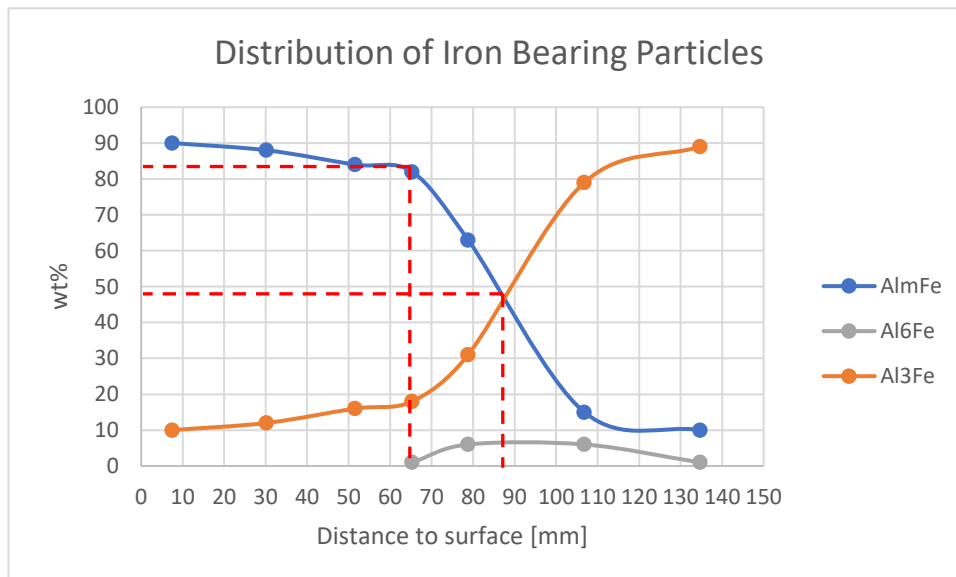
Figure 5.5: wt% of the different iron bearing particles as a function of mean distance to surface. Point of fraction drop in Al_mFe and point of change in dominating phase are marked.

But if the present data is compared with data from other studies, one can get indications that it is not only the high fraction of Al_mFe which causes the formation of Fir-tree structure. Zhang et al. have recently studied how Ni and V influence phase selection in AA5657 [13]. However, none of the materials got visible Fir-tree structure. To study the phase transition across a Fir-tree structure, they characterized a slice of AA1050 with visible Fir-tree structure, see Figure 5.6 [4]. The Fir-tree height was measured to be 6-8 mm. Close to the surface, the Al_mFe phase was dominating with approximately 75 vol% of all iron bearing particles. At 6 mm in distance to surface, both Al_mFe and Al_6Fe were major phases. Al_6Fe was the dominating phase at 9 mm in distance to surface and further towards the center of the ingot. It is a clear correlation between the fraction of Al_mFe and Al_6Fe. Figure 5.7 shows the phase distribution in a slice of AA5657 with no visible Fir-tree structure. It can be seen that the fraction of Al_mFe close to the surface is high and that it drops at 40 mm in distance to surface. However, there is no phase which has simultaneously increase in fraction. The fraction of the phases α-AlFeSi (Al_7Fe_2Si), Al_3Fe and Al_6Fe increases with increased distance to surface, but the Al_mFe is still the dominating phase. Thus, it can be proposed that it is not a critical fraction of Al_mFe that causes the Fir-tree structure, but the sudden change in dominating phase from Al_mFe to Al_3Fe or from Al_mFe to Al_6Fe.
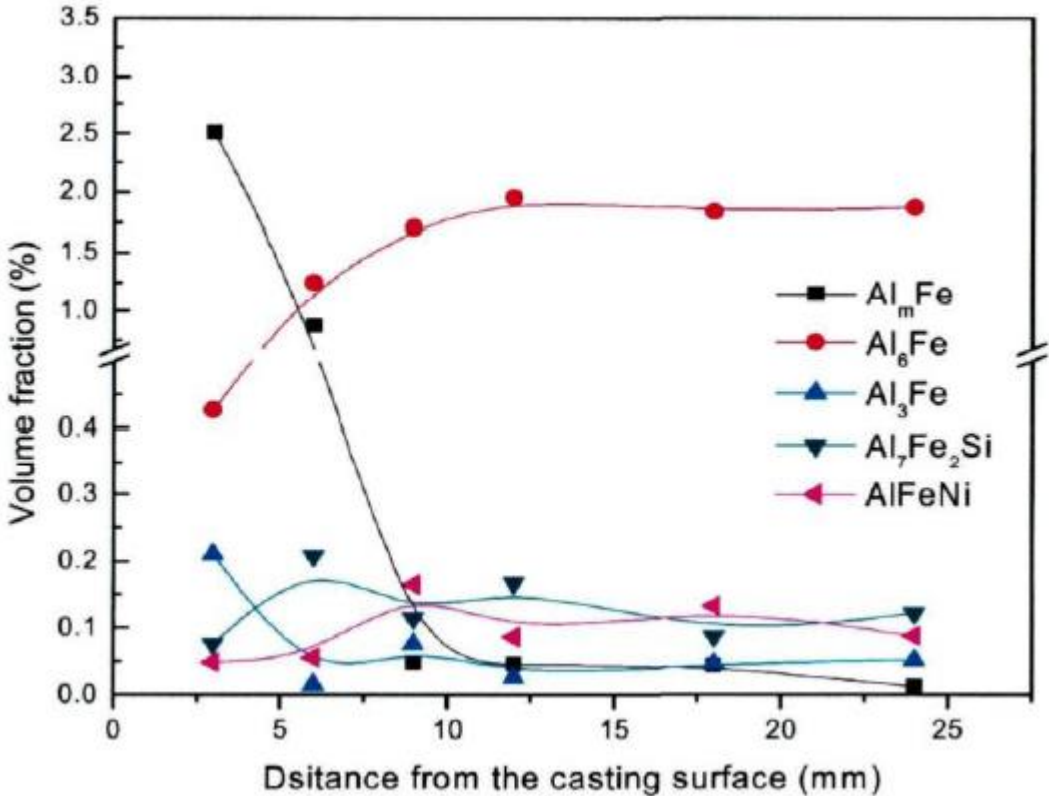
Figure 5.6: The distribution of iron bearing particles across an AA1050 ingot with visible Fir-tree structure [4].
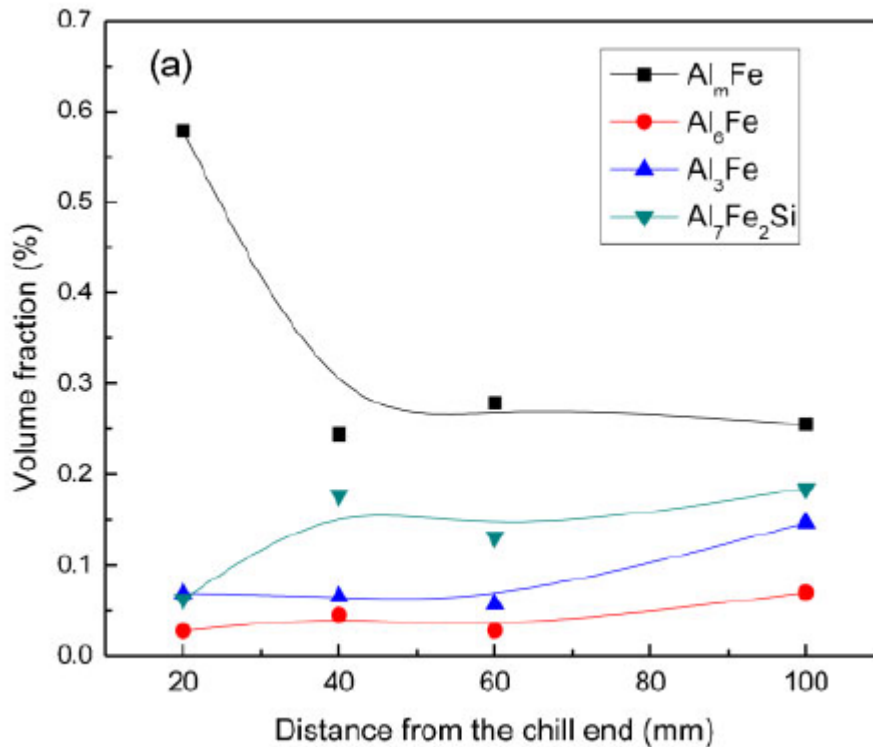
Figure 5.7: The distribution of iron bearing particles across an AA5657 sample from DC simulator [13].

The high fraction of Al_mFe must be put in context with the cooling rate, as this has been discussed to be one of the most critical factors for formation of Al_mFe and Fir-tree structure. As mentioned in Section 2.3.1, different critical cooling rates for formation of Al_mFe has been reported. Miki et al. reported that the cooling rate must be above 10 K/s for Al_mFe to form [6]. In one study, it was reported that for AA5005, the critical cooling rate for formation of Al_mFe and Fir-tree structure was 8.5 K/s [23]. The calculated cooling rate given in Section 2.1.2, shows that close to the surface of the ingot, the cooling rate is approximately 8 K/s. It is in the same range as the reported values and Al_mFe can therefore be expected to form at the surface.

Between 78.3 and 106.3 mm in distance, there was a change in dominating phase from Al_mFe to Al_3Fe. Figure 5.5 indicated that the change in dominating phase is at approximately at 90 mm in distance to surface (critical point). The cooling rate at this location in the sheet ingot is about 2.5 K/s, see Figure 5.8. 2.5 K/s can be perceived as a critical cooling rate. It can be seen that if the casting speed is reduced to 60 and 50 mm/s, the critical cooling rate is located at approximately 80 and 65 mm in distance to surface, respectively, Figure 5.9. If the casting speed is lowered to 40 mm/s, the cooling rate is 2.5 K/s at the surface of the ingot. However, the casting speed will affect other factors than the cooling rate. The effect of reduced cooling rate by reducing casting speed can therefore not be interpreted isolated.

82

Reducing the casting speed will decrease the cooling rate, but this will in turn will reduce the temperature gradient. Aliravci reported that the fraction of Al_mFe decreased if the temperature gradient was increased [23]. To achieve the same fraction of Al_mFe, the solidification velocity needed to be increased (NGR AA1050). To reduce the fraction of Al_mFe in the present alloy, it can be worth to studying the effect of increased temperature gradient, e.g. by increasing the temperature of the melt.

There is approximately 10 wt% Al_mFe at 134.7 mm in distance to surface, where the cooling rate is roughly 1.2 K/s. Both at the critical point and locations towards the center of ingot, the cooling rate is at a significantly lower level than what is expected that Al_mFe forms at. This implies that there are other factors which have big impact on the phase selection and enables Al_mFe to form at very low cooling rate, hence, plays a crucial role in the formation of Fir-tree structure. This will be discussed in in next sub section. The presence of Al_3Fe in the subsurface region, can be explained by the air gap between the solidified aluminium and the mould, which reduces the cooling rate, see Section 2.1.2.
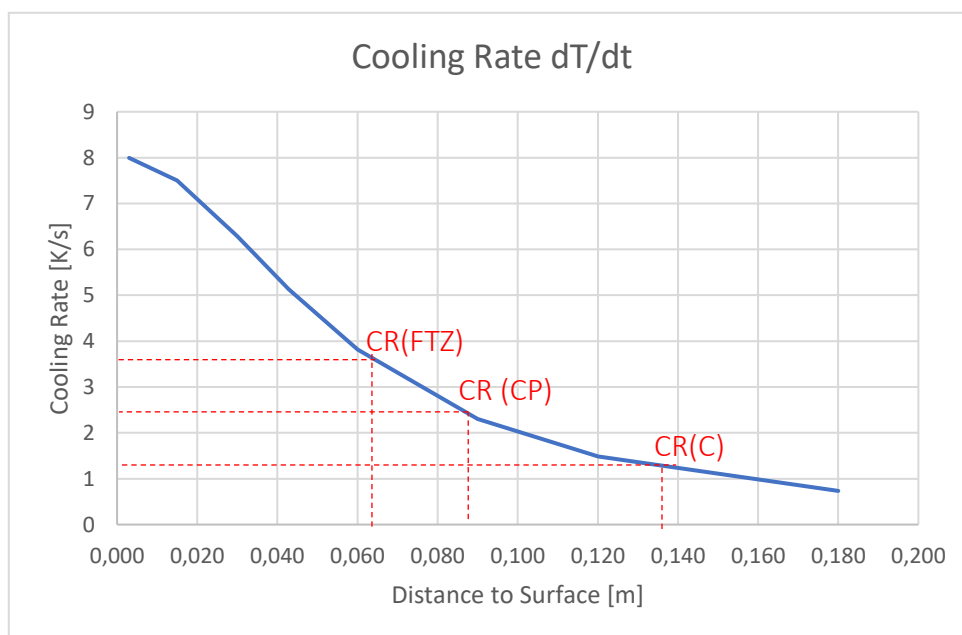
Figure 5.8: Cooling Rate (CR) as a function of distance to surface. CR for the measured Fir-Tree Zone (FTZ), Critical Point (CP) and Center (C) is marked.
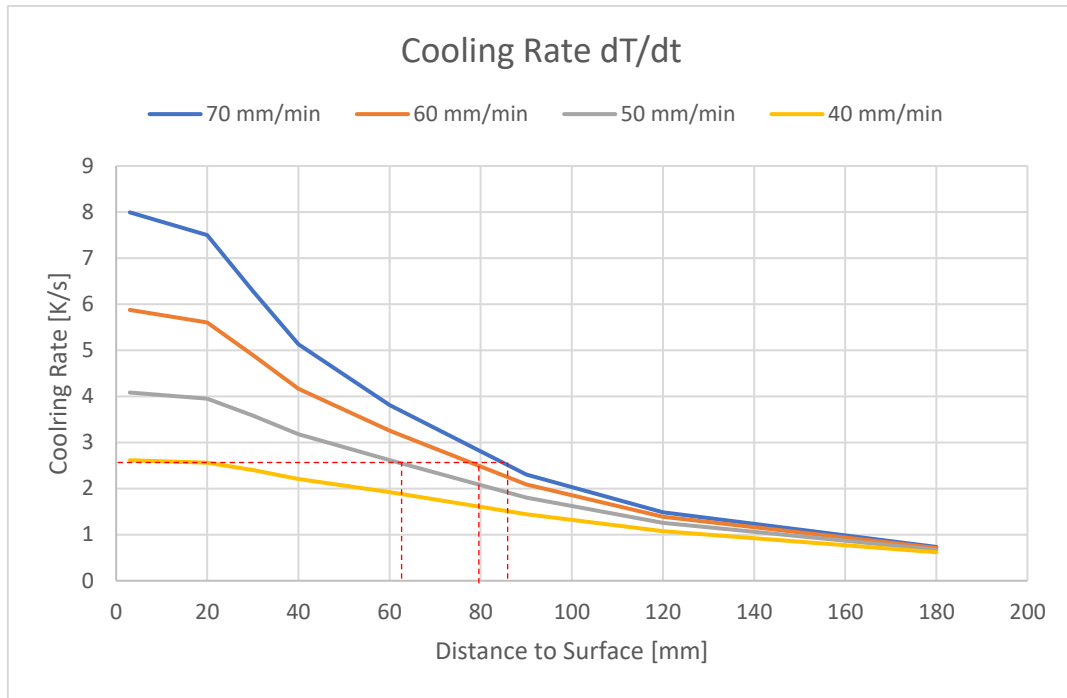
Figure 5.9: Shows the effect of casting speed on the cooling rate as a function of distance to surface. The location for the critical cooling rate at different casting speeds is marked.

5.7.2   Chemical Composition

In the present results, Al_mFe was identified at locations with much lower cooling rates than reported critical cooling rates from other researchers. Though it has been discussed that a possible solution can be to lower the casting speed, this is not a wanted solution as it will lower the productivity in the casting house. In addition, the existence of Al_mFe in low cooling rate-regions, suggest that there are other factors, such as chemical composition, that plays an even more crucial role than the cooling rate for Fir-tree structure formation. Other studies have also reported that Al_mFe can form at low cooling rates/low solidification velocities when the chemical compositions of alloy are changed [26]. The effect of impurities has then been discussed as the reason.

As presented in Section 2.3.2, Brusethaug et al. reported that the Fe/Si ratio influences the formation and width of the Fir-tree structure. In the study, the results showed that a Fe/Si ratio of 2 gave the widest Fir-tree structure and should therefore be avoided. They recommended to increase the ratio to 3 to prevent formation of Fir-tree structure. The Fe/Si ratio in the present material is 3.1 and should therefore not be the main reason for the formation. On the other hand, Allen et al. reported that the presence of Si in grain refined alloys will promote formation of Al_mFe in 1xxx Al alloys [26]. Aliravci suggested that the level of Si should be below 0.07 wt% to avoid formation of Al_mFe (AA1050) [23]. In the present material, the level of Si was 0.0919 wt% (AA5005).

The impurity level of V will also influence the formation of Al_mFe phase, hence the formation of Fir-tree structure. Allen et al. reported that in 1xxx Al alloys, typical levels of V (10-100 ppm) will promote Al_mFe phase [26]. Zhang et al. also showed that increased level of V, increased the fraction of Al_mFe formed at positions with lower cooling rates [13]. Consequently, the level of V in the present alloy (AA5005), should be kept at a minimum. Another approach to prevent formation of Fir-tree structure, can be to increase the level of Ni. This impurity element has been reported by Zhang et al. to increase the fraction of Al_3Fe at higher cooling rates. It should be mentioned, that it has only been succeeded to find one study who reported this relationship.

6   Conclusion

Iron bearing particles across a part of the cross-section of a sheet ingot of AA5005 with Fir-tree structure defect have been studied. Different techniques and approaches to characterize the iron bearing particles have been tested and compared. The present work can be divided into two parts:

I)   Finding reliable techniques to identify the iron bearing particles which causes the Fir-tree structure defect

II) Quantitative characterization of iron bearing particles to study the mechanism for Fir-tree structure formation

6.1   Techniques to Characterize Iron Bearing Particles

The morphology of the iron bearing particles was studied in plane polished samples, deep etched samples and as powder extracted from the aluminium matrix. From plane polished samples, areas of interest could quickly be observed. The powder and deep etched samples revealed more about the growth of the particles and the 3D-morphology. The particles tended to agglomerate when they were extracted from the aluminium matrix. This could make study of morphology challenging.

With EBSD and WDS, particles with characteristic morphologies could be identified. The iron bearing particles were very small, which mostly resulted in too poor EBSP quality for phase identification. When the pattern quality was satisfying, the particles could easily be identified. The small sizes of the particles were also a challenge with the WDS analyses. It was evident that the interaction volume between the electron beam and particle often was too large, which resulted in falsified quantitative analyses. To determine exact chemical composition by WDS is difficult for a large fraction of particles. Therefore, the WDS analyses need to be interpreted with caution. But it was clear that three different iron bearing particles exists in the alloy. A combination of WDS and EBSD gave a more reliable identification of iron bearing particles.

The phenol method for extracting iron bearing particles from the aluminium matrix, was for the first time carried out at the department. With the basic laboratory equipment in the lab, the experimental procedures were developed and documented. The iron bearing particles were successfully extracted, and a quantitative analysis of the fraction of different particles could be performed by using XRD and the Rietveld refinement method.

6.2 Formation of Fir-tree Structure in DC Ingot

The grain size increased with increasing distance to surface of the ingot. This indicated that the cooling rate decreases towards the center of the ingot during solidification.

Close to the surface, where the cooling rate is the highest, the dominating particle had a skeletal morphology in plane polished sample. The skeletal morphology dominated in the ingot until 5.6 cm in distance to the surface of the ingot. With further increasing distance from surface until 10.4 cm, it was a mixture of both skeletal and needle-like particles. At 12.0-13.6 cm in distance to surface, where the cooling rate is the lowest, the dominating morphology of particles was needle-like.

By EBSD and WDS, the particles with characteristic morphologies was identified. The skeletal particles showed to be mainly the Al_mFe phase. The 3D morphology of Al_mFe was dendritic. The phase grew as thin flakes where it was possible and frequently branched to adjust to the interdendritic channels. The tips were usually semi-spherical. It could be observed that a few typical Al_mFe particles have four main branches starting from what appeared like a nucleation site. The particles with needle-like morphology proved to be Al_3Fe. Al_3Fe could also appear with plate and stacked plate-like morphology. The 3D-morphology of the phase was either bundles of needles, rods and flakes or plates. The plates consisted of densely packed rods in one direction, probably parallel to the heat flow. Al_6Fe were only identified a few times and appeared with both skeletal-like and plate-like morphology. The 3D-morphology of Al_6Fe was not determined.

The phase distribution of iron bearing particles achieved by powder XRD measurements corresponded well with observations from morphology studies, EBSD and WDS analyses. Close to the surface, Al_mFe dominated with approximately 90 wt%, the remaining was Al_3Fe. At 135 mm in distance to surface, the phase distribution was completely different: 89 wt% Al_3Fe, 10 wt% Al_mFe and 1 wt% Al_6Fe. Al_6Fe did only exist as a minority phase at some locations towards the center of the ingot. Between 65 and 79 mm in mean distance to surface, there was a rapid change in dominating phase from Al_mFe to Al_3Fe. The reason for Fir-tree structure, was supposed to be the sudden change in dominating phase.

The findings are in accordance with the theoretical background: According to cooling rate calculations for the present material, the cooling rate close to the surface is approximately 8 K/s. Earlier studies have reported formation of Al_mFe and Fir-tree structure in AA5005 at approximately this cooling rate. The relatively high fraction of Al_mFe in low cooling rates regions have been discussed to be caused by trace elements which either promotes formation of Al_mFe or supress formation of Al_3Fe.

7   Further work

In future characterizations of the Fir-tree structure, it is recommended to use the phenol method to extract the iron bearing particles from the aluminium matrix. From the present results, this method does not only seem to be the most reliable technique for identification, but also to provide the most useful information for Fir-tree structure characterization.

For this alloy, the following is suggested to avoid formation of Fir-tree structure:

- To decrease the cooling rate to decrease the fraction of Al_mFe. This can be achieved by reducing the casting speed.
- To increase the temperature gradient by increasing the temperature of the melt. If the temperature gradient is increased, higher solidification velocity to form the same fraction of Al_mFe is required.
- Lower the level of the trace element V in the alloy, since V promotes Al_mFe.
- Decrease the content of Si, since the presence of Si in grain refined alloys promotes Al_mFe.
- Increase the level of trace element which promotes Al_3Fe, e.g. Ni.

In general, further research on Fir-tree structure should study the effect of trace elements and temperature gradient on eutectic phase selection.

8 References

1. *OIM Data Collection 7.2 Manual.*
2. *OIM Analysis 5.3 Manual*.
3. Ltd, V. *X-RAY DIFFRACTION.* [cited 2018 22.04]; Available from: http://www.veqter.co.uk/residual-stress-measurement/x-ray-diffraction.
4. Li, G., *Effect of trace elemnts V and Ni on Fe intermetallic phases formation and distribution in DC cast 5xxx series Al ingots*. 2012, University of Québec, Chicoutimi.
5. Darrell, H. and J. Goodge. *Wavelength-Dispersive X-Ray Spectroscopy (WDS)*. [cited 2018 23.04]; Available from: https://serc.carleton.edu/research_education/geochemsheets/wds.html.
6. Brusethaug, S.P., D. and O. Vorren, *The Effect of Process Paramters on the Fir-Tree Structure in DC-Cast Rolling Ingots*, in *8th International Light Metals Congress*. 1987: Leoben-Vienna.
7. Sabu, U. *Introduction to Solidification of Metals and Design Considerations in Casting*. 2015; Available from: https://www.slideshare.net/ummen6097/solidification?next_slideshow=3.
8. Westengen, H., *Structure Inhomogeneities in Direct Chill Cast Sheet Ingots of Commercial Purity Aluminum.* Aluminium : Fachzeitschrift der Aluminiumindustrie, 1982. **58**(7): p. 398.
9. Porter, D.A., K.E. Easterling, and M.Y. Sherif, *Phase Transformations in Metals and Alloys*. 3rd ed. ed. 2009, Boca Raton, Fla: CRC Press.
10. Blackwell, J.H. and J.R. Ockendon, *Exact solution of a stefan problem relevant to continuous casting.* International Journal of Heat and Mass Transfer, 1982. **25**(7): p. 1059-1060.
11. Otani, T., et al., *Fir Tree Structure of 1000- and 5000-Series Aluminum Alloy Sheet Ingots*, in *Light Metals*, G.M. Bell, Editor. 1981. p. 452-459.
12. Aliravci, C.A., J.E. Gruzleski, and M.O. Pekgüleryüz, *A Thermodynamic Study of Metastable Al-Fe Phase Formation in Direct Chill (DC)-Cast Aluminum Alloy Ingots*, in *Light Metals*, B. Welch, Editor. 1998. p. 466-474.
13. Zhang, Z., G. Li, and X.G. Chen, *Effect of nickel and vanadium on iron bearing intermetallic phases in AA 5657 simulated DC castings.* Materials Science and Technology, 2014. **30**(8): p. 951-961.
14. Li, Y.J. and L. Arnberg, *Solidification structures and phase selection of iron-bearing eutectic particles in a DC-cast AA5182 alloy.* Acta Materialia, 2004. **52**(9): p. 2673-2681.
15. Schwartz, A.J., et al., *Electron Backscatter Diffraction in Materials Science*. 2009, Boston, MA: Springer US: Boston, MA.
16. Solberg, J.K. and m. Norges teknisk-naturvitenskapelige universitet Institutt for, *Teknologiske metaller og legeringer*. 2014, Trondheim: Institutt for materialteknologi, Norges teknisk-naturvitenskapelige universitet.
17. Dave, N.M. *Solidification*. 2016 10.10.17; Available from: https://www.slideshare.net/NamanDave/solidification-59517471?next_slideshow=2.
18. Totten, G.E. and D.S. MacKenzie, *Handbook of aluminum : Vol. 1 : Physical metallurgy and processes*. Vol. Vol. 1. 2003, New York: Marcel Dekker.
19. Grandfield, J., D.G. Eskin, and I. Bainbridge, *Direct-Chill Casting of Light Alloys : Science and Technology*. Direct-Chill Casting of Light Alloys. 2013, Hoboken: Wiley.

20. Materia, T. *Direct-Chill Casting*. 2016; Available from: http://www.totalmateria.com/page.aspx?ID=CheckArticle&site=ktn&LN=NO&NM=384.

21. Emley, E.F., *Continuous Casting of Aluminium.* International Metals Reviews, 1976. **21**(1): p. 75-115.

22. Kurz, W. and D.J. Fisher, *Fundamentals of solidification*. 4th rev. ed. ed. 1998, Uetikon-Zuerich: Trans Tech Publications.

23. Aliravci, A., *Kinetics, Thermodynamics and Mechanism of Metastable Al-AlmFe Phase and Fir-Tree Zone Formation in DC-Cast Al-Fe-Si alloy Ingots* in *Mining, Metals and Materials Engineering*. 2006, Mc Gill University: Ottawa.

24. Zhang, Z., et al., *Identification and Distribution of Fe Intermetallic Phases in AA5657 DC Cast Ingots*, in *13th International Conference on Aluminum Alloys*. 2012: Pittsburgh, Pennsylvania.

25. Chen, X.G., *Growth Mechanisms of Intermetallic Phases in DC Cast AA1xxx Alloys*, in *Light Metals*, B. Welch, Editor. 1998. p. 460-465.

26. Allen, C.M., et al., *Intermetallic phase selection in 1XXX Al alloys.* Progress in Materials Science, 1998. **43**(2): p. 89-170.

27. Liu, K., X. Cao, and X.-G. Chen, *A New Iron-Rich Intermetallic-Al m Fe Phase in Al-4.6Cu-0.5Fe Cast Alloy.* Metallurgical and Materials Transactions A, 2012. **43**(4): p. 1097-1101.

28. Maitland, T. and S. Sitzman, *Electron Backscatter Diffraction (EBSD) Technique and Materials Characterization Examples*, in *Scanning Microscopy for Nanotechnology: Techniques and Applications*, W. Weilie Zhou and Z.L. Wang, Editors. 2007, Springer New York: New York, NY.

29. Hjelen, J., *Scanning elektron-mikroskopi*. 1986, Trondheim: Sintef.

30. Instruments, O. *EBSD Explained From data acquisition to advanced analysis*. 2015 [cited 2018 23.02]; Available from: https://www.oxford-instruments.com/products/microanalysis/ebsd.

31. Wright, S.I., et al., *Introduction and comparison of new EBSD post-processing methodologies.* Ultramicroscopy, 2015. **159**: p. 81-94.

32. Hjelen, J., *Averaging*. 2018.

33. Lawes, G., *Scanning Electron Microscopy and X-Ray Microanalysis*. 1987, London: John Wiley & Sons.

34. Scott, V.D., G. Love, and S.J.B. Reed, *Quantitative Electron-Probe Microanalysis*. 2 ed. Ellis Horwoos Series in Physics and its Applications, ed. M.J. Cooper and J.W. Mason. 1995.

35. Gupta, A.K., P.H. Marois, and D.J. Lloyd, *Review of the techniques for the extraction of second-phase particles from aluminum alloys.* Materials Characterization, 1996. **37**(2-3): p. 61-80.

36. Simensen, C., P. Fartum, and A. Andersen, *Analysis of intermetallic particles in aluminium by dissolution of the sample in butanol.* Fresenius' Zeitschrift für analytische Chemie, 1984. **319**(3): p. 286-292.

37. Abou Khatwa, M.K. and D.V. Malakhov, *On the thermodynamic stability of intermetallic phases in the AA6111 aluminum alloy.* Calphad, 2006. **30**(2): p. 159-170.

38. Sato, K. and I. Izumi, *Chemical Isolation of Intermetallic Compounds from Aluminium And Its Alloys.* BUNSEKI KAGAKU, 1984. **33**(11): p. E495-E498.

39.	Skinner, T.D. and M. Vickers. *X-ray Diffraction Techniques*. 2007 [cited 2018 22.04]; Available from: https://www.doitpoms.ac.uk/tlplib/xray-diffraction/index.php.

40.	Mittemeijer, E.J. and U. Welzel, *Modern diffraction methods*. 2013, Weinheim: Wiley-VCH.

41.	Skjerpe, P., *Structure of AlmFe.* Acta Crystallographica Section B, 1988. **44**(5): p. 480-486.

42.	Gjønnes, J., et al., *Structure Model for the Phase Al m Fe Derived from Three-Dimensional Electron Diffraction Intensity Data Collected by a Precession Technique. Comparison with Convergent-Beam Diffraction.* Acta Crystallographica Section A, 1998. **54**(3): p. 306-319.

43.	Solli, I., *Characterizaation of Fir-Tree Structure in Al-Mg Alloys*, in *Material Science and Enigneering*. 2017, NTNU.

44.	Raanes, M.P., *Personal Communication*. 2018.

45.	Koten, G.v., et al., *Versatility in phenolate bonding in organoaluminum complexes containing Mono- and Bis(ortho)-chelating phenolate ligands. X-ray structures of Al{OC6H2(CH2NMe2)2-2,6-Me-4}3, Al(Me)2{OC6H2(CH2NMe2-2,6-Me-4} N-AlMe3, and Al(Me)2{OC6H2(CH2NMe2)2-2,6-Me-4} N-AlMe3O-AlMe3.* Organometallics, 1995. **14**(10): p. 4483-7333.

46.	Villars, P., L.D. Calvert, and W.B. Pearson, *Pearson's handbook of crystallographic data for intermetallic phases : Vol. 1*. Vol. Vol. 1. 1985, Metals Park: American Society for Metals.

Appendix 1: Crystallographic Information for the Iron Bearing Particles

Table 1: Atomic positions for the Al_mFe phase. The study did not succeed to refine occupation numbers [42].

Atoms	x	y	z
Fe_1	0.1838	0.1838	0.5792
Fe_2	0.1740	0.1740	0.2750
Fe_3 / Al	0.183	0.183	0.8716
Al_1	0.337	0.031	0.0729
Al_2	0.295	0.044	0.3657
Al_3	0.295	0.044	0.7729
Al_4	0.00000	0.000	0.0748
Al_5	0.215	0.215	0.9793
Al_6	0.233	0.233	0.173
Al_8	0.500	0.197	0.00000
Al_9	0.000	0.000	0.3488
Al_{10}	0.000	0.000	0.211
Al_{11}	0.000	0.000	0.50000

Table 2: Atomic positions for the Al_6Fe phase with space group Cmc2 [46].

Atoms	Symmetry	x	y	z	Occupancy
Al_1	m	0.0	0.1450	0.1050	1.00
Al_2	m	0.0	0.1210	0.3970	1.00
Al_3	l	0.3255	0.0171	0.0000	1.00
Al_4	l	0.3182	0.2872	0.2610	1.00
Fe	m	0.0	0.4612	0.2500	1.00

Table 3: Atomic positions for the Al$_3$Fe phase [46].

Atoms	Symmetry	x	y	z	Occupancy
Al$_1$	2/m	0.0	0.5	0.5	1.00
Al$_2$	2	0.0	0.2441	0.0	1.00
Al$_3$	m	0.3223	0.0	0.2778	0.70
Al$_4$	m	0.2352	0.0	0.5392	1.00
Al$_5$	m	0.0812	0.0	0.5824	1.00
Al$_6$	m	0.2317	0.0	0.9729	1.00
Al$_7$	m	0.4803	0.0	0.8277	1.00
Al$_8$	m	0.3100	0.0	0.7695	1.00
Al$_9$	m	0.0869	0.0	0.7812	1.00
Al$_{10}$	m	0.0645	0.0	0.1730	1.00
Al$_{11}$	l	0.1883	0.2164	0.1111	1.00
Al$_{12}$	l	0.3734	0.2110	0.1071	1.00
Al$_{13}$	l	0.1765	0.2168	0.3343	1.00
Al$_{14}$	l	0.4959	0.2832	0.3296	1.00
Al$_{15}$	l	0.3664	0.2238	0.4799	1.00
Fe$_1$	m	0.0865	0.0	0.3831	1.00
Fe$_2$	m	0.4018	0.0	0.6243	1.00
Fe$_3$	m	0.0907	0.0	0.9890	1.00
Fe$_4$	m	0.4001	0.0	0.9857	1.00
Fe$_5$	l	0.3188	0.2850	0.2770	1.00

Appendix 2: Simulated Diffraction Diagrams
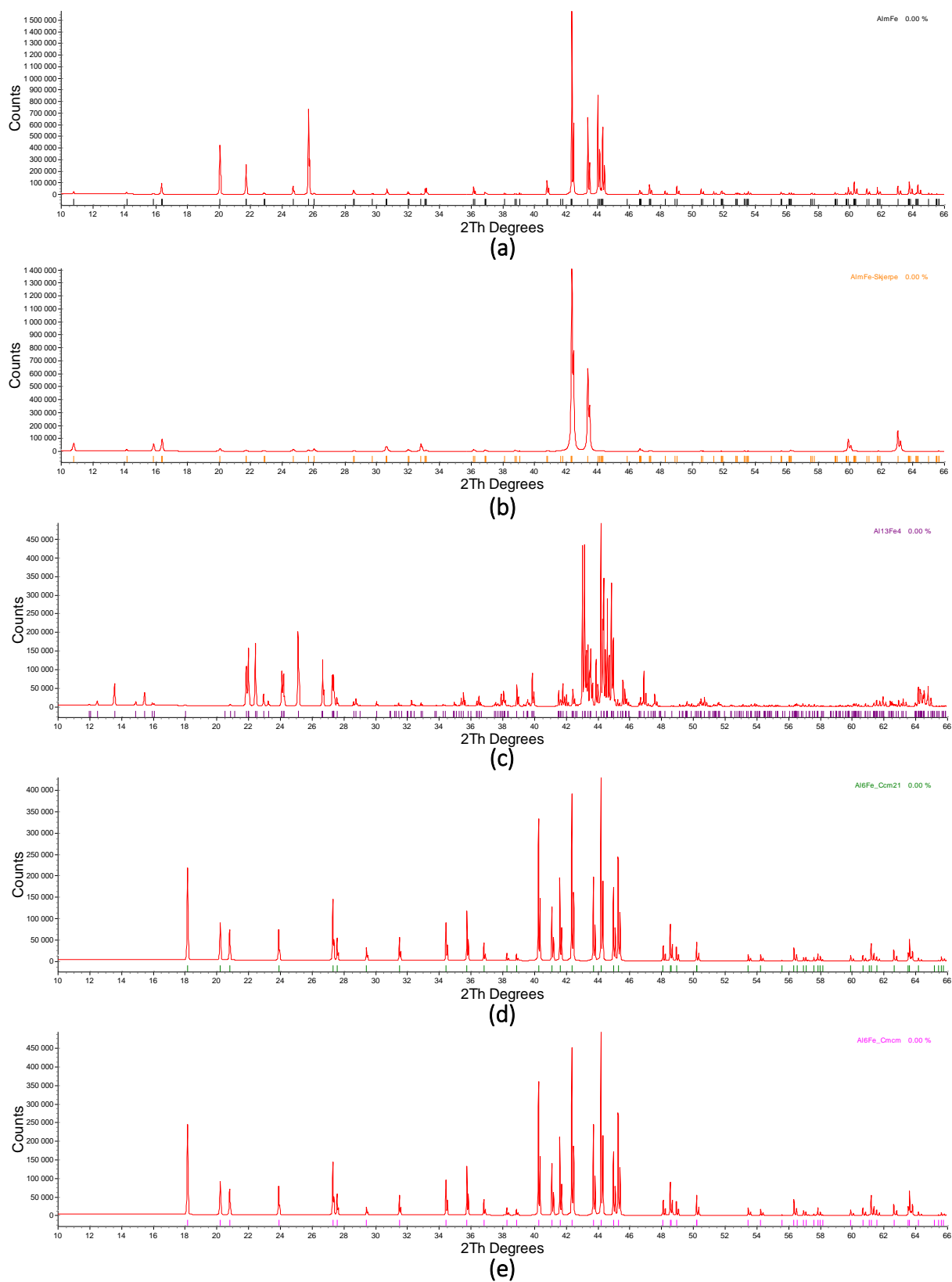
Figure 1: Simulated diffraction diagrams for (a) Al_mFe ($I\bar{4}2m$), (b) Al_mFe ($I4/mmm$), (c) Al_3Fe, (d) $Al_6Fe(Ccm2)$, (e) Al_6Fe ($Ccmm$).

Appendix 3: Low-Magnification SEM-Images

Low-magnification BSE-SEM images at three different distances to the surface: close to surface, at 10.4 cm and 13.6 cm in distance to surface, see Figure 2,3 and 4, respectively.
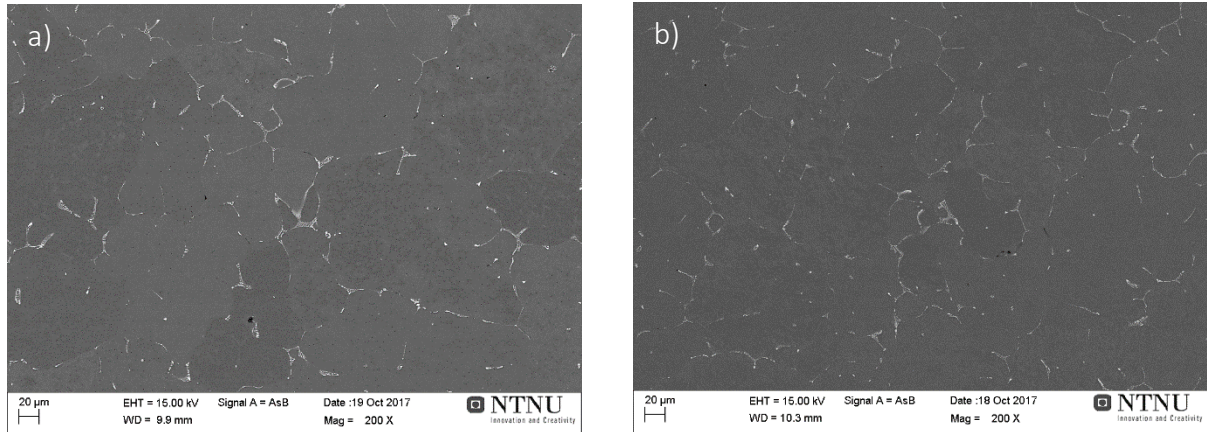
Figure 2: At the samples closest to the surface, the skeletal morphology of particles dominates a) T1, b) B1.
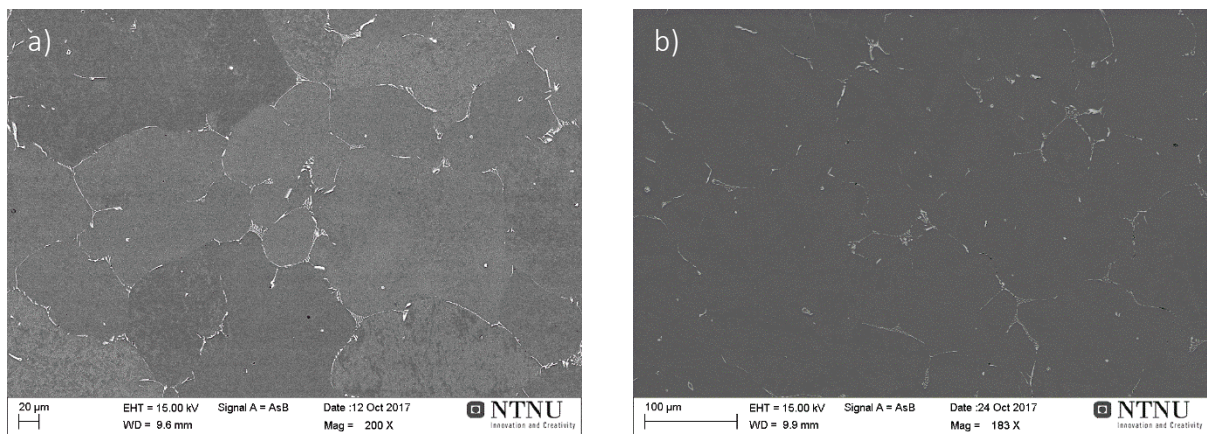
Figure 3: At the distance 10.4 cm to surface, there is a mixture of particles with skeletal and needle-like morphology a) T7, b) B7.
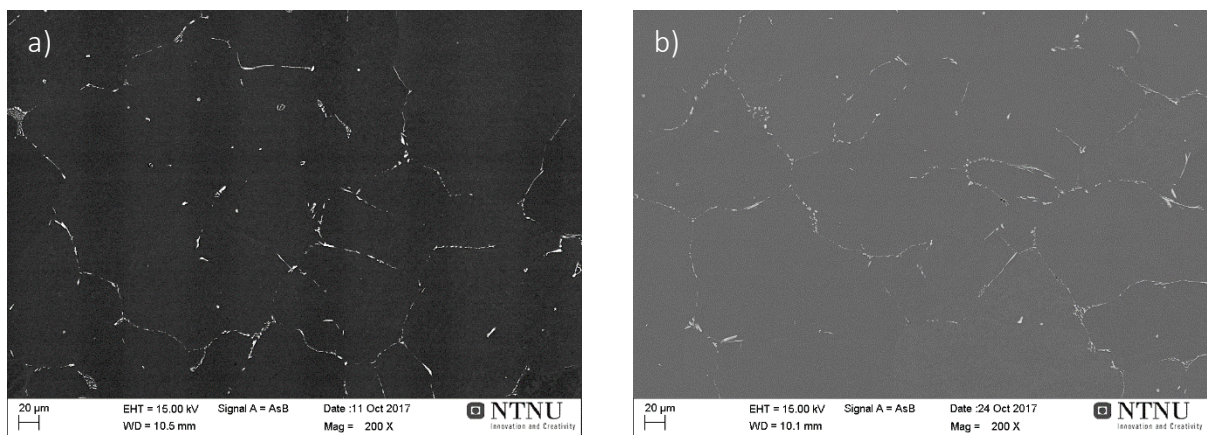
Figure 4: At the sample closest to the center of the ingot, particles with needle-like morphology dominates, but particles with skeletal morphology can also be observed a) T9, b) B9.

Appendix 4: Morphology Study in Light Microscope

The morphology of the iron bearing particles changed from the surface and towards the center of the ingot. Figure 5-13 and Figure 14-22 show in detail the change in particle's morphology for the bottom and top slice, respectively. For each sample the particle morphologies are imaged at 500x and 1000x.

Samples from Bottom Slice
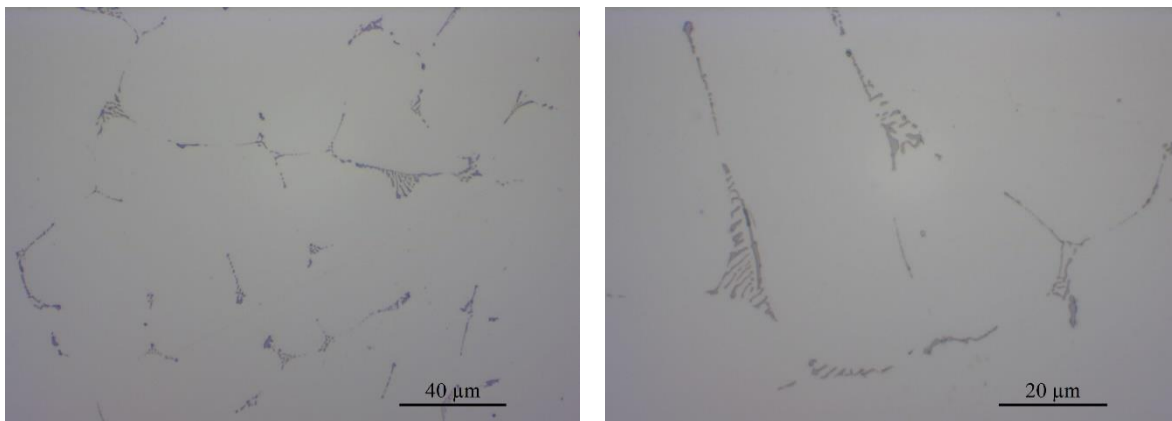
Figure 5: The main morphology of the intermetallic phases is skeletal in sample B1.
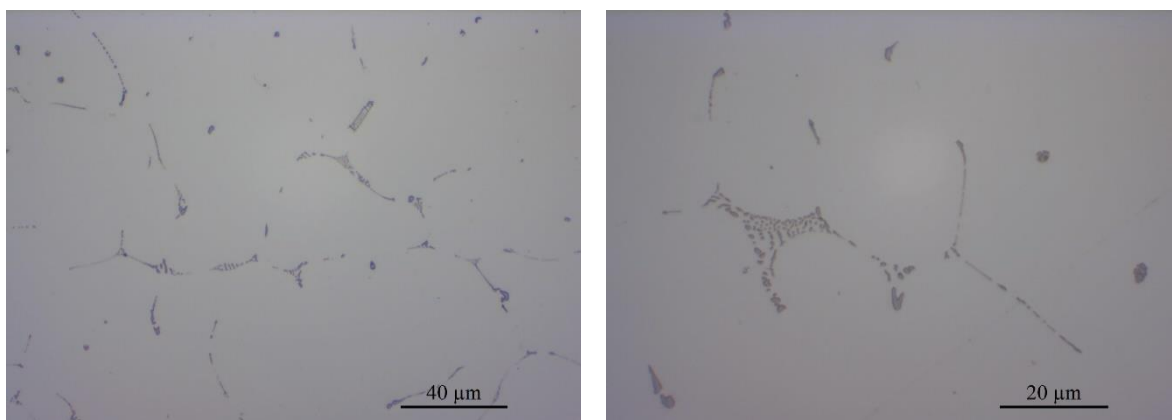
Figure 6: Mainly skeletal morphology of intermetallic phases in sample B2.
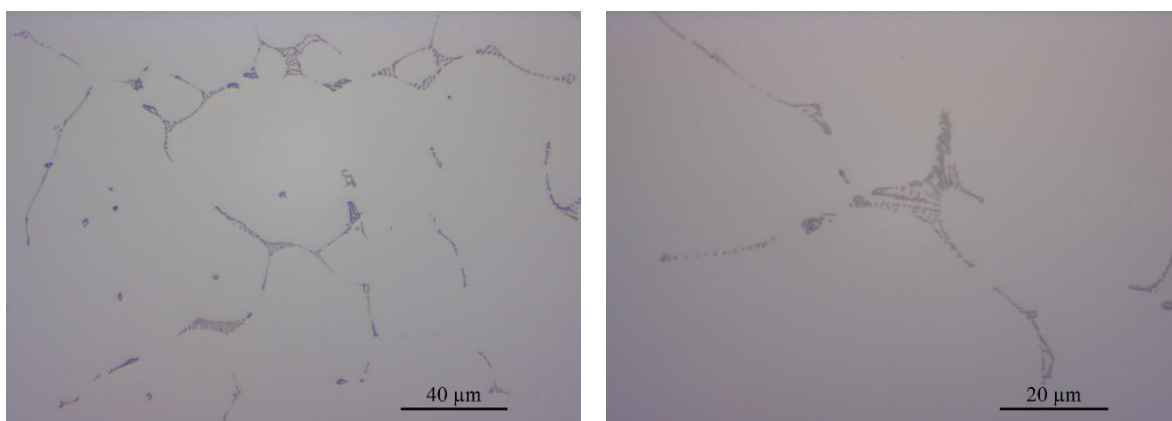
Figure 7: Mainly skeletal morphology of intermetallic phases in sample B3.
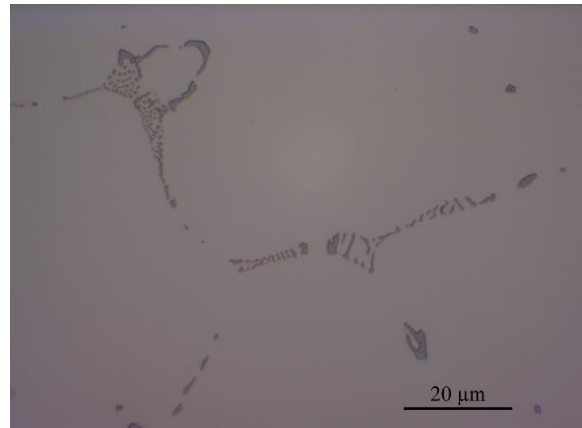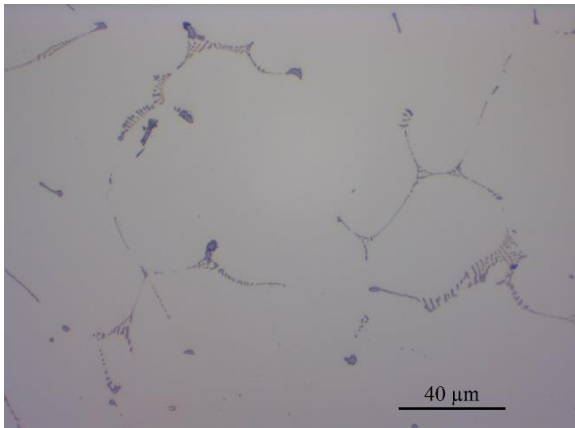
Figure 8: Mainly skeletal particles in sample B4.
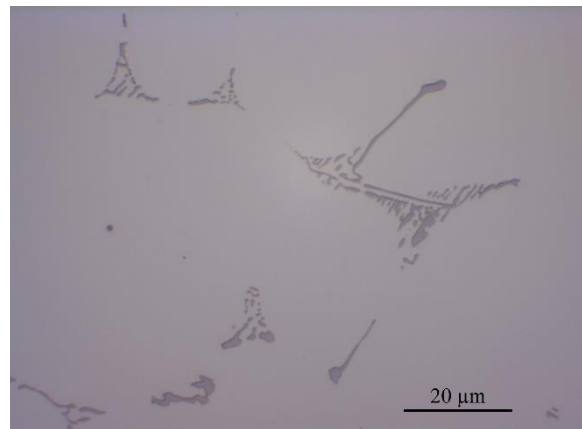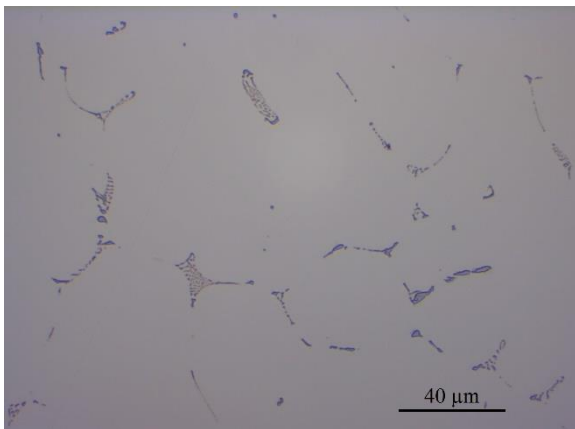
Figure 9: Mainly skeletal particles, but also some particles with needle-like morphology in sample B5.
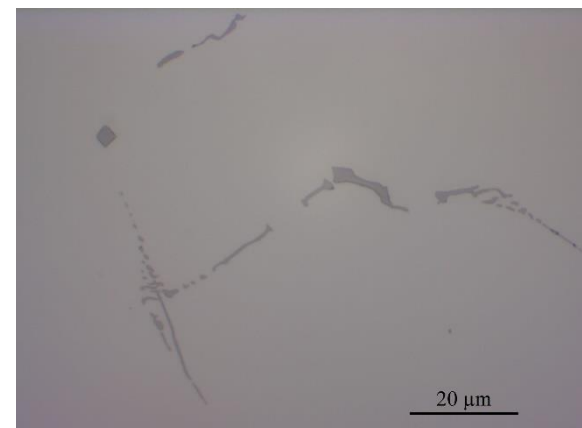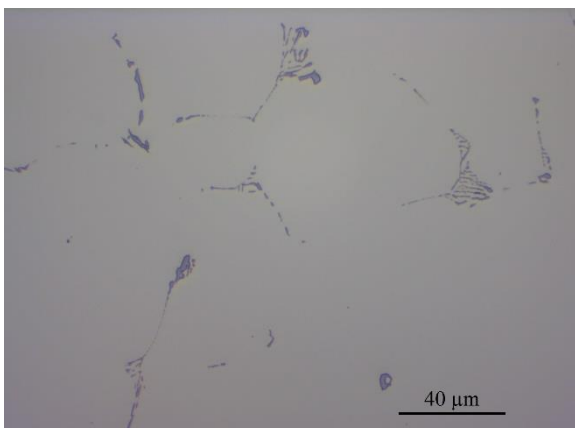
Figure 10: Mixture of particles with skeletal and needle-like morphology in sample B6.
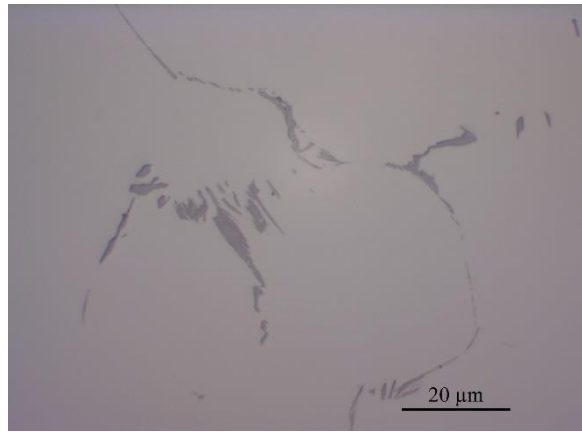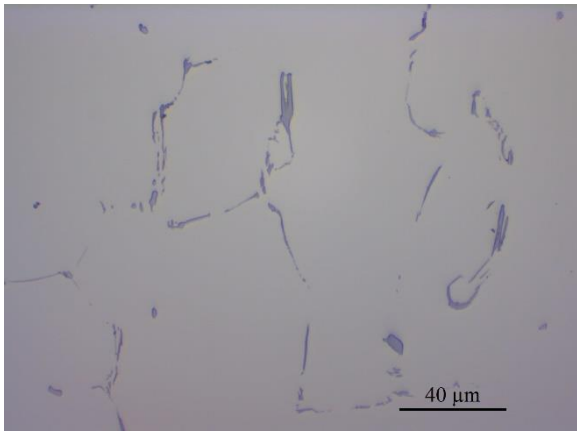
Figure 11: Mainly particles with needle-like morphology in sample B7. Notice the change in morphology compared to the sample closer to the surface, e.g. sample B4.
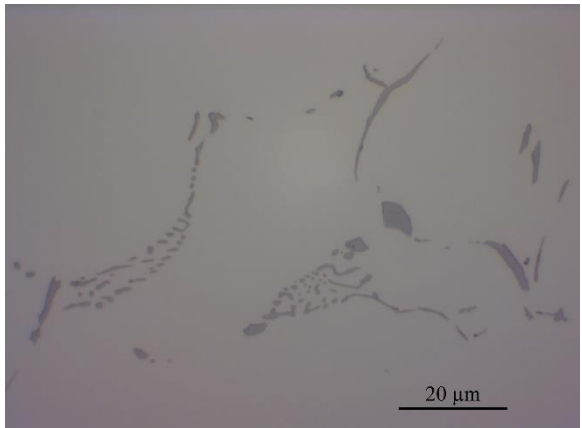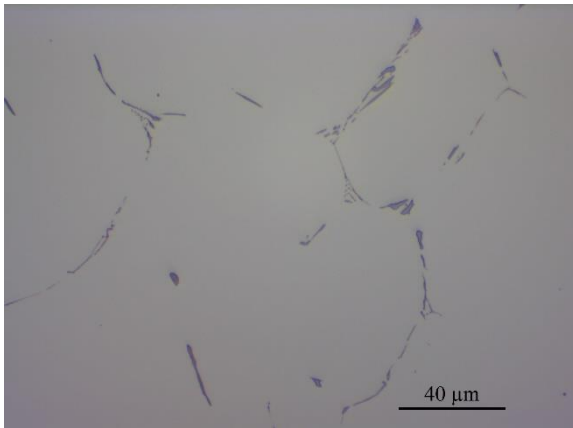
Figure 12: Mainly needle-like particles in sample B8.
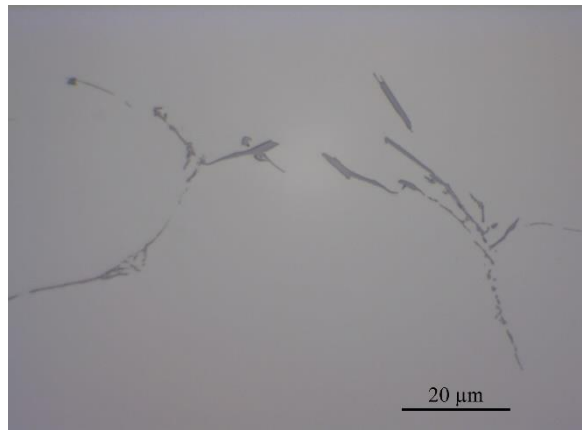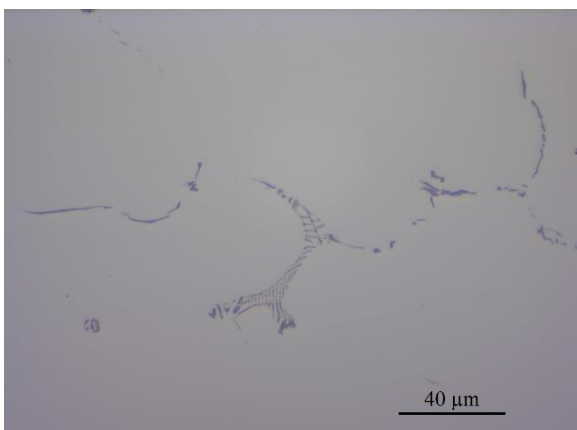
Figure 13: Mainly particles with needle-like morphology in sample B9, but skeletal particles can still be observed. Notice the increase in size of intermetallic phases, compared to e.g. sample B1.

Samples from Top Slice
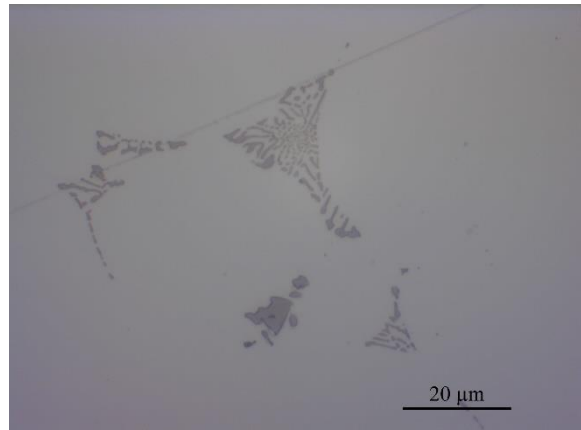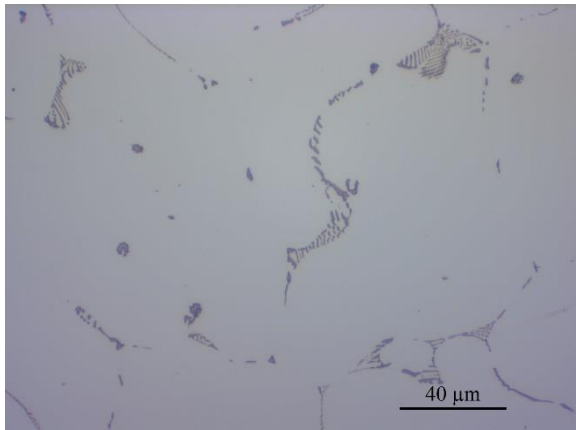
Figure 14: Mainly skeletal particles in sample T1.
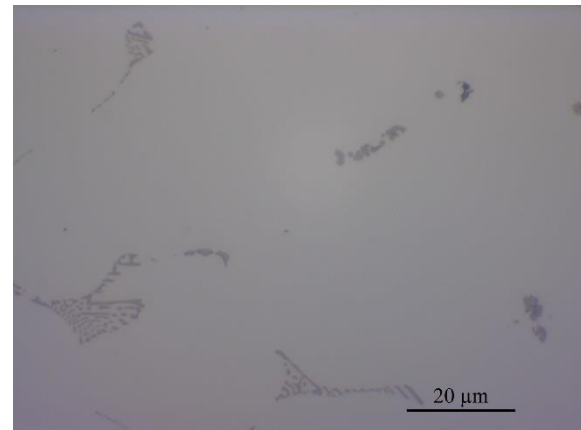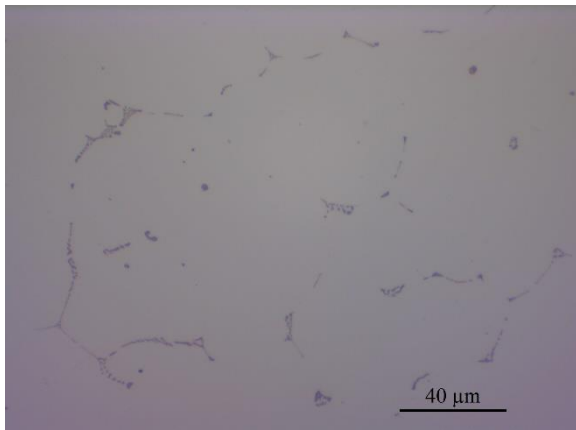
Figure 15: Mainly particles with skeletal morphology in sample T2.
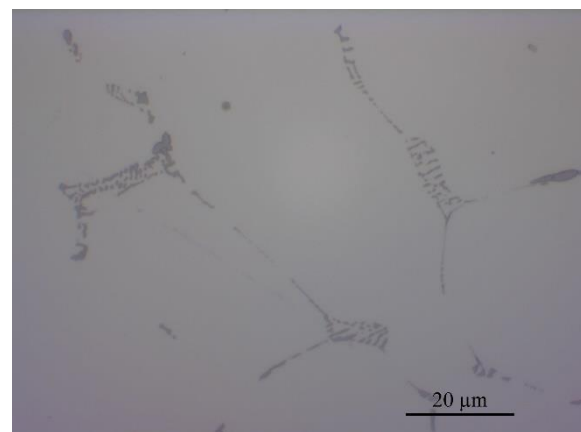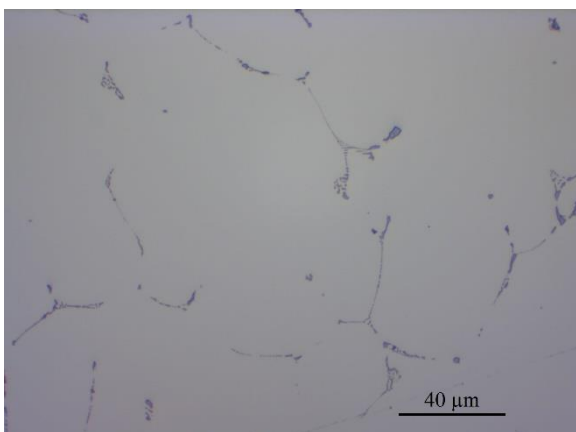
Figure 16: Mainly particles with skeletal morphology in sample T3.
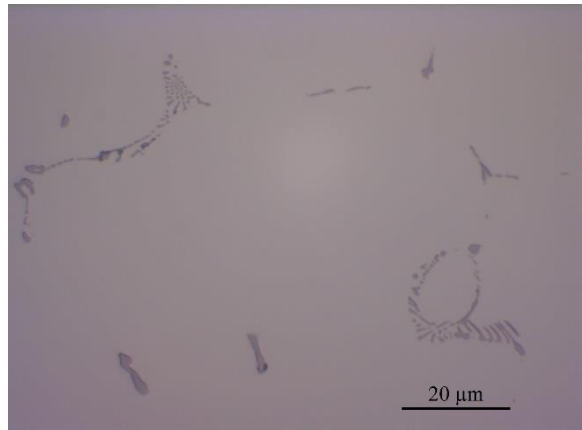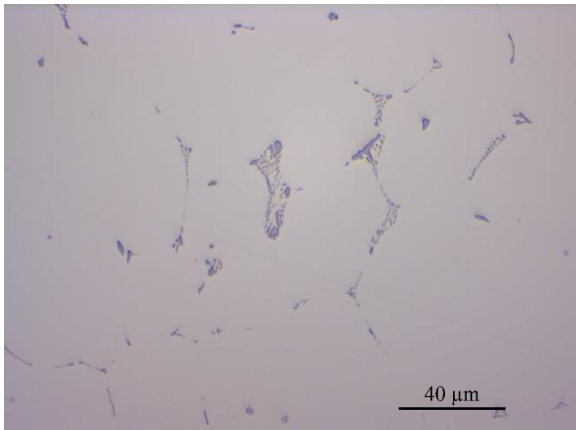
Figure 17: Mainly particles with skeletal morphology in sample T4, but a few particles with needle-like morphology can be observed.
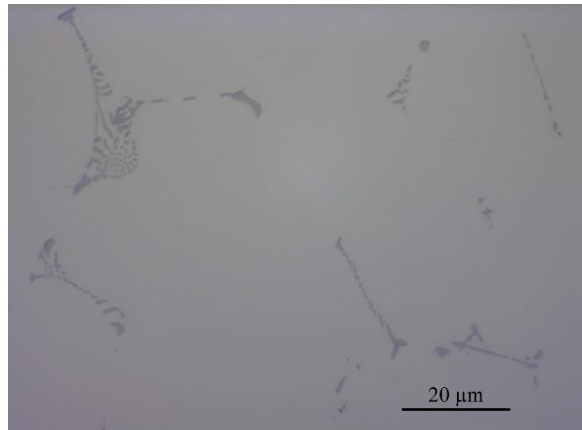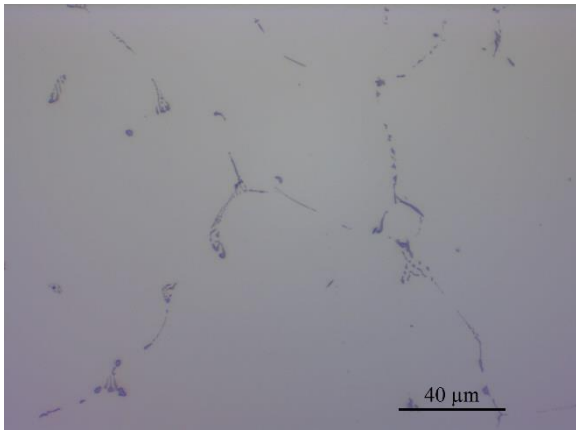
Figure 18: A mixture of skeletal and needle-like particles in sample T5.
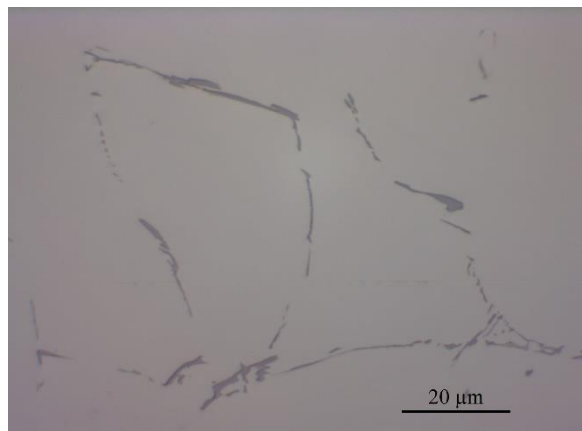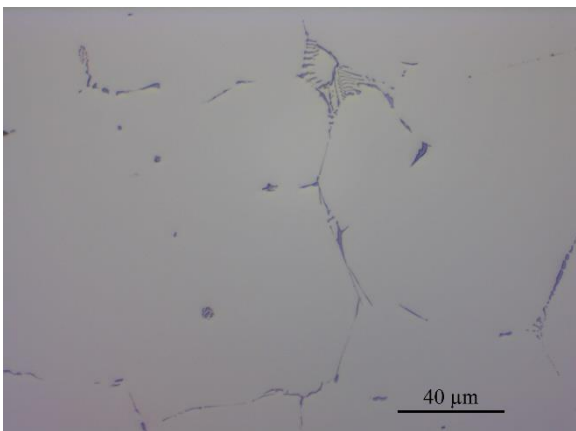
Figure 19: Mixture of both skeletal and needle-like particles in sample T6.
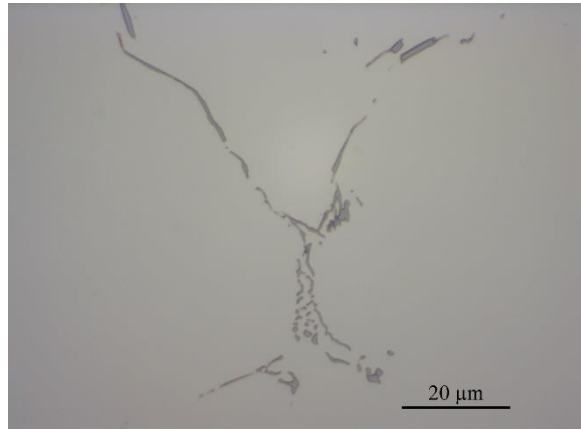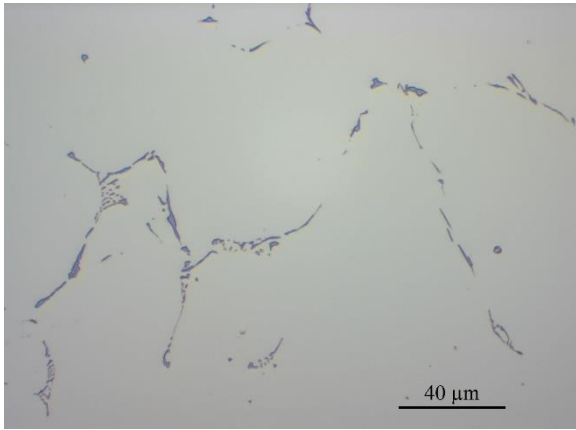
Figure 20: Mainly particles with needle-like morphology, but some particles with skeletal morphology can be observed in sample T7.
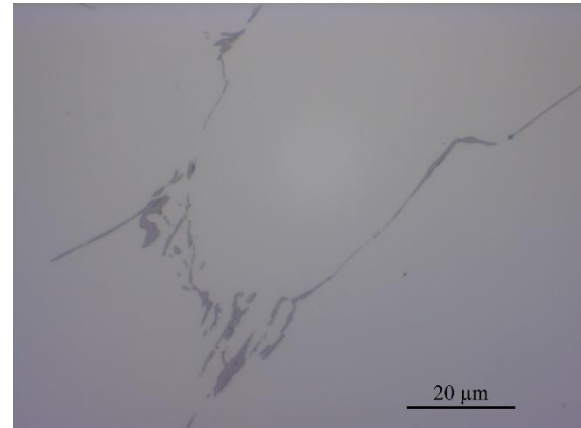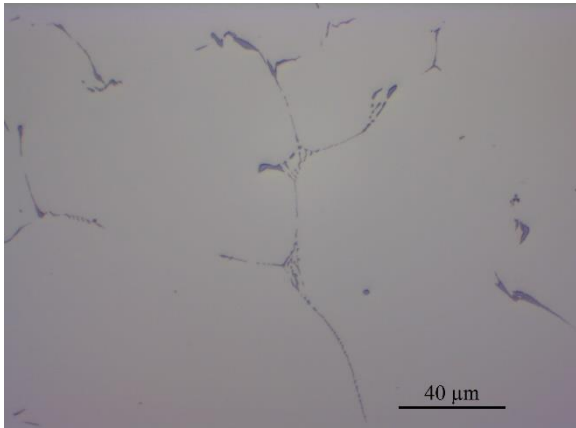
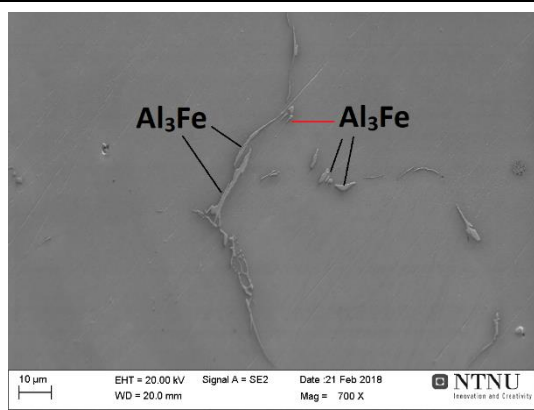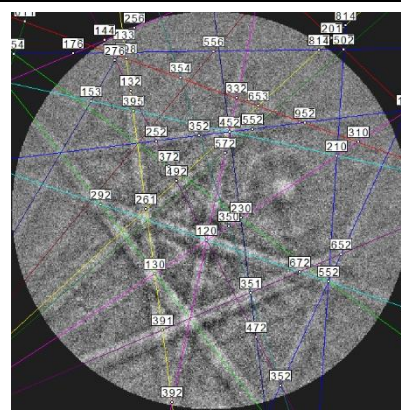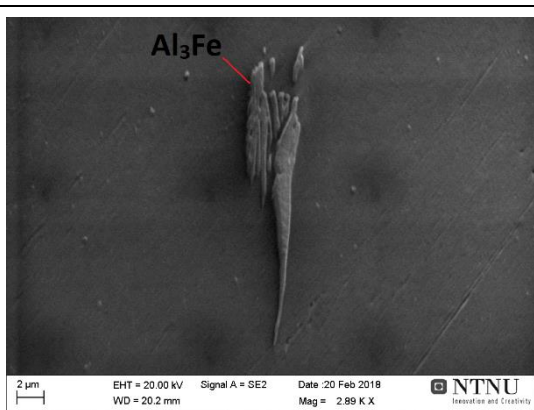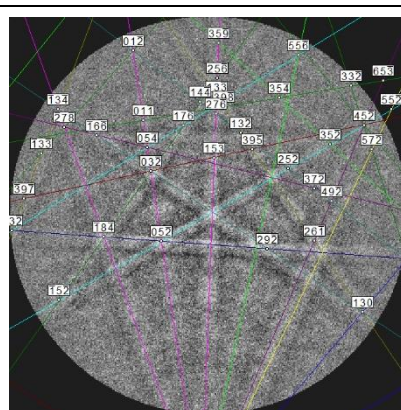*Figure 21: Mainly needle-like particles in sample T8.*
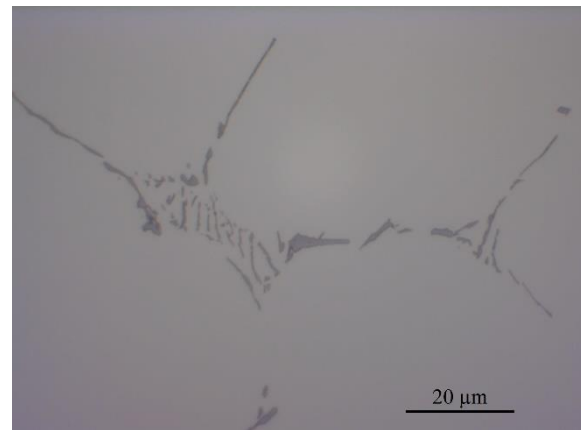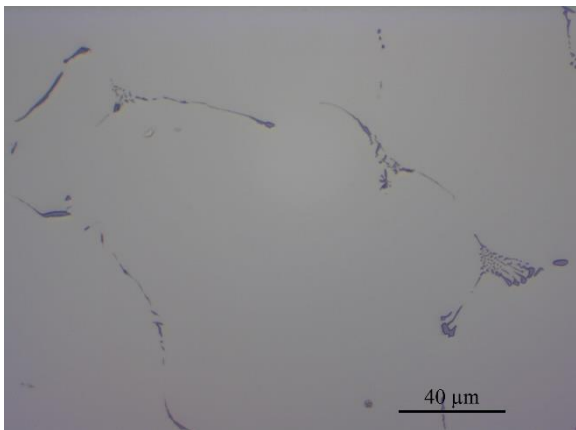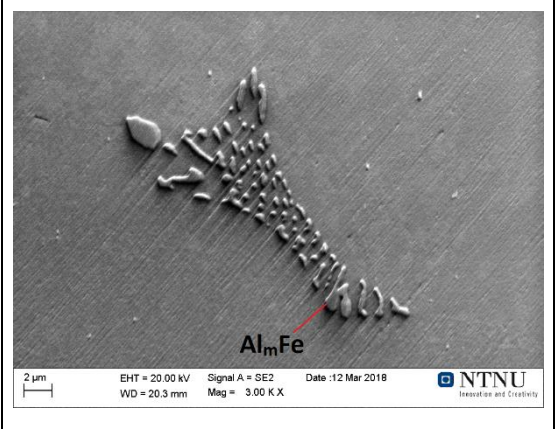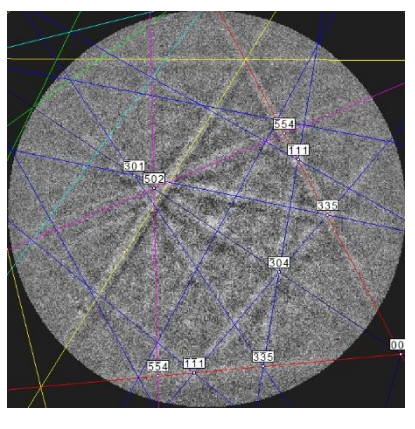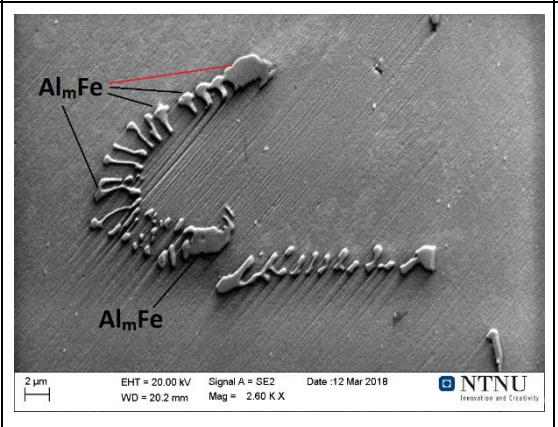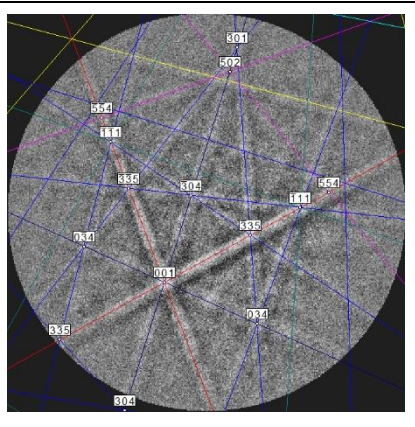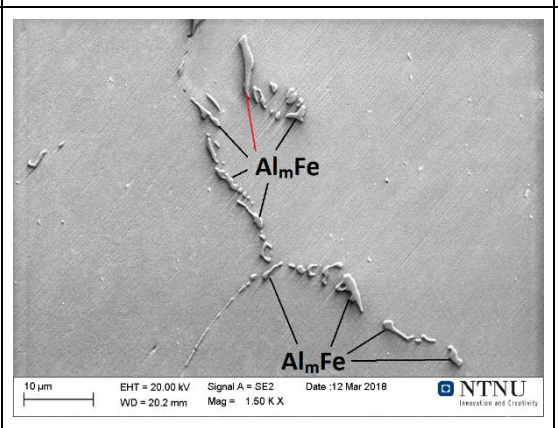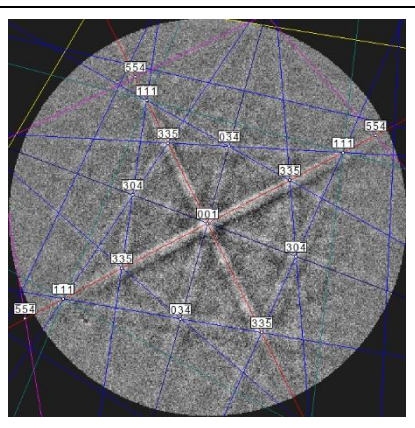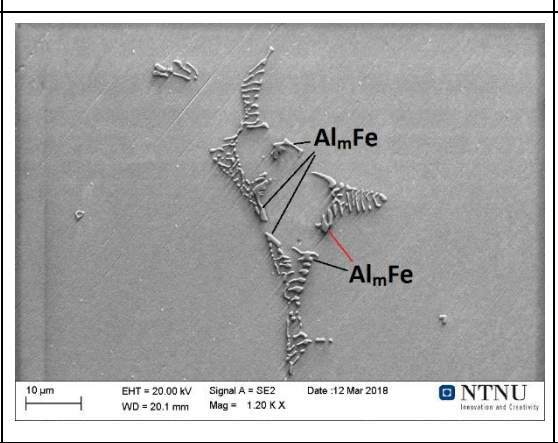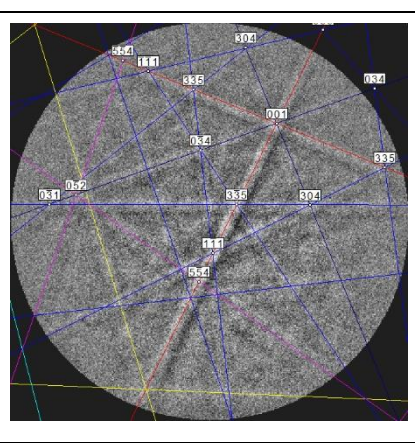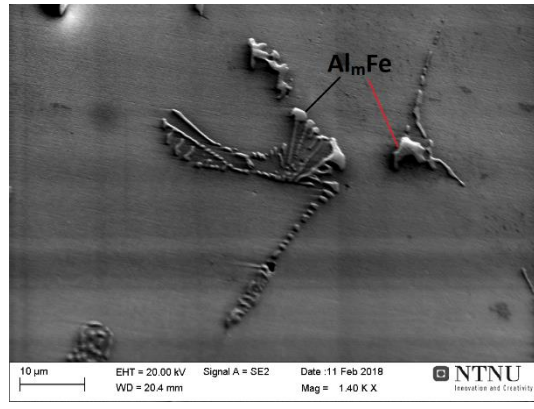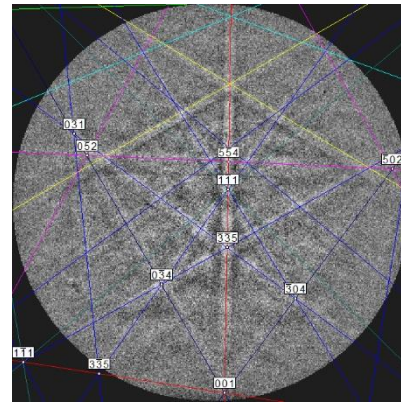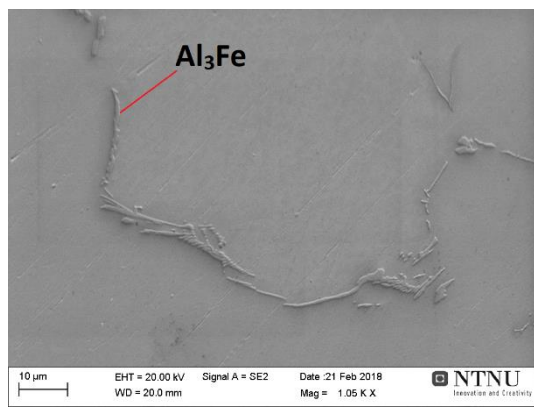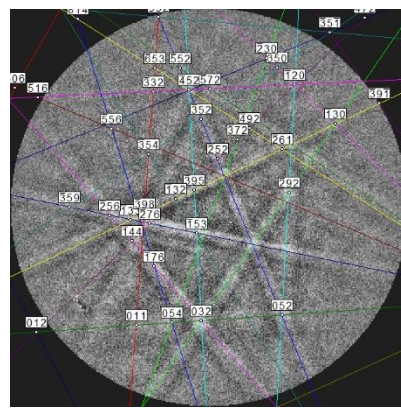
Figure 22: Mainly needle-like particles, but skeletal particles can occasionally be observed in sample T9.

Appendix 5: Different Particles Identified by EBSD Technique

Phase	Sample	Particle*	EBSP with overlaid solution
Al$_m$Fe	T3		
Al$_m$Fe	T3		
Al$_m$Fe	T3		
Al$_m$Fe	T3		

Al_mFe	T5	Al_mFe	
Al_3Fe	T7	Al_3Fe	
Al_3Fe	T7	Al_3Fe Al_3Fe	
Al_3Fe	T7	Al_3Fe	

* The lines show branches of the particle which were positively identified. The shown EBSP with overlaid solution is from the branch highlighted in red.

Appendix 6: Quantitative Analysis of XRD Measurements

Table 4: Results from quantitative phase analysis of XRD measurements (DTS= distance to surface).

Sample	Mean DTS [mm]	Al_mFe [wt%]	Al_3Fe [wt%]	Al_6Fe [wt%]	Rwp [%]
S1	7.5	90	10	0	8.4
S2	30.2	88	12	0	6.9
S3	51.5	84	16	0	7.7
S4	65.3	82	18	1	6.9
S5	78.8	63	31	6	6.5
S6	106.8	15	79	6	4.4
S7	134.7	10	89	1	5.8